Catalyst Design for Methane to Methanol Transformation via C-H Bond Activation using Transition Metal Oxide Dications

by

Emily Elizabeth Claveau

A Dissertation submitted to the Graduate Faculty of
Auburn University
in partial fulfillment of the
requirements for the Degree of
Doctor of Philosophy

Auburn, Alabama
August 5, 2023

Keywords: quantum chemistry, C-H bond activation, catalysis, methane to methanol transformation

Approved by

Dr. Evangelos Miliordos, Chair, *James E. Land* Associate Professor, Department of Chemistry and Biochemistry
J. Vincent Ortiz, *Ruth W. Molette* Professor, Department of Chemistry and Biochemistry
Konrad Patkowski, *S. D. and Karen H. Worley* Professor, Department of Chemistry and Biochemistry
Andrew Adamczyk, Assistant Professor, Chemical Engineering

Abstract

      The push towards greener energy solutions has been a focus for society in the last several decades, due to the need for cleaner industrial processes. One elusive process that draws the focus of several groups is methane to methanol transformation, which despite the continued search for a proper method providing both selectivity and efficiency, no ideal solution has been found. Here transition metal oxide dications are highlighted as potential catalytic candidates for methane to methanol transformation, through the use of high-level electronic structure calculations.

      Transition metal oxides are popular catalytic candidates due to their natural abundance and industrial applications. With the removal of two electrons for the formation of the dication the character of the metal oxide can be manipulated to favor CH bond selectivity or reaction efficiency. This dissertation illustrates the importance of these complexes and how to best apply them for the transformation of methane to methanol.

      Investigation began with a neutral transition metal oxide, niobium oxide, which indicated the importance of spin on the efficiency of the reaction mechanism, showing the higher spin states follow an efficient but non-selective pathway, and the lower spins following a selective yet less efficient and more energy intensive path. To understand the metal oxide character of the first-row transition metal oxide dications an extensive electronic structure analysis was performed on these complexes to characterize their behavior and was found that the early transition metals possessed oxo ground states and oxyl excited states, middle transition metals had oxyl ground states and oxo excited states, and the late transition metals having only oxyl states.

Using the spectrochemical series allows for the manipulation of oxo or oxyl character depending on the ligand introduced to the system. Due to the oxo metal oxides' preference for selectivity of the CH bond in methane, a strong field ligand was placed on the metal oxides to understand how the oxo state could be stabilized over the oxyl, even in the late transition metal case of cobalt oxide where a small oxo component at a small distance was stabilized over some oxyl components. Metal oxide dication systems with a fully saturated coordination sphere (five ammonia ligands) were explored to understand the effects of multiple ligands on the electronic structure and potential further stabilization of certain metal oxide character. Reacting a fully coordinated metal oxide dication with methane further emphasized the importance of excited states in these reactions in that they can influence ground state behavior and affect the outcome of the reaction. With this in mind the ground and excited states of the five-ammonia ligated metal oxide dications were analyzed at multiple different DFT functionals and multireference methods to determine a method to best systematically study these systems moving forward.

Acknowledgments

First, I would like to give my sincere gratitude to my advisor, Dr. Evangelos Miliordos. These five years would not have been possible without his unending support and guidance. Thank you for fostering such a welcoming environment in the group that allowed for creativity, productivity, and collaboration projects.

Thank you to my PhD committee, Dr. Vincent Ortiz, Dr. Konrad Patkowski, and Dr. Andrew Adamczyk for their guidance and continued discussion. Your advice has been invaluable and beneficial for the development of new ideas.

To my teammates and coaches at Auburn Masters Swimming. Thank you for the support and motivation both in and out of the pool, and pushing me to strive to be the best version of myself, as a swimmer, teammate, student, and researcher.

To Nuno Miguel da Silva Almeida, for all of his love, support, and encouragement. Without him this journey would not have been as enjoyable, I look forward to the next step together, and the many new adventures ahead.

To my parents and my brother, thank you for standing by me, for your constant love and support, and always believing in me when I did not believe in myself.

Table of Contents

List of Tables

List of Figures

Chapter 1: Introduction

It was estimated by the World Bank in 2015, that approximately 140 billion m^3 of natural gas was flared at thousands of oil fields across the globe.[1] This flaring of natural gas, which is about 70-90 weight percent methane, is not only a waste of potentially valuable resources but also a cause of significant environmental damage.[1,2,3] Methane is a major atmospheric pollutant with a 12-year life time in the atmosphere and is 25 times more potent as a greenhouse gas than CO_2, due in part to its ability to trap heat and absorb infrared radiation.[4] The Environmental Protection Agency (EPA) data from 2020 showed that CO_2 accounted for 79% of greenhouse gas emissions and CH_4 accounted for 11%, however with its high global warming index it causes a more adverse impact.[4] The leading cause of methane emission is natural gas and petroleum systems making up 32% of the emissions, 17% coming from landfills, and additional contributions from biomass and coal.[4] Fracking related methane leaks arise from the integrity of the well as gaps and microfractures between casing and cement can form during drilling, which occurs at high pressure or from improperly set cement.[5–7] Both of these contributing industries allow methane to "leak through the cracks" into the atmosphere without any containment. Ideally, the methane could be converted onsite to another, less harmful and potent chemical, but what would ideal conversion look like?

Methanol is a reasonable solution, as a liquid at room temperature, it is easier to transport without the need for high pressure storage. It is a bulk chemical widely used in the chemical industry with 21 million tons produced annually, and was originally distilled from wood earning its early moniker of "wood spirit" in 1601 by Robert Boyle until 1834 when it was first established as a chemical given the identity of methanol.[8] The first isolated synthetic methanol route was established in 1905 by Paul Sabatier, and later in 1934 the first synthetic methanol

plant was commercialized by BASF.[9] Methanol's diverse applications, as a solvent, gasoline additive, and chemical feedstock/platform chemical make it a desirable product.[10] It is also a promising alternative to auto and jet fuels and it is beneficial not only environmentally but also economically.[11] In 2005, George A. Olah presented the idea of a methanol economy "if we can produce methanol efficiently from non-fossil fuel sources, we could eventually replace oil and gas as a fuel and chemical raw material".[12]

A future world-wide methanol market would be beneficial as it would facilitate a push for independence from foreign energy sources and allow for conservation of existing petroleum-based energy reserves. Economically, consumers would see a lower cost resulting from the increased competition, in addition to the environmental benefit from improved or lessened emissions as methane would be captured and converted to methanol rather than vented or flared.[8] Present production efforts are expensive both financially and energetically, however a positive benefit cannot yet be fully exploited, and another low cost/low energy method is crucial.

The conversion of methane to methanol (MTM) is ideal, though some issues remain. The most pressing pertains to the C-H bond in question. The carbon hydrogen bond in methane is one of the strongest molecular bonds (439.3 ± 0.4 kJ mol^{-1}) and requires an adequate catalyst for activation.[13] However, methanol has a weaker carbon hydrogen bond than methane (401.92 ± 0.63 kJ mol^{-1}) and can over-oxidize to unwanted derivatives such as formaldehyde therefore it is important to choose a catalyst that is selective for the CH bond in methane but not for the bond in methanol to prevent over oxidation to unwanted products.[13]

Industrial methods for the transformation of methane to methanol exist, but come at a cost. Two common methods are the indirect and direct method of methane to methanol transformation, with the former the most well-known. The indirect method is the major current

industrial method and was first discovered for methane to methanol transformation involving the Fischer-Tropsch synthesis, which was patented in 1930.[14–16] This method is a two-step process, a steam reforming reaction to produce syngas ($CO + H_2$) via steam, O_2, or H_2, followed by the Fischer-Tropsch synthesis (FTS) utilizing harsh conditions for the hydrogenation of syngas to petrochemicals, most importantly methane.[16–19] Conditions required for the indirect transformation of methane to methanol are high temperatures ~700-1100°C and high pressures ~10-20 atm.[19,20] In addition to these harsh conditions the process is energy intensive, endothermic, and has low energy efficiency.[14] Industrial purification of methanol via the indirect method of transformation involves a third step. Following the endothermic step of syngas generation and methanol synthesis via FTS, the product purification step is necessary as low methanol yield and selectivity of FTS process result in the mixing of multiple impurities with the desired product.[21,22]

The direct method of methane to methanol transformation is more ideal, a one-step partial oxidation based on the avoidance of syngas generation, accounting for 60% of the cost, which would potentially reduce cost and increase efficiency.[23,24] Catalysts such as iron, cobalt, nickel, copper, and ruthenium have been introduced in conjunction with the direct method, however the purity of the produced methanol depends on the selectivity of the introduced catalyst.[25–28]

Direct Partial Oxidation of Methane
$$2CH_4 + O_2 \leftrightarrows CH_3OH + H_2O$$

Syngas
(CO, H_2O)

$$CO + H_2O \leftrightarrows CO_2 + H_2$$
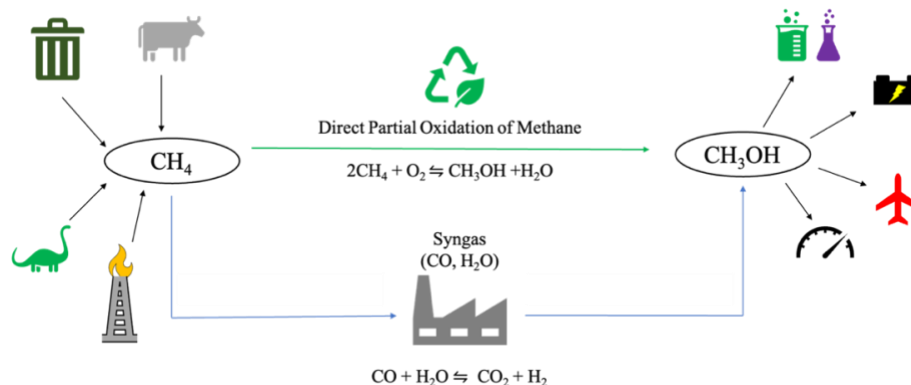
Figure 1.1: *Direct vs. Indirect methods of methane to methanol transformation*

Catalytic methods have been explored but struggle with the tradeoff between selectivity and efficiency. Homogeneous catalytic methods result in multiple side products and methanol derivatives, with low methane conversion rates due to the selectivity of a weaker methanol CH bond than that of CH_4 resulting in over-oxidation to methanol derivatives.[29] Nørskov *et. al.* explored the possibility of heterogenous catalysts but observed a similar problem with weak selectivity and over oxidation of methane to methanol.[30] If a catalytic route is chosen for the conversion of methane to methanol, it is imperative that the catalyst be both selective for the CH bond of methane and not over-oxidize methanol at the end step.

Several studies have been published regarding zeolite supported catalysts at moderate temperatures for the methane to methanol transformation, leading to breakthroughs in conversion, selectivity, or overoxidation prevention. A zeolite composed of either copper or iron was a successful breakthrough for methane to methanol conversion. In the case of copper the zeolite contains highly active oxygen species and can function at low temperatures.[31] Additionally, in 2017 an example of selective anaerobic oxidation with a direct stepwise method for MTM was shown to give a 97% selectivity over a copper zeolite with water as a source of oxygen.[32,33] Use of an iron zeolite (Fe ZSM5) showed methane oxidation in the presence of N_2O (1:1) leading to methanol formation directly on the surface.[33] Copper and iron zeolites are also shown to be effective with H_2O_2 oxidation, with 92% selectivity to methanol and only 0.5% conversion to overoxidized methanol derivatives.[34]

It is important to mention that a proper catalyst alone is not enough to improve the methanol yield. A plasma approach has been shown as an additional approach utilizing the direct method to achieve direct MTM conversion, while avoiding the challenge of low methanol selectivity and yield normally associated. The application of non-thermal plasma (NTP)

irradiation has been shown to be helpful in overcoming high chemical stability of reaction resulting from the CH bond of methane. The addition of a Dielectric Barrier Discharge (DBD) reactor has been considered for NTP reactor studies to optimize the methane to methanol process through either a temperature or substrate variation. Larkin *et. al.* focused on reacting methane to be recovered as a mixture of organic liquids (methanol included) over a range of temperatures and found that at higher temperatures there was less conversion of methane to liquid, than at lower temperatures.[35] However, there was no indication of the amount of methanol recovered in the mixture of liquid organics. Chawdhury *et. al.* found that packing the DBD with a substrate material improved the methanol selectivity by 10% and the yield by 3.7%, which packed with glass beads vs. a non-packed reactor.[36,37] It was later reported that the glass beads gave the best methanol selectivity of glass substrates investigated (spherical beads, hollow cylindrical capillaries, and spongy honeycomb wool) due to their structure allowing for uniform plasma discharge.[36,37]

Jiang *et. al.* presents an electrochemical approach to MTM in which electrochemical energy is harnessed for activation energy required to overcome both methane and oxidant barriers. Efficacy of both liquid and solid electrolytes were analyzed in the system. Deployment of solid electrolytes in electrochemical conversion of MTM offered the benefit of increasing system temperature to ~200 °C, which accounts for favorable CH activation. The drawback of the solid electrolytes however is their lack of active oxygen species with a suitable oxidation capability to attack the activated methane and convert to methanol while avoiding methanol over-oxidation, which in turn leads to low selectivity of methanol. Liquid electrolytes solve the problem of active oxygen species as there is a continuous supply, but the low methane solubility restricts the efficiency of methane to methanol conversion.[38]

As opposed to the higher temperature and pressure commercial conversion of methane to methanol, a biological route may provide insight into further understanding the conversion process. A class of bacteria known as methanotrophs possess a unique ability to use methane as both a carbon and an energy source to carry out the partial oxidation of methane to methanol at high selectivity and conversion.[39] The desired conversion is performed under ambient conditions with the assistance of the methane monooxygenase (MMO) enzyme, which assists the methanotrophic bacteria with the CH bond activation of methane making the MMO enzyme/ methanotroph relationship a potential model candidate for understanding the catalytic activity of methane to methanol transformation.[40–42]

A promising solution is the use of a metal oxide catalyst. They are considered one of the most important catalytic candidates for heterogeneous catalysis, and are good for most refining and petroleum processes, synthesis of specialized chemicals and improving environmental issues.[43,44] Prominence of metal oxide catalysts began in the 1950s when they were found to catalyze a variety of necessary reaction involved in petroleum chemistry such as oxidation and acid-base reactions.[44] Defects occurring in the metal oxides, such as kinks or steps allow for in structure selectivity and able to exploit different catalytic properties.[45] Transition metals are widely studied due to their diverse industrial applications, astrophysical applications, but mostly for their catalytic ability and high abundance.[46] They are well documented in their use as several works have been published on the use of transition metal oxides for methane to methanol conversion, across several charges for first and second row transition metals.[20,47–53]

The most promising candidate among the multitude of transition metal oxides is possibly the dication. Though these are shown to be both industrially and catalytically important, there is minimal electronic structure information in the literature.[54–64] Nature chooses dications for

multiple natural and biological processes for their ability to switch between the two forms of the

metal oxide, most notably the heme iron complexes in blood, as well as in enzymes. [65–70] Metal

oxide dications have two forms: oxo and oxyl. The oxo form of the metal oxide is characterized

by a closed shell on oxygen ($M^{4+}O^{2-}$), and the oxyl form has an unpaired electron on the

oxygen($M^{3+}O^{\bullet-}$).[71] Oxo and oxyl metal oxides react through different mechanisms, allowing their

behavior to be potentially exploited depending on the goal of the reaction. It is important to note

that metal oxide dications may not possess both the oxo and oxyl forms, therefore it is important

to study their electronic structure to completely understand their capabilities as potential

catalysts. Oxo metal oxides proceed via either the 2+2 or Proton Coupled Electron Transfer

(PCET) mechanisms, which are both selective mechanisms but possess high energy barriers. The

oxyl metal oxide form proceeds via the radical mechanism, also known as Hydrogen Atom

Transfer (HAT), unlike the previously mentioned mechanisms HAT is not selective for the CH

bond but possesses low energy barriers and is efficient compared to the 2+2 or PCET

mechanisms. Investigations of the electronic structure and reactivity potential of transition metal

oxide dications have been ongoing for both the first, and second row transition metals. Promising

data has been shown for their potential catalytic activity for both water and methane activation.
[47–50,52,53,55,72–76]

A solution for methane to methanol transformation may lie in the ability to design a

proper catalyst using either an oxo or oxyl metal oxide depending on the purpose it will serve

and add ligands from the spectrochemical series to further manipulate the character of the metal

oxide. The spectrochemical series provides a possible route to the manipulation of catalytic

behavior for reaction with methane. Strong field ligands such as ammonia, water, and CN$^-$ are

able to stabilize the oxo character in the metal oxides, where the weak field ligands, such as

halogens and OH^{-} stabilize the oxyl character. The importance of ligand effect on a catalyst was shown in two studies looking at iron oxide dication and the neutral zirconium oxide molecule. The iron oxide dication study completed by Kirkland *et. al.* shows the stabilization of the oxo excited state with water, and the further stabilization with the ammonia ligand; a stronger field ligand.[56] The state in question is an iron oxo excited state that is stabilized as the ground state with the addition of an ammonia ligand.

Additionally, the study completed on the neutral zirconium by Jackson *et. al.* shows the stabilization of the ligated metal oxides over the non-ligated complexes.[50] Focusing on the oxyl component of zirconium the authors showed the ability of weak field ligands to stabilize the methane to methanol transformation over the strong field ligated path and the non-ligated path.

The goal of this dissertation is to discuss the underlying mechanism of methane activation, characterizing the electronic structure of first row transition metal oxide dications, and apply ligands to these dications to understand the effects on the electronic structure and reactivity effects to create a functional catalyst for the successful transformation of methane to methanol.

A very detailed perspective on past and future strategies was published earlier in 2023 focusing on the catalytic advances made with cations, anions, and dications for tackling the selective methane to methanol conversion.[49] This dissertation focuses on molecular transition metal oxide dications (TMO^{2+}), ligand effects both on their electronic structure and reactivity, and an assessment of various methodologies.

1   A. G. Aregbe, Natural Gas Flaring—Alternative Solutions, *World Journal of Engineering and Technology*, 2017, **05**, 139–153.

2   R. Mansoor and M. Tahir, Recent Developments in Natural Gas Flaring Reduction and Reformation to Energy-Efficient Fuels: A Review, *Energy and Fuels*, 2021, **35**, 3675–3714.

3   Z. Zakaria and S. K. Kamarudin, *Renewable and Sustainable Energy Reviews*, 2016, 65, 250–261.

4   U.S. EPA, *Greenhouse Gas Emissions*, 2020.

5   J. N. Meegoda, F. Asce, ; Samuel Rudy, Z. Zou and M. Agbakpe, Can Fracking Be Environmentally Acceptable?, *J Hazard Toxic Radioact Waste*, , DOI:doi.org/10.1061/(ASCE)HZ.2153-5515.000033.

6   S. S. Harrison, Evaluating System for Ground-Water Contamination Hazards Due to Gas-Well Drilling on the Glaciated Appalachian Plateau, *Groundwater*, 1983, **21**, 689–700.

7   G. Bol, H. Grant, S. Keller, F. Marcassa and J. de Rozieres, Putting a stop to gas channeling, *Oilfield Rev.* , 1991, **3**, 35–43.

8   P. Khirsariya and R. K. Mewada, in *Procedia Engineering*, Elsevier Ltd, 2013, vol. 51, pp. 409–415.

9   T. J. Hall, J. S. J. Hargreaves, G. J. Hutchings, R. W. Joyner and S. H. Taylor, *Catalytic synthesis of methanol and formaldehyde by partial oxidation of methane*, ELSEVIER, 1995, vol. 42.

10   Q. Zhang, D. He and Q. Zhu, *Recent Progress in Direct Partial Oxidation of Methane to Methanol*, 2003, vol. 12.

11   M. Sohrabi and L. Vafajoo, Partial Oxidation of Methane to Methanol in a Catalytic Packed Bed Reactor: Kinetic Modeling and Experimental Study, *World Appl Sci J*, 2009, **6**, 339–346.

12   George A. Olah, The Methanol Economy, *Chemical & Engineering News Archive*, 2003, **81**, 5.

13   Y. R. Luo, *Comprehensive Handbook of Chemical Bond Energies*, CRC Press, Boca Raton, FL, 2007.

14   N. Salahudeen, A. A. Rasheed, A. Babalola and A. U. Moses, *J Nat Gas Sci Eng*, 2022, 108.

15   F. Wolke, Y. Hu, M. Schmidt, O. Korup, R. Horn, E. Reichelt, M. Jahn and A. Michaelis, Spatially-resolved reaction profiles in Fischer-Tropsch synthesis – influence of operating conditions and promotion for iron-based catalysts, *Catal Commun*, 2021, **158**, 106335.

16   Process for the Production of Paraffin-Hydrocarbons with more than one Carbon Atom (1,746,464), 1930, 1–3.

17   S. Abelló and D. Montané, Exploring Iron-based Multifunctional Catalysts for Fischer-Tropsch Synthesis: A Review, *ChemSusChem*, 2011, **4**, 1538–1556.

18   G. Henrici-Olivé and S. Olivé, The Fischer-Tropsch Synthesis: Molecular Weight Distribution of Primary Products and Reaction Mechanism, *Angewandte Chemie International Edition in English*, 1976, **15**, 136–141.

19   M. E. Dry and J. C. Hoogendoorn, Technology of the Fischer-Tropsch Process, *Catalysis Reviews*, 1981, **23**, 265–278.

20   H. Liu, J. Qu, M. Pan, B. Zhang, Q. Chen and C. He, Design and optimization of small-scale methanol production from sour natural gas by integrating reforming with hydrogenation, *Int J Hydrogen Energy*, 2020, **45**, 34483–34493.

21   T. Blumberg, T. Morosuk and G. Tsatsaronis, A comparative exergoeconomic evaluation of the synthesis routes for methanol production from natural gas, *Applied Sciences (Switzerland)*, , DOI:10.3390/app7121213.

22   C. Shi, M. Elgarni and N. Mahinpey, Process design and simulation study: CO2 utilization through mixed reforming of methane for methanol synthesis, *Chem Eng Sci*, , DOI:10.1016/j.ces.2020.116364.

23   A. de Klerk, Engineering evaluation of direct methane to methanol conversion, *Energy Sci Eng*, 2015, **3**, 60–70.

24   D. D. Anggoro, F. T. Chamdani and L. Buchori, One step catalytic oxidation process of methane to methanol at low reaction temperature : A Brief Review, *IOP Conf Ser Mater Sci Eng*, 2021, **1053**, 012056.

25   E. Iglesia, S. C. Reyes and R. J. Madon, *Transport-Enhanced a-Olefin Readsorption Pathways in Ru-Catalyzed Hydrocarbon Synthesis*, 1991, vol. 129.

26   L. A. Cano, A. A. Garcia Blanco, G. Lener, S. G. Marchetti and K. Sapag, Effect of the support and promoters in Fischer-Tropsch synthesis using supported Fe catalysts, *Catal Today*, 2017, **282**, 204–213.

27   H. M. Torres Galvis, J. H. Bitter, T. Davidian, M. Ruitenbeek, A. I. Dugulan and K. P. De Jong, Iron particle size effects for direct production of lower olefins from synthesis gas, *J Am Chem Soc*, 2012, **134**, 16207–16215.

28   M. Luo, H. Hamdeh and B. H. Davis, Fischer-Tropsch Synthesis. Catalyst activation of low alpha iron catalyst, *Catal Today*, 2009, **140**, 127–134.

29   M. Ravi, M. Ranocchiari and J. A. van Bokhoven, The Direct Catalytic Oxidation of Methane to Methanol - A Critical Assessment, *Angewandte Chemie*, 2017, **129**, 16684–16704.

30   A. A. Latimer, A. Kakekhani, A. R. Kulkarni and J. K. Nørskov, Direct Methane to Methanol: The Selectivity-Conversion Limit and Design Strategies, *ACS Catal*, 2018, **8**, 6894–6907.

31   M. H. Groothaert, P. J. Smeets, B. F. Sels, P. A. Jacobs and R. A. Schoonheydt, Selective oxidation of methane by the bis(μ-oxo)dicopper core stabilized on ZSM-5 and mordenite zeolites, *J Am Chem Soc*, 2005, **127**, 1394–1395.

32   V. L. Sushkevich, D. Palagin, M. Ranocchiari and J. A. Van Bokhoven, *Selective anaerobic oxidation of methane enables direct synthesis of methanol*, .

33   E. V. Starokon, M. V. Parfenov, S. S. Arzumanov, L. V. Pirutko, A. G. Stepanov and G. I. Panov, Oxidation of methane to methanol on the surface of FeZSM-5 zeolite, *J Catal*, 2013, **300**, 47–54.

34   J. Xu, R. D. Armstrong, G. Shaw, N. F. Dummer, S. J. Freakley, S. H. Taylor and G. J. Hutchings, Continuous selective oxidation of methane to methanol over Cu- and Fe-modified ZSM-5 catalysts in a flow reactor, *Catal Today*, 2016, **270**, 93–100.

35   D. W. Larkin, L. L. Lobban and R. G. Mallinson, Direct partial oxidation of methane to organic oxygenates using a dielectric barrier discharge reactor as a catalytic reactor analog, *Catal Today*, 2001, **71**, 199–210.

36   P. Chawdhury, D. Ray and C. Subrahmanyam, Single step conversion of methane to methanol assisted by nonthermal plasma, *Fuel Processing Technology*, 2018, **179**, 32–41.

37   P. Chawdhury, D. Ray, D. Nepak and C. Subrahmanyam, NTP-assisted partial oxidation of methane to methanol: Effect of plasma parameters on glass-packed DBD, *J Phys D Appl Phys*, , DOI:10.1088/1361-6463/aae635.

38   H. Jiang, L. Zhang, Z. Han, Y. Tang, Y. Sun, P. Wan, Y. Chen, M. D. Argyle and M. Fan, *Green Energy and Environment*, 2022, 7, 1132–1142.

39   R. S. Hanson and T. E. Hanson, *Methanotrophic Bacteria*, 1996, vol. 60.

40   D. Park and J. Lee, Biological conversion of methane to methanol, *Korean Journal of Chemical Engineering*, 2013, **30**, 977–987.

41   I. Y. Hwang, D. Hoon Hur, J. Hoon Lee, C. H. Park, I. S. Chang, J. W. Lee and E. Yeol Lee, Batch conversion of methane to methanol using methylosinus trichosporium OB3B as biocatalyst, *J Microbiol Biotechnol*, 2015, **25**, 375–380.

42   C. E. Bjorck, P. D. Dobson and J. Pandhal, Biotechnological conversion of methane to methanol: evaluation of progress and potential, *AIMS Bioeng*, 2018, **5**, 1–38.

43   J. C. Védrine, Metal Oxides in Heterogeneous Oxidation Catalysis: State of the Art and Challenges for a More Sustainable World, *ChemSusChem*, 2019, **12**, 577–588.

44   J. C. Védrine, Heterogeneous Catalysis on Metal Oxides, *Catalysts*, 2017, **7**, 341.

45   J. C. Volta and J. L. Portefaix, Structure Sensitivity of Mild Oxidation Reactions on Oxide Catalysts - A Review, *Appl Catal*, 1985, **18**, 1–32.

46   B. Su, Z. C. Cao and Z. J. Shi, Exploration of Earth-Abundant Transition Metals (Fe, Co, and Ni) as Catalysts in Unreactive Chemical Bond Activations, *Acc Chem Res*, 2015, **48**, 886–896.

47   S. N. Khan and E. Miliordos, Methane to Methanol Conversion Facilitated by Transition-Metal Methyl and Methoxy Units: The Cases of FeCH3+ and FeOCH3+, *Journal of Physical Chemistry A*, 2019, **123**, 5590–5599.

48   S. Sader and E. Miliordos, Methane to methanol conversion facilitated by anionic transition metal centers: The case of Fe, Ni, Pd, and Pt, *Journal of Physical Chemistry A*, 2021, **125**, 2364–2373.

49   E. E. Claveau, S. Sader, B. A. Jackson, S. N. Khan and E. Miliordos, Transition metal oxide complexes as molecular catalysts for selective methane to methanol transformation: Any prospects or time to retire?, *Physical Chemistry Chemical Physics*, 2023, **25**, 5313.

50   B. A. Jackson and E. Miliordos, Weak-field ligands enable inert early transition metal oxides to convert methane to methanol: The case of ZrO, *Physical Chemistry Chemical Physics*, 2020, **22**, 6606–6618.

51   R. A. Periana, D. J. Taube, S. Gamble, H. Taube, T. Satoh and Fujii Hiroshi, Platinum Catalysts for the High-Yield Oxidation of Methane to Methanol Derivative, *Science (1979)*, 1988, **280**, 560–564.

52   E. E. Claveau and E. Miliordos, Quantum chemical calculations on NbO and its reaction with methane: Ground and excited electronic states, *Physical Chemistry Chemical Physics*, 2019, **21**, 26324–26332.

53   N. M. S. Almeida, I. R. Ariyarathna and E. Miliordos, O-H and C-H Bond Activations of Water and Methane by RuO2+ and (NH3)RuO2+: Ground and Excited States, *Journal of Physical Chemistry A*, 2019, **123**, 9336–9344.

54   K. Qin, C. D. Incarvito, A. L. Rheingold and K. H. Theopold, Hydrogen atom abstraction by a chromium(IV) oxo complex derived from O2, *J Am Chem Soc*, 2002, **124**, 14008–14009.

55   I. R. Ariyarathna and E. Miliordos, Ab initio investigation of the ground and excited states of MoO+,2+,- and their catalytic strength on water activation, *Physical Chemistry Chemical Physics*, 2018, **20**, 12278–12287.

56   J. K. Kirkland, S. N. Khan, B. Casale, E. Miliordos and K. D. Vogiatzis, Ligand field effects on the ground and excited states of reactive FeO2+ species, *Physical Chemistry Chemical Physics*, 2018, **20**, 28786.

57   J. L. Tilson, W. C. Ermler and R. J. Fowler, CI potential energy curves for three states of RuO2+, *Chem Phys Lett*, 2011, **516**, 131–136.

58   D. Schröder, M. Engeser, H. Schwarz and J. N. Harvey, Energetics of the ligated vanadium dications VO2+, VOH2+, and [V,O,H2]2+, *ChemPhysChem*, 2002, **3**, 584–591.

59   D. Schröder, S. Bärsch and H. Schwarz, Second Ionization energies of gaseous iron oxides and hydroxides: The FeOmHn2+ dications (in = 1, 2; n ≤ 4), *Journal of Physical Chemistry A*, 2000, **104**, 5101–5110.

60   H. Johansen and K. Tanaka, Ab initio RHF, CI, and MC SCF calculations on the vanadyl ion, *Chem Phys Lett*, 1985, **116**, 155–159.

61   J. Fišer and R. Polák, The ZnO2+ dication in the gas phase, *Chem Phys Lett*, 2013, **558**, 8–14.

62   M. Reimann, F. A. Bischoff and J. Sauer, Thermochemistry of FeO mH nz Species: Assessment of Some DFT Functionals, *J Chem Theory Comput*, 2020, **16**, 2430–2435.

63   T. Z. H. Gani and H. J. Kulik, Understanding and Breaking Scaling Relations in Single-Site Catalysis: Methane to Methanol Conversion by FeIV=O, *ACS Catal*, 2018, **8**, 975-.

64   C. J. Ballhausen and H. B. Gray, The Electronic Structure of the Vanadyl Ion, *Inorg Chem*, 1962, **1**, 111–122.

65   R. J. Martinie, C. J. Pollock, M. L. Matthews, J. M. Bollinger, C. Krebs and A. Silakov, Vanadyl as a Stable Structural Mimic of Reactive Ferryl Intermediates in Mononuclear Nonheme-Iron Enzymes, *Inorg Chem*, 2017, **56**, 13382–13389.

66   J. Hohenberger, K. Ray and K. Meyer, The biology and chemistry of high-valent iron-oxo and iron-nitrido complexes, *Nat Commun*, 2012, **3**, 1–13.

67   T. L. Poulos, Heme enzyme structure and function, *Chem Rev*, 2014, **114**, 3919–3962.

68   A. H. Follmer, S. Tripathi and T. L. Poulos, Ligand and Redox Partner Binding Generates a New Conformational State in Cytochrome P450cam (CYP101A1), *J Am Chem Soc*, 2019, **141**, 2678–2683.

69   K. Ray, F. F. Pfaff, B. Wang and W. Nam, Status of reactive non-heme metal-oxygen intermediates in chemical and enzymatic reactions, *J Am Chem Soc*, 2014, **136**, 13942–13958.

70   A. J. Mitchell, N. P. Dunham, R. J. Martinie, J. A. Bergman, C. J. Pollock, K. Hu, B. D. Allen, W. C. Chang, A. Silakov, J. M. Bollinger, C. Krebs and A. K. Boal, Visualizing the reaction cycle in an Iron(II)- and 2-(Oxo)-glutarate-dependent hydroxylase, *J Am Chem Soc*, 2017, **139**, 13830–13836.

71   Y. Shimoyama and T. Kojima, Metal-Oxyl Species and Their Possible Roles in Chemical Oxidations, *Inorg Chem*, 2019, **58**, 9517–9542.

72   S. N. Khan and E. Miliordos, Electronic Structure of RhO2+, Its Ammoniated Complexes (NH3)1-5RhO2+, and Mechanistic Exploration of CH4Activation by Them, *Inorg Chem*, 2021, **60**, 16111–16119.

73   I. R. Ariyarathna and E. Miliordos, Radical abstraction: Vs. oxidative addition mechanisms for the activation of the S - H, O - nd C - H bonds using early transition metal oxides, *Physical Chemistry Chemical Physics*, 2021, **23**, 1437–1442.

74   I. R. Ariyarathna, N. M. S. Almeida and E. Miliordos, Ab initio investigation of the ground and excited states of RuO+,0,-and their reaction with water, *Physical Chemistry Chemical Physics*, 2020, **22**, 16072.

75   G. Liu, Z. Zhu, S. M. Ciborowski, I. R. Ariyarathna, E. Miliordos and K. H. Bowen, Selective Activation of the C−H Bond in Methane by Single Platinum Atomic Anions, *Angewandte Chemie*, 2019, **131**, 7855–7859.

76   K. J. De Almeida, T. C. Silva, J. L. Neto, M. V. J. Rocha, T. C. Ramalho, M. N. De Miranda and H. A. Duarte, Methane C-H bond activation by niobium oxides: Theoretical analyses of the bonding and reactivity properties of Nbo mn+ (m = 1, 2; N = 0, 1, 2), *J Organomet Chem*, 2016, **802**, 49–59.

Chapter 2: Methodology

This chapter presents the theory and methodologies used throughout the dissertation. Theory explanations were elaborated from Szabo and Ostlund and any additional information will be cited herein.[1]

The work in this dissertation is entirely computational. Computational chemistry is a definition encompassing many different types of calculations (electronic structure, molecular dynamics, molecular mechanics, etc.) as a subgroup of theoretical chemistry. As early as 1928 theoretical physicists were attempting to solve the Schrödinger equation, proposed by Erwin Schrödinger in 1926, with calculating machines to verify quantitatively experimentally reproduced solutions for simple systems such as the hydrogen molecule and the helium atom. With the invention of the electronic computer during World War II and general access to such technology to scientists in the following decade, a new field of theoretical chemistry was born as physicists were more focused on nuclear structure rather than molecular structure. This new field of Computational Chemistry worked towards the goal obtaining quantitative information regarding molecular behavior via numerical approximations of the Schrödinger equation solution with the use of a digital computer. Major developments in the following decades were packaged into software and readily available to chemists making quantum computational chemistry a more useful accessible tool, able to characterize molecular structure in minutes or hours instead of years. These developments have led to a greater output of literature regarding the applications of computational chemistry to chemical problems for the better understanding of structure and reactivity.[2]

1. Origins of Electronic Structure Theory

1.1. The Schrödinger Equation

An Austrian physicist by the name of Erwin Schrödinger proposed an equation in 1926 to solve for the total energy of a molecular system. This allows for the analytical solution of a one electron system to be easily obtained, whereas other systems require the implementation of numerical approximations. Shown in Equation 1 is the non-relativistic time independent Schrödinger equation, where $\hat{H}$ is the Hamiltonian operator, Ψ represents the wavefunction where information regarding the system resides, and E represents the absolute energy of the system.

$$\hat{H}\Psi = E\Psi \qquad (1)$$

As stated previously, $\hat{H}$ is the Hamiltonian operator that relates to the absolute energy of a molecular system of N electrons (i and j) and M nuclei (A and B) shown in a molecular coordinate diagram in Figure 2.1.
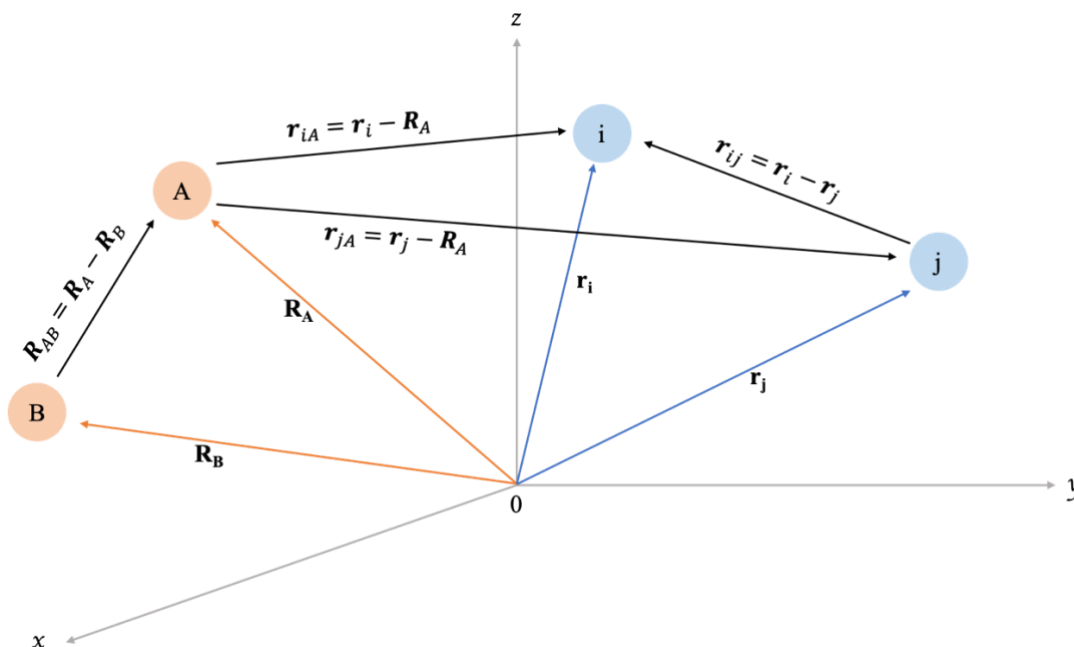
Figure 2.1: *Molecular coordinate diagram for two nuclei two electron system*

For a molecular system the Hamiltonian can be written as follows:

$$\hat{H} = \hat{T}_{el} + \hat{T}_{nuc} + \hat{V}_{el,nuc} + \hat{V}_{el,el} + \hat{V}_{nuc,nuc} \tag{2}$$

And further expanded as,

$$\hat{H} = -\sum_{i=1}^{N} \frac{\hbar^2}{2m_i} \nabla_i^2 - \sum_{A=1}^{M} \frac{\hbar^2}{2m_A} \nabla_A^2 \tag{3}$$

$$-\sum_{i=1}^{N}\sum_{A=1}^{M} \frac{Z_i e^2}{4\pi\varepsilon_0 |\vec{r}_j - \vec{R}_A|} + \sum_{i=1}^{N}\sum_{j>i}^{N} \frac{e^2}{4\pi\varepsilon_0 |\vec{r}_i - \vec{r}_j|} + \sum_{A=1}^{M}\sum_{B>A}^{M} \frac{Z_A Z_B e^2}{4\pi\varepsilon_0 |\vec{R}_A - \vec{R}_B|}$$

Where the first two terms correspond to the kinetic energy of the electrons and nuclei respectively, the third term representing the coulombic attraction between the electrons and nuclei, and the final two terms corresponding to the electron repulsion and nuclei repulsion respectively. The Hamiltonian written in Equation 3 can be further simplified into atomic units where mass of the electron (m_e), charge of the electron (e), $\frac{1}{4\pi\varepsilon_0}$, and $\hbar$ are set to 1, shown in Equation 4.

$$\hat{H} = -\sum_{i=1}^{N} \frac{1}{2} \nabla_i^2 - \sum_{A=1}^{M} \frac{1}{2M_A} \nabla_A^2 - \sum_{i=1}^{N}\sum_{A=1}^{M} \frac{Z_A}{r_{iA}} + \sum_{i=1}^{N}\sum_{j>i}^{N} \frac{1}{r_{ij}} + \sum_{A=1}^{M}\sum_{B>A}^{M} \frac{Z_A Z_B}{R_{AB}} \tag{4}$$

1.2. The Born Oppenheimer Approximation

The following discussion is a qualitative analysis of a central theme to quantum chemistry. The Born Oppenheimer Approximation is built on the fact that nuclei are much heavier than electrons (about 2000 times) thus they move more slowly, which allow for the terms referring to only nuclei, the kinetic energy of nuclei (term 2 in Equation 3 & 4) and the repulsion between nuclei (final term in Equation 3 & 4) can be considered separate. These constants now only add to the operator eigenvalues, no longer affecting the operator eigen functions.

The Hamiltonian operator ($\hat{H}$) is now referred to as the electronic Hamiltonian ($\hat{H}_{elec}$) which contains only the terms describing the motion of electrons and is summarized in Equation 5.

$$\hat{H} = -\sum_{i=1}^{N}\frac{1}{2}\nabla_i^2 - \sum_{i=1}^{N}\sum_{A=1}^{M}\frac{Z_A}{r_{iA}} + \sum_{i=1}^{N}\sum_{j>i}^{N}\frac{1}{r_{ij}} \tag{5}$$

This approximation reshapes the Schrödinger equation to only involve the electronic Hamiltonian shown in Equation 6 and the electronic wavefunction is transformed to describe the motion of electrons, expanded in Equation 7.

$$\hat{H}_{elec}\varphi_{elec} = E_{elec}\varphi_{elec} \tag{6}$$

$$\phi_{elec} = \phi_{elec}(\{r_i\}; \{R_A\}) \tag{7}$$

The above description of electron motion is explicitly dependent on the electronic coordinates, but parametrically dependent on nuclear coordinates, as a different arrangement of nuclei occurs the φ_{elec} becomes a different function of electronic coordinates. The same dependence is seen for the electronic energy

$$\varepsilon_{elec} = \varepsilon_{elec}(\{R_A\}) \tag{8}$$

With this approximation taken under consideration, the total energy expression is transformed to the sun of the ε_{elec} and ε_{nuc}.

$$\varepsilon_{tot} = \varepsilon_{elec} + \varepsilon_{nuc} = \varepsilon_{elec} + \sum_{A=1}^{M}\sum_{B>A}^{M}\frac{Z_A Z_B}{Z_{AB}} \tag{9}$$

A new nuclear Hamiltonian is generated for the motion of the nuclei, since electrons move much faster than nuclei, it becomes reasonable to replace the coordinates of electrons with their average values.

$$\hat{H}_{nuc} = -\sum_{A=1}^{M}\frac{1}{2M_A}\nabla_A^2 + \left(-\sum_{i=1}^{N}\frac{1}{2}\nabla_i^2 + \sum_{i=1}^{N}\sum_{A=1}^{M}\frac{Z_A}{r_{iA}} + \sum_{i=1}^{N}\sum_{j>i}^{N}\frac{1}{r_{ij}}\right) + \sum_{A=1}^{M}\sum_{B>A}^{M}\frac{Z_AZ_B}{R_{AB}} \qquad (10)$$

The above can be further simplified to

$$\hat{H}_{nuc} = -\sum_{A=1}^{M}\frac{1}{2M_A}\nabla_i^2 + \varepsilon_{elec}(\{R_A\}) + \sum_{A=1}^{M}\sum_{B>A}^{M}\frac{Z_AZ_B}{R_{AB}} \qquad (11)$$

$$\hat{H}_{nuc} = -\sum_{A=1}^{M}\frac{1}{2M_A}\nabla_i^2 + \varepsilon_{tot}(\{R_A\}) \qquad (12)$$

$E_{tot}(\{R_A\})$ provides a potential for nuclear motion as a function of the coordinates $\{R_A\}$ and can be mapped out as shown in Figure 2.1.

1.3. Antisymmetry Principle

To properly describe an electron, both the spatial and spin components need to be specified. At the non-relativistic limit, the electronic Hamiltonian only depends on the spatial component. Proper description of spin to done with the implementation of two spin functions $\alpha(\omega)$ for $m_s=+1/2$ and $\beta(\omega)$ for $m_s=-1/2$. It must be specified that the two spin functions abide by the following parameters

$$\int d\omega \alpha^*(\omega)\alpha(\omega) = \int d\omega \beta^*(\omega)\beta(\omega) = 1 \qquad (13)$$

And

$$\int d\omega \alpha^*(\omega)\beta(\omega) = \int d\omega \beta^*(\omega)\alpha(\omega) = 0 \qquad (14)$$

Since electrons are fermions, an additional requirement must be placed in the wavefunction: "a many-electron wavefunction must be antisymmetric with respect to the interchange of the coordinate **x** (both space and spin) of any two electrons."

$$\phi(x_1, \ldots, x_i, \ldots, x_j, \ldots, x_N) = -\phi(x_1, \ldots, x_j, \ldots, x_i, \ldots, x_N) \tag{15}$$

This requirement shown above in Equation 15 is known as the antisymmetry principle, and the antisymmetry is easily enforced during the construction of a wavefunction through the use of Slater determinants.

1.4. Spin and Spatial Orbitals: Role in constructing the Slater Determinant

An orbital is a wavefunction for a single particle, an electron. For the construction of a Slater determinant, both the spin orbital (discussed previously) and the spatial orbitals must be included.

Spatial orbitals $\psi_i(r)$ are a function of position vector r describing the spatial component of the probability of finding a particle at position r such that $|\psi_i(r)|^2 dr$ is the probability of finding an electron in small volume element *dr* and assumed to form an orthonormal set.

$$\int dr\ \psi_i^*(r)\psi_j(r) = \delta_{ij} \tag{16}$$

A complete description of an electron includes a complete set for describing spin consisting of two orthonormal functions $\alpha(\omega)$ and $\beta(\omega)$ for electron spin up and spin down respectively.

The wavefunction of an electron describes both the spatial distribution and its spin is known as a spin orbital, $\chi(x)$ where x is both spatial and spin coordinated. Each spatial orbital yields two spin orbitals, one for spin up (α) and one for spin down (β).

$$X(x) = \begin{cases} \psi(r)\alpha(\omega) \\ \psi(r)\beta(\omega) \end{cases} \tag{17}$$

The antisymmetry in the Pauli Exclusion Principle needs to be satisfied for the wavefunction, and easy enforcement via Slater determinants which satisfy the requirement and contain both spatial and spin components and allow for easy construction of the wavefunction as follows simplified for N electrons.

$$\psi(x_1, x_2, \dots, x_N) = \frac{1}{\sqrt{N!}} \begin{vmatrix} x_i(x_1) & x_j(x_1) & \dots & x_k(x_1) \\ x_i(x_2) & x_j(x_2) & \dots & x_k(x_2) \\ \vdots & \vdots & \ddots & \vdots \\ x_i(x_N) & x_j(x_N) & \dots & x_k(x_N) \end{vmatrix} \qquad (18)$$

2. Electronic Structure Methods

The goal of quantum chemists since the infancy of the field is to find and describe exact solutions to the electronic Schrödinger equation. However due to the presence of many electrons, the number of independent variables and complexity of the resulting equations render this task practically impossible ("many-electron problem"). One way to obtain approximate results is to exploit the variational principle, where the best wavefunction can be obtained through a minimization of the energy shown as:

$$\varepsilon = \langle \psi^* | H | \psi \rangle \geq \varepsilon_{exact} \qquad (19)$$

where the minimum value obtained from Equation 19 is the variational estimate of the exact ground state energy, and the best ψ will give lower energy closer to the exact energy, expressed as the simplified form for normalized wavefunctions.

The Hartree Fock approximation is central to the attempt to solve the electronic Schrödinger equation, constitutes the first step towards more accurate approximations, and has played an important role in modern chemistry.

2.1. Hartree Fock

The following discussion of the Hartree Fock approximation is merely a general picture, and not replacing the explanation in Szabo and Ostlund. The essence of the Hartree Fock approximation is to replace the complex "many-electron problem" with a "one-electron problem" where electron-electron repulsion is treated in an average way. Hartree Fock is an

approximate method because the wavefunction is written as a single Slater determinant (single

electron configuration). In this method, the energy is minimized by optimizing the coefficients

through the expansion of molecular orbitals via a linear combination of basis functions.

$$\phi_i = \sum_k c_{ki} g_k \tag{20}$$

This method is the starting point for several other methods used in this dissertation. Avoiding the

derivation which can be found in Szabo and Ostlund we result in the Hartree Fock equation.

The Hartree Fock equation is a pseudo one-electron equation treated with one electron

behavior with the others considered in an average way, it is similar to the Schrödinger equation

but uses orbitals (ϕ) instead of ψ and $\hat{F}$ instead of $\hat{H}$.

$$\hat{F}(\phi)\phi = E_\phi \phi \tag{21}$$

Note that $\hat{F}$ depends on the optimal orbitals ϕ. Due to the complexity of the Fock equation, basis

sets are introduced where the unknowns are coefficients (c_{ki}) and the Fock equation becomes

$$F(C)C = SCE \tag{22}$$

where F depends on C, and F depends on a solution whereas $\hat{H}$ in the Schrödinger equation does

not, therefore we must follow the iterative self-consistent field (SCF) process, illustrated below,

until ϕ or E converges.
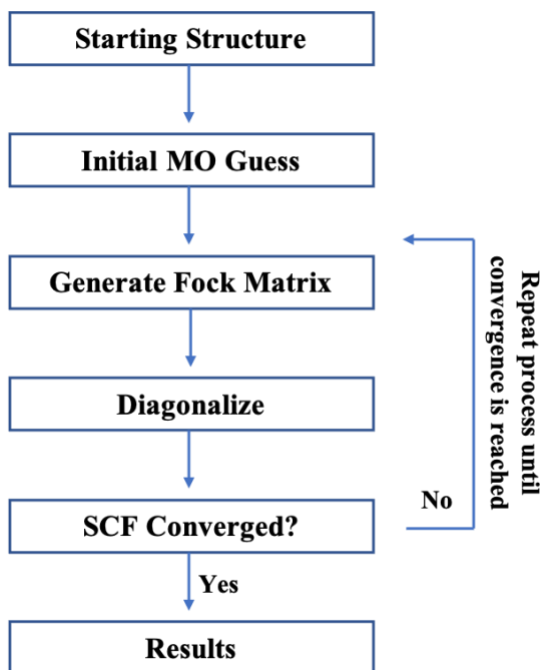
Figure 2.2: *Self-consistent Field Process*

3. Wavefunction Improvements

Improvements have been made to the wavefunction over the years resulting in the implementation of new methodologies. Some of these are discussed below and used throughout this dissertation.

3.1. MCSCF

The variational principle gives the central theme of Multi Configurational Self-Consistent Field method (MCSCF) is the use of more than one Slater determinants, varied in order to minimize the energy. The MCSCF wavefunction is built out with expansion coefficient c_I and the orthonormal orbitals $|\psi_I\rangle$, both of which are optimized.

$$|\psi_{MCSCF}\rangle = \sum_I c_I |\psi_I\rangle \tag{23}$$

MCSCF provides the freedom to decide which configurations are necessary to provide an adequate description.

Complete Active Space Self-Consistent Field (CASSCF) method is a widely used MCSCF variation. In CASSCF, the orbitals are separated into active and inactive orbitals, and further split into three groups: closed, occupied, and virtual. The inactive orbitals consist of doubly occupied orbitals otherwise denoted as closed or unoccupied orbitals and the remaining are considered active orbitals (i.e. those participating in promotions). As a result, the CASSCF wavefunction is written as a linear combination of the Slater determinants with all possible configurations present in the active space. In this method the energy is minimized variationally by optimizing both the coefficients and the molecular orbitals.

The resulting wavefunction is constructed from a linear combination of all possible arrangements within the active space from occupied to active orbitals, and referred to as the reference wavefunction. Active space refers to the orbitals participating in the excitation and is entirely molecule or system dependent, and will change for each system considered. However, the active space must be carefully chosen since not all orbitals can be included except for very small molecules, and large active spaces result in computationally expensive calculations. Figure 2.3 shows the movement within orbitals for the CASSCF method.
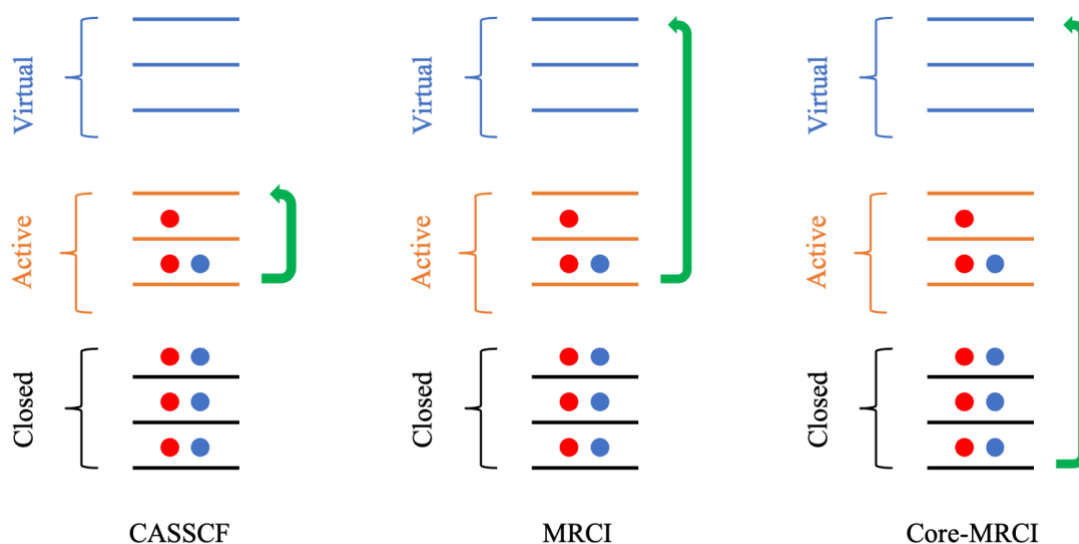
Figure 2.3: *Promotion of electrons across different wavefunction methods*

CASSCF method can be either state averaged or state specific. State averaged CASSCF (SA-CASSCF) refers to when more than one state is of interest, and the minimized energy is the averaged energy of the states in question (see Equation 24). SA-CASSCF is a common exploratory approach for proper active space characterization.

$$\varepsilon_{min} = \frac{\varepsilon_1 + \varepsilon_2 + \cdots + \varepsilon_n}{n} \tag{24}$$

Whereas state specific CASSCF asks one specific state at a time and the minimized energy reflects only that state.

3.2. Configuration Interaction

3.2.1. MRCI

Multi-reference Configuration Interaction (MRCI) is built on top of CASSCF and includes more Slater determinants, and promotions of electrons from the active orbitals to the virtual orbitals. The coefficients of these new Slater determinants are now optimized but not the orbitals, this optimization allows for further energy decrease and further approaching the ε_{exact}. This uses the reference wavefunction obtained at CASSCF and further minimizes the energy by allowing only single and double excitation (due to calculation limits) from the active to the virtual orbitals and further minimizes this energy. This energy drop is from the so-called "dynamic electron correlation", which includes the fine electron interaction and is important for defining energetics. Excitations are also allowed from the core to virtual orbitals, this process is known as core-MRCI and is a common practice when analyzing transition metals. Both MRCI methods and their corresponding excitations are shown in Figure 2.3 alongside CASSCF.

3.2.2. MRCI+Q

MRCI+Q is an approximate method built on top of MRCI that only gives a correction to the energy i.e. not wavefunction information. This correction is known as the Davidson

correction and is a semi-empirical way to obtain the contribution of higher excitations, in this case quadruple excitations. It is a good estimate for the energy as if quadruple excitations were included.

$$\Delta E_Q = (1 - a_o^2)(E_{CISD} - E_{HF}) \qquad (25)$$

Equation 25 shows the estimation of the energy for MRCI+Q where a_o is the coefficient of the wavefunction from CASSCF, and E_{CISD} is the energy obtained at the MRCI level.

3.2.3. Size extensivity

A method is considered size extensive if the energy of AB is equal to the energy at the infinite separation of A and B (see Equation 26).

$$E_{AB} = E_A + E_B \qquad (26)$$

Both CASSCF and Coupled Cluster methods (see below) are considered size extensive as they retain higher order excitations to satisfy Equation 26, thus the energy of the fragments A and B can be calculated separately.

Methods such as MRCI, MRCI+Q, and CASPT2 are size non-extensive, meaning the energy of AB does not equal the sum of the energies of A and B calculated separately, refer to Equation 27.

$$E_{AB} \neq E_A + E_B \qquad (27)$$

In order to calculate E_{AB} the, both fragments must be present but separated at an infinite distance.

4. Coupled Cluster Theory

Coupled Cluster calculations is a size extensive alternative to the previously discussed methods. In coupled cluster theory the wavefunction, known as the coupled cluster ansatz, is written as

$$\psi_{CC} = e^{\hat{T}}\psi_{HF} \tag{28}$$

where ψ_{HF} is a single Slater determinant. A limitation is placed of the systems that are able to be characterized by coupled cluster calculations, they must posses single reference character, i.e. one dominant electron configuration.

The general expression of the operator $\hat{T}$ is known (see Equation 29), however goal is to find the parameters that $\hat{T}$ is dependent on. $\hat{T}$ is known as the cluster operator and can be expanded as the sum of all possible excitations from occupied to virtual orbitals

$$\hat{T} = \hat{T}_1 + \hat{T}_2 + \hat{T}_3 + \cdots + \hat{T}_N \tag{29}$$

where N is the total number of electrons and $\hat{T}$ generates all possible determinant combinations of $\hat{T}$ acting on ψ. Single excitations are denoted as $\hat{T}_1$, double excitations as $\hat{T}_2$, triple excitations as $\hat{T}_3$, and so on and are written as follows.

$$\hat{T}_1\psi_{HF} = \sum_i^{occ} \sum_a^{virtual} t_i^a \psi_i^a \rightarrow t_i^a \tag{30}$$

Higher excitations involve more amplitudes, double excitations can be written succinctly as t_{ij}^{ab}, triples as t_{ijk}^{abc}, and higher excitations with the addition of appropriate indices for the occupied and virtual space. The coupled cluster method used throughout this dissertation is the Coupled Clusters Singles, Doubles, and Perturbatively Connected Triples, CCSD(T), and known as the "gold standard" of calculation.

5. Basis Sets

Basis sets have the ability to influence the result of the calculation and are necessary for the proper characterization of molecular systems.

5.1. Minimal Basis

A minimal basis contains the minimum number of basis functions to describe a given system. This results from the entire inner shell and valence orbitals from the corresponding atom or atoms in the molecule. The minimal basis for H_2 for example is composed of two functions, one corresponding to the 1s function of hydrogen A and the other corresponding to the 1s function of hydrogen B. Alternatively, CH_4 would include in its minimal basis the four 1s functions of the hydrogens, the 1s function of carbon, the 2s function of carbon, and the three 2p functions of carbon, resulting in a nine-function minimal basis.

The basis must be chosen carefully for each system, as the wrong choice can lead to results far from the real answer. Many types of basis sets have been proposed and used in various studies throughout the years but in this dissertation the correlation consistent family of basis sets is widely used and will be discussed below, along with additional basis set implementations.

5.2. Correlation Consistent Basis Sets

Correlation consistent basis sets were developed by Dunning et al in 1989 for the first-row atoms boron-neon, by adding shells of functions to core set of atomic Hartree Fock functions, and are accurate in dealing with outer electron behavior.[3] This was based on the work of Almlöf and coworkers who found that basis sets from correlated atomic calculations provide and excellent description of molecular correlation effects.[4,5]

This class of basis sets take on the form cc-pVXZ. The "cc" indicates correlation consistent, "p" indicates polarization functions which add higher angular momentum functions in the basis set and are important to describe the perturbation of the atomic wavefunctions within the molecule and account for diffuse character the orbitals cannot describe. Most interesting for this class pertains to "X" which can be "D, T, Q, 5, …", as the value of X is increased the

number of functions on the atom also increases. Referring to Figure 2.4 representing oxygen, as the value of X increases additional s, p, d, f, g, h-type functions are placed on the atom, this model holds for the first and second row atoms as proposed by Dunning and coworkers.[3]
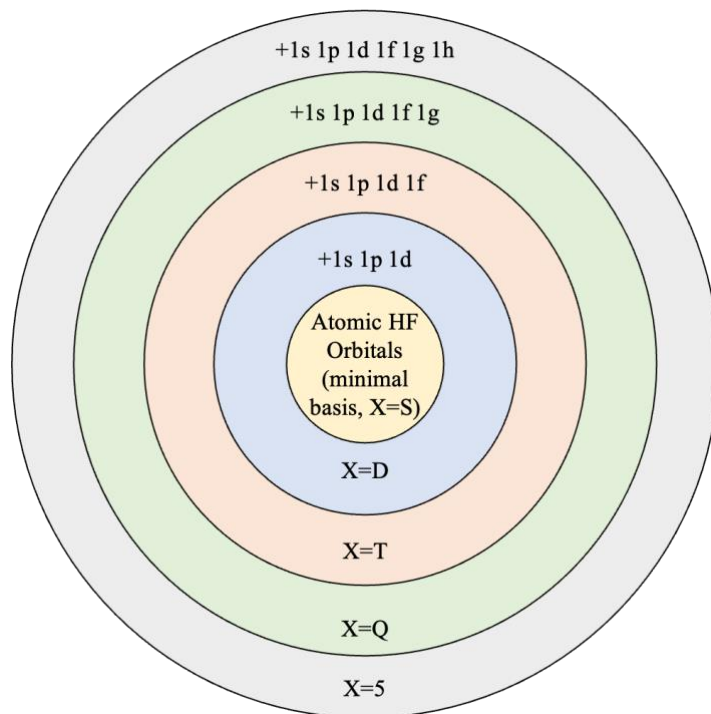
Figure 2.4: Expansion of correlation consistent basis set

Additional forms of the basis function are written to include a pseudopotential (cc-pVXZ-PP) or diffuse functions (aug-cc-pVXZ) and are discussed in the next two sections.

5.3. Effective Core Potentials (Pseudopotentials)

One way to consider relativistic effects is using an effective core potential (ECP). In this case, the inner electrons are not included in the calculation since relativistic Hamiltonian is necessary to accurately describe their orbitals due to their high speeds. Rather they are replaced with a pseudopotential and gives accurate results despite only considering the valence electrons of the system.[6] Pseudopotentials are more commonly included in calculations involving the lower half of the periodic table beginning with the second-row transition metals, due to the large

atomic number (or nuclear charge) in heavy atoms and the non-negligible relativistic effects. This manages to reduce the computational cost as they do not play a significant direct role in chemical behavior. Debate exists over whether to use "small core" or "large core" pseudopotentials, both of which close off all shells except those most affected by chemical bonding, with the small core treating the outermost two shells as explicit electrons. Though it is more expensive it is also more accurate, and the large core only the outermost one shell. These effects neglect to include the inner core electrons, due to the high speeds (close to the nucleus), in the Hamiltonian and only solve the Schrödinger equation for the valence electrons.

5.4. Diffuse Functions

Diffuse functions represent the tail portion of the atom's orbital, distant from the nuclei. These functions are shown to be good for both anions and Rydberg states. In this dissertation they are most commonly placed on the oxygen atom of a metal oxide to account for the anionic character of the oxygen terminus (polarized bond), and are referred to as augmented basis sets (aug-cc-pVXZ).

6. Density Functional Theory

Calculations on large or complex systems are highly demanding and require large amounts of resources that are often unavailable. Density Functional Theory offers an alternate method that reduces this cost and considerably increases the size of the systems that can be studied.

Density Functional Theory is the method where the energy (E) is written as a function of the electronic density (ρ) and minimized with respect to ρ. The main benefit is while a wavefunction if expressed in terms of the positions or coordinates of all electrons, ρ is a three variable function expressed as a function of a given x, y, z coordinate.

E and ρ are connected with an exact functional, comprised of five components, under the basic idea that if the density is known then the energy is also known. A functional consists of five terms:

- Electron-electron repulsion

- Exchange (XC) correlation

- Nuclear electron attraction

- Nuclear-nuclear repulsion

- Kinetic energy of electron

Three of these terms are known, the attraction and both repulsion terms, as they are coulombic, and are a function of electronic density, thus easy to calculate if the electronic density is known.

The kinetic energy (KE) and exchange (XC) terms are more difficult. For the kinetic energy term Kohn-Sham formulation is required where the density is obtained as the squared moduli of occupied Kohn-Sham orbitals and then kinetic energy is obtained in terms of occupied molecular orbitals. The XC term is implemented by different empirical functionals.

7. Functionals

Several functionals have been developed over the years to improve the exchange correlation (XC) term. Simply put, a functional is the function of a function. Each type of functional writes the XC term in a different empirical form, sometimes with different parameterizations. A model XC term is present in Hartree Fock calculations and is written as:

$$\hat{K}_j(x_1)f_i(x_1) = \phi_j(x_1) \int \frac{\phi_j^*(x_2)f_i(x_2)}{r_{12}} dx_2 \qquad (31)$$

7.1. Local Density Functionals (LDA)

The Local Density Approximation is the simplest proposed model. Here the E_{XC} term is defined only by the density (ρ).

$$E_{XC} = \int_{-\infty}^{+\infty} \varepsilon_{XC}(\rho(r))dr \qquad (32)$$

This approach assumes a homogeneous electron gas (Jellium model) which is inaccurate for

molecular systems.[7]

7.2. Generalized Gradient Approximation (GGA)

GGA type functionals are a betterment of the LDA functionals in that now a spatial non-

uniform variation component of $\rho(r)$ is included, meaning functionals of this type are dependent

on both the density and its gradient.

$$E_{XC} = \int_{-\infty}^{+\infty} \varepsilon_{XC}(\rho(r), \nabla\rho(r))dr \qquad (33)$$

This allows for improvement of the results over the LDA type functionals especially regarding

energy barriers and characterize well ionic, covalent, metallic, and hydrogen bonding.[8] However,

these functionals struggle for van der Waals interactions but characterize well ionic, covalent,

metallic, and hydrogen bonding. A functional of this type used in this dissertation is the BLYP

functional.

7.3. Meta-GGA

Inclusion of additional semi-local information led to the implementation of Meta-GGA

type functionals. Functionals of this group have explicit dependence on higher order (mainly

second order) gradients of ρ on the kinetic energy density which involves the gradients of the

occupied orbitals.[9]

$$E_{XC} = \int_{-\infty}^{+\infty} \varepsilon_{XC}(\rho(r)), \nabla(\rho(r)), \nabla^2(\rho(r))dr \qquad (34)$$

These functionals have a significant improvement in the determination of atomization energies compared to their predecessors.[9,10] The M06-L functional mentioned in several parts of this dissertation is a member of the Meta-GGA functional family.

7.4. GGA hybrid

Development of hybrid functionals has allowed for improvement by matching the XC of the GGA method and mixing a percentage of Hartree Fock exchange (see above). This improvement allows for a significant advance in calculating molecular properties, the most notable functional from this group is B3LYP which is used in this dissertation alongside its counterpart M06.

7.5. Meta-GGA hybrid

This additional hybrid group involves the dependence on Hartree Fock exchange, the gradient of ρ and the kinetic energy density. Functionals of this type are constructed using empirical fittings of their parameters and have shown improvement in the determination of energy barriers and atomization energies.[9] TPSSH and MN15 are both functionals of this type used in this dissertation, MN15 specifically for transition metals as it has been proposed to properly characterize transition metal character.[11,12]

8. Spin Orbit

Spin orbit addresses the coupling between spin and orbital angular momenta. The motion of a charged particle generates a magnetic moment (i.e. acts as a magnet.) Both the motion of the electron around the nuclei (orbital angular momentum) and the electronic spin are sources of magnetic moments. The interaction of the two "magnets" is not generally included in the Hamiltonian unless a spin orbit term is added. This is especially important for second-row

transition metals and beyond as the spin orbit coupling constant, the energy distance between splittings, is typically very small up to and including the first-row transition metals.

9. Dipole Moments

A dipole moment, or first multipole electric moment, indicates how polarized a system is, and shows how easily or how strongly a system is affected by the application of an external field. Herein two ways of determining the dipole moment (μ) are discussed.

9.1. Expectation Value

Expectation values can be gathered from the calculations and used for dipole moment calculations for wavefunction methods.

$$\vec{\mu} = e \int \psi^* \vec{r} \psi d\tau + \sum_i z_i \vec{R}_i \tag{35}$$

However, for methods such as MRCI+Q that do not have a wavefunction since it is only an energy correction, the expectation value cannot be determined. This method for dipole moments is often inaccurate as it carries errors.

9.2. Finite Field Approach

A more accurate method for calculating the dipole moment is the finite field approach which involves the application of an external field (Δf) to see how the energy changes (ΔE) to calculate the dipole moment (μ) as shown succinctly in Equation 36.

$$\mu = \frac{\Delta E}{\Delta f} \tag{36}$$

The larger the dipole moment the more sensitive it is to an external field and the more active indicated by the large energy change. This method is much more accurate than the expectation value method since the finite field Approach is an energy based and the energy is less sensitive than the wavefunction (e.g. Hartree Fock iteration), and is the ratio of two differences resulting in the cancellation of two

errors, the cancellation of energy and the cancellation of polarizability if a proper numerical method is used.

1   A. Szabo and N. S. Ostlund, *Modern Quantum Chemistry: Introduction to Advanced Electronic Structure Theory*, Dover Publications, New York, 1996.

2   National Research Council, in *Mathematical Challenges from Theoretical/Computational Chemistry*, National Academies Press, Washington, D.C., 1995.

3   T. H. Dunning, Gaussian basis sets for use in correlated molecular calculations. I. The atoms boron through neon and hydrogen, *J Chem Phys*, 1989, **90**, 1007–1023.

4   J. Almlöf, T. Helgaker and P. R. Taylor, Gaussian Basis Sets for High-Quality ab Initio Calculations, *J. Phys. Chem*, 1988, **92**, 3029–3033.

5   J. Almlöf and P. R. Taylor, General contraction of Gaussian basis sets. I. Atomic natural orbitals for first- and second-row atoms, *J Chem Phys*, 1987, **86**, 4070–4077.

6   L. R. Kahn and W. A. Goddard, Ab initio effective potentials for use in molecular calculations, *J Chem Phys*, 1972, **56**, 2702–2712.

7   V. Sahni, K.-P. Bohnen and M. K. Harbola, Analysis of the local-density approximation of density-functional theory, *Phys Rev A (Coll Park)*, 1988, **37**, 1895–1907.

8   J. P. Perdew, K. Burke and M. Ernzerhof, Generalized Gradient Approximation Made Simple, *Phys Rev Lett*, 1996, **77**, 3865–3868.

9   J. Tao, J. P. Perdew, V. N. Staroverov and G. E. Scuseria, Climbing the density functional ladder: Nonempirical meta–generalized gradient approximation designed for molecules and solids, *Phys Rev Lett*, 2003, **91**, 146401.

10   J. Tao, J. P. Perdew, A. Ruzsinszky, G. E. Scuseria, G. I. Csonka and V. N. Staroverov, Meta-generalized gradient approximation: Non-empirical construction and performance of a density functional, *Philosophical Magazine*, 2007, **87**, 1071–1084.

11   S. N. Khan and E. Miliordos, Methane to Methanol Conversion Facilitated by Transition-Metal Methyl and Methoxy Units: The Cases of FeCH3+ and FeOCH3+, *Journal of Physical Chemistry A*, 2019, **123**, 5590–5599.

12   H. S. Yu, X. He, S. L. Li and D. G. Truhlar, MN15: A Kohn-Sham global-hybrid exchange-correlation density functional with broad accuracy for multi-reference and single-reference systems and noncovalent interactions, *Chem Sci*, 2016, **7**, 5032–5051.

This chapter is a summary of a published manuscript found in Appendix A

Chapter 3: Mechanism of Methane Activation

Transition metals have been widely studied due to their industrial and catalytic applications and transition metal oxides have given promising results.

Catalysis is a growing field with several industrial applications ranging from refineries and pharmaceuticals to environmental problems involving but not limited to biomass, biofuels, and fossil fuels.[1] One of these problems in the transformation of methane to methanol which requires a suitable catalyst to activate the CH bond of methane. This bond however is one of the strongest molecular bonds requiring more of the catalyst to not only activate but return the catalyst and not over oxidize the desired products. Many catalytic candidates have been proposed such as the $FeSO_4$ catalyst which is one of the first patents for a methane oxidation catalyst, electrolytic copper which gave a higher methanol yield with lower oxygen concentration, supported oxides of various metals (Pd, Co, Cu, Mn, Ce, V, Fe, Ti), and the Periana catalyst.[2–5] But the most promising candidates may be the transition metal oxides. Transition metal oxides have a unique nature due to the outer d electrons, and the metal oxygen bonding varies between nearly ionic to highly covalent or metallic, and the presence of electrons or lone pairs on oxygen can further alter the behavior of metal oxides, making them easier to manipulate catalytically.[6]

Transition metal oxides have been previously studied in the literature but most of the electronic structure work exists on the first-row metals for both neutral and charged species, though many second-row works exist as well.[7–22] Here we focus on the second-row transition metals and compare to their first-row analogs. Investigating the catalytic activity of a metal oxide begins with and analysis of its electronic structure this section covers the mechanism of methane activation via niobium oxide. Niobium oxides have been implemented in gas sensors, electrochromics,

electrolytic capacitors, and rechargeable batteries due to their energy band structure and multiple crystal structures.[23-25] Catalytically Nb_2O_5 has been promising as a degradation candidate for toxic organic dyes such as methylene blue.[26] High catalytic activity of niobium stems from its high acidity, redox properties, and strong interaction between metal and support materials, these properties allow niobium to take on multiple catalytic roles: active phase, dopant, or support.[27]

This discussion begins with an investigation into the electronic structure of a transition metal oxide, NbO, to understand its behavior and character followed by its reaction with methane and how it behaves mechanistically and a final discussion on the effect of spin on the mechanistic behavior of methane to methanol transformation.

1. Computational Techniques

To solve the electronic Schrödinger equation multireference configuration interaction (MRCI) was employed. The reference wavefunction was obtained at the complete active space self-consistent field (CASSCF) level with all valence electrons correlated. Chosen active space consists of nine electrons in twelve orbitals: the three 2p orbitals or oxygen, one 5s, five 4d, and three 5p orbitals of niobium. The 5p orbitals of niobium are only partially occupied at every metal oxygen distance but deemed necessary for smooth convergence of CASSCF iterations. MRCI and MRCI+Q calculations were carried out with the 2s electrons of oxygen not previously included in the active space at CASSCF, the Davidson correction (+Q) is implemented to account for the portion of missing dynamic correlation and to alleviate the size extensivity error of MRCI. Coupled cluster singles, doubles, and perturbatively connected triples (CCSD(T)) calculations were carried out for states with dominant single reference character. Additional CCSD(T) calculations involving the sub-valence $4s^24p^6$ niobium electrons were carried out, referred to as C-CCSD(T). Spin orbit calculations were performed by adding the Breit-Pauli spin-orbit operator to

the electronic Hamiltonian and diagonalizing the new Hamiltonian matrix from the unperturbed MRCI wavefunctions at 1.7Å.

Correlation consistent basis sets were implemented for this work. The cc-pV5Z-PP basis placed on niobium, which includes the Stuttgart relativistic effective core pseudopotential which replaced the 28 electrons of niobium ($1s^2 2s^2 2p^6 3s^2 3p^6 3d^{10}$), and the aug-cc-pV5Z basis on oxygen with diffuse functions to better describe the polarized $Nb^{\delta+}O^{\delta-}$ bond.[28–31] The corresponding weighted-core cc-pwCV5Z basis set was applied when excitations from the inner $4s^2 4p^6$ electrons of niobium were allowed.[31] The C_{2v}, highest Abelian subgroup of the full $C_{\infty v}$ point group was selected. Numerically solving the ro-vibrational Schrödinger equation allowed for the evaluation of spectroscopic constants. Dipole moments were calculated as both expectation values and using the finite field approach where dipole moments are calculated as a linear response to an applied electric field (μ_{FF}) with ±0.001 a.u. intensity applied along the interatomic axis. All calculations related to the electronic structure portion of this study were carried out in MOLPRO 2015.[32]

CASSCF, CCSD(T), and DFT calculations were carried out on the reaction of NbO with methane. DFT calculations were done in Gaussian 16 with the MN15 functional due to its ability to properly characterize the behavior of transition metals.[18,33,34] To study the first step of the reaction (NbO + CH_4 → CH_3NbOH) CASSCF calculations were employed involving an active space consisting of 11 electrons in 11 orbitals. The 11 orbital active space is made up of the nine molecular orbitals of NbO used for the electronic structure analysis, and the bonding and anti-bonding molecular orbitals of the activated C-H bond. Three orbitals of NbO corresponding to the 5p orbitals of niobium remain inactive as their contribution at equilibrium distances is minor.

Single point CCSD(T) calculations were employed for the two-step reaction (NbO + CH_4→Nb + CH_3OH) using DFT optimized geometries (CCSD(T)//MN15) due to substantial

single reference character in almost all cases. The same 11 electron/11 orbital active space was used and CASSCF calculations were done to obtain the largest coefficient of the CI vector, then the T1 diagnostic was gathered at the CCSD level to assess the multi-reference character of the intermediates and transition states. Correlation consistent basis sets were also applied for the reaction part of the study but this time using the cc-pVTZ-PP basis on niobium, cc-pVTZ on carbon and hydrogen, and the aug-cc-pVTZ on oxygen.[29–31,35]

2. NbO Electronic Structure Overview

Beginning with the fragments the Nb ground state is a ^6D with a $5s^1 4d^4$ configuration, and is one of three transition metals which prefer the $s^1 d^5$ half-filled valence shell.[36] Niobium's first excited state is of the more common s^2 character ($5s^2 4d^3$) lying 1486 cm^{-1} (M_J averaged above the ground state.) Combining the Nb (^6D) + O (^3P) fragments results in the following states $^{4,6,8}[\Sigma^+(1)$, $\Sigma^-(2)$, Π (3), Δ (2), Φ (1)] , and the combination of the Nb (^4F) + O (^3P) results in the following states $^{2,4,6}[\Sigma^+(2)$, Σ^- (1), $\Pi(3)$, $\Delta(3)$, $\Phi(2)$, $\Gamma(1)]$.

Potential energy curves for the doublet and quartet are shown in Figure 3.1, sextet states were found to be too high in energy and are not considered in the electronic structure discussion.
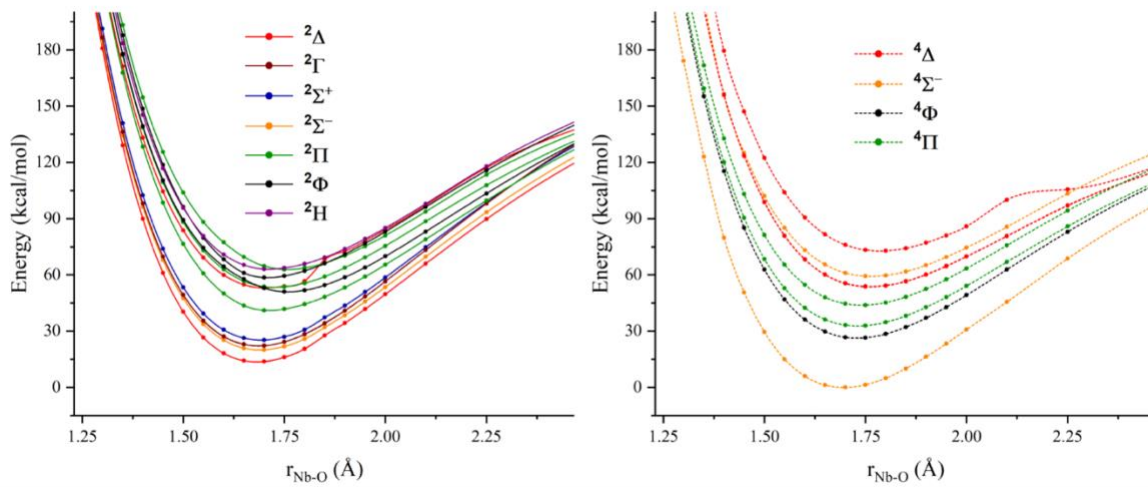
Figure 3.1*: Potential Energy Curves for S=1 and S=3 of Niobium Oxide*

The ground state of this system is a $^4\Sigma^-$, single reference state with a $3\sigma^\alpha\ 1\delta_{xy}^\alpha\ 1\delta_{x^2-y^2}^{2\alpha}$ configuration. It is also well bound and well separated from the excited states and the equilibrium wavefunction points towards metal oxo (O^{2-}) picture. The $^2\Delta$ first excited state lies about 30 kcal/mol above the ground state as a result of the promotion of a $1\delta_{x^2-y^2}^2$ orbital to 3σ and is also a single reference entity. The configurations of the lowest seven states of niobium are shown in Figure 3.2, and become increasingly more multireference the first six of which see single occupation in the 3σ and the seventh ($1^2\Pi$) returning to double occupation in 3σ orbital.

These states are not typically oxyl as there is no unbound character on the oxygen terminus and have smaller metal oxygen bond lengths typical of this species. Spectroscopic information was gathered for the several doublet and quartet states at various methods to compare to experiment.

Figure 3.2: Electron Configuration for lowest seven states of NbO

The ground state possesses a 1.696 Å Nb-O distance that changes by only 0.002 Å with the Davidson correction and CCSD(T), and an additional 0.015Å elongation with the addition of core correlation.

3. Reaction of NbO with CH4

We analyze the reaction of NbO with methane for the activation of the CH bond of methane for the formation of CH_3NbOH. The reaction of $NbO^{+,0,2+}$ and $NbO_2^{+,0,2+}$ have been studied in the

literature but only for the ground state.[37–39] Here we use not only the ground state but also the low-lying excited states of NbO to explore the activation of the CH bond of methane.

Intermediate structures were obtained at the DFT/MN15 level due to MN15's ability to properly characterize transition metals. Potential Energy Profiles were created for the S=1/2 and S=3/2 states to account for the behavior of excited states in the reaction. Figure 3.3 shows the intrinsic reaction coordinate for the reaction of NbO with CH_4 focusing on the CH bond activation step. This includes the pathways for the ground state and lowest excited states up to the CH_3NbOH intermediate step.
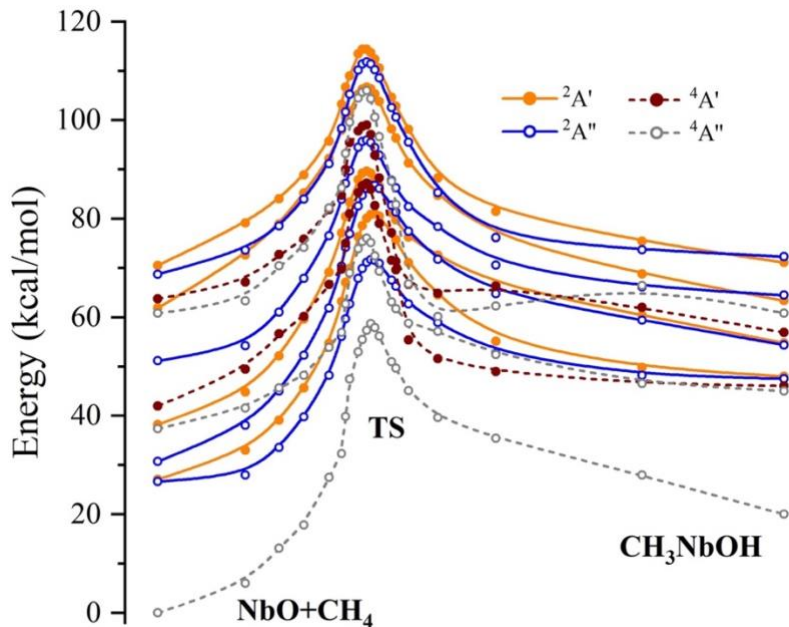
Figure 3.3: *Potential Energy Profile along Intrinsic Reaction Coordinate of NbO + CH₄*

Here the $^4A''$ pathway corresponds to the $^4\Sigma^-$ ground state of the diatomic. The $^2\Delta$ first excited state from the diatomic splits into two components, $^2A'$ and $^2A''$, for the reaction with methane. From this initial analysis we see the ground state quartet pathway remains well separated as it did in the metal oxide analysis discussed previously. These components are characterized by $3\sigma^2 1\delta_{xy}$ and $3\sigma^2 1\delta_{x^2-y^2}$ configuration for the $^2A'$ and $^2A''$ respectively. Both the $^2A'$ and

^{2}A′′components start from the same energy and configuration at the NbO+CH$_4$ step and converge to the same energy at the end of the reaction at the CH$_3$NbOH step with both bearing $3\sigma^21\delta^1$ character. The next excited state in the diatomic is a $^2\Sigma^-$, which in this figure is represented by a ^{2}A′′ path as the Σ denotes only one component. This ^{2}A′′ from the $^2\Sigma^-$ retains the $3\sigma^11\delta^2$ character across the reaction, and the same occurs for the remaining S=1/2 states above this state. However, the S=3/2 states undergo some avoided crossings, for example, the ^{4}A′′ and ^{4}A′ components of the $^4\Phi$ and $^4\Pi$ cross in the transition state region and exchange their $3\sigma^11\delta^22\pi^1$ configurations. From the potential energy profiles gathered here is can be conclusively noted that the reaction of the lowest energy states of NbO +CH$_4$ proceed via a 2+2 mechanism in which one of methane's C-H bonds is heterolytically cleaved, a proton attaches to the oxygen from the cleaved bond, and the remaining methyl anion bonds to niobium (shown in Figure 3.3). An alternative mechanism, the radical mechanism, is not currently observed due to the strong Nb^{2+}O^{2-} oxo character of the Nb–O bond ($2\sigma^21\pi^4$). However, due to this lack of additional mechanism in the potential energy profile when the reaction pathway was constructed the S=5/2 pathway was included, as our electronic structure calculations indicated the high spin states correspond to the Nb^{3+}O$^{\bullet\,-}$ which facilitates the radical mechanism. Upon the construction of the energy landscape the S=5/2 state is indicative of proceeding via a radical mechanism. This high spin state is generated from the ground state via promotion of one $1\pi_x$ electron to a $2\pi_x$ orbital, representing the electron transfer from oxygen to metal.

There are two mechanisms of interest for this reaction, the 2+2 and radical mechanisms. The 2+2 mechanism is exhibited by the doublet and quartet spins. The first step is an interaction between the methane and niobium oxide molecules followed by the first transition state which forms a closed Nb–O–H–CH$_3$ structure before opening again at the CH$_3$–H bond, the CH bond

activation step. There is then a bond breaking disconnecting the H from the CH_3 group resulting in the combination of the OH group that will later make up methanol and in the second transition state the methanol group is fully formed though still bonded to the metal. This leads to the subsequent release of the metal, resulting in $Nb + CH_3OH$. The radical mechanism is exhibited by the sextet pathway. Previously the sextet was not considered due to its large separation in energy compared to the doublet and quartet spins, however the possibility of radical mechanism made the sextet analysis imperative. The radical mechanism begins in the same way as the 2+2, with the interaction of the methane and metal oxide. The combination into the first transition state differs greatly from the 2+2 mechanism however, as there is no bond connecting the CH_3 group back to the metal, and slightly resembles the intermediate between transition states 1 and 2 for the 2+2 mechanism. The difference in transition states can be seen in Figure 3.4. The intermediate step also differs greatly in that instead of a connected almost linear CH_3–Nb–O–H molecule there are two separate components $CH_3 + Nb$–OH which are then recombined in transition state 2 before the release of methanol from Nb. As mentioned previously there are three spins that undergo very different mechanisms for the conversion of methane to methanol via CH activation, is there any affect that spin has on the mechanism and how the process will go?
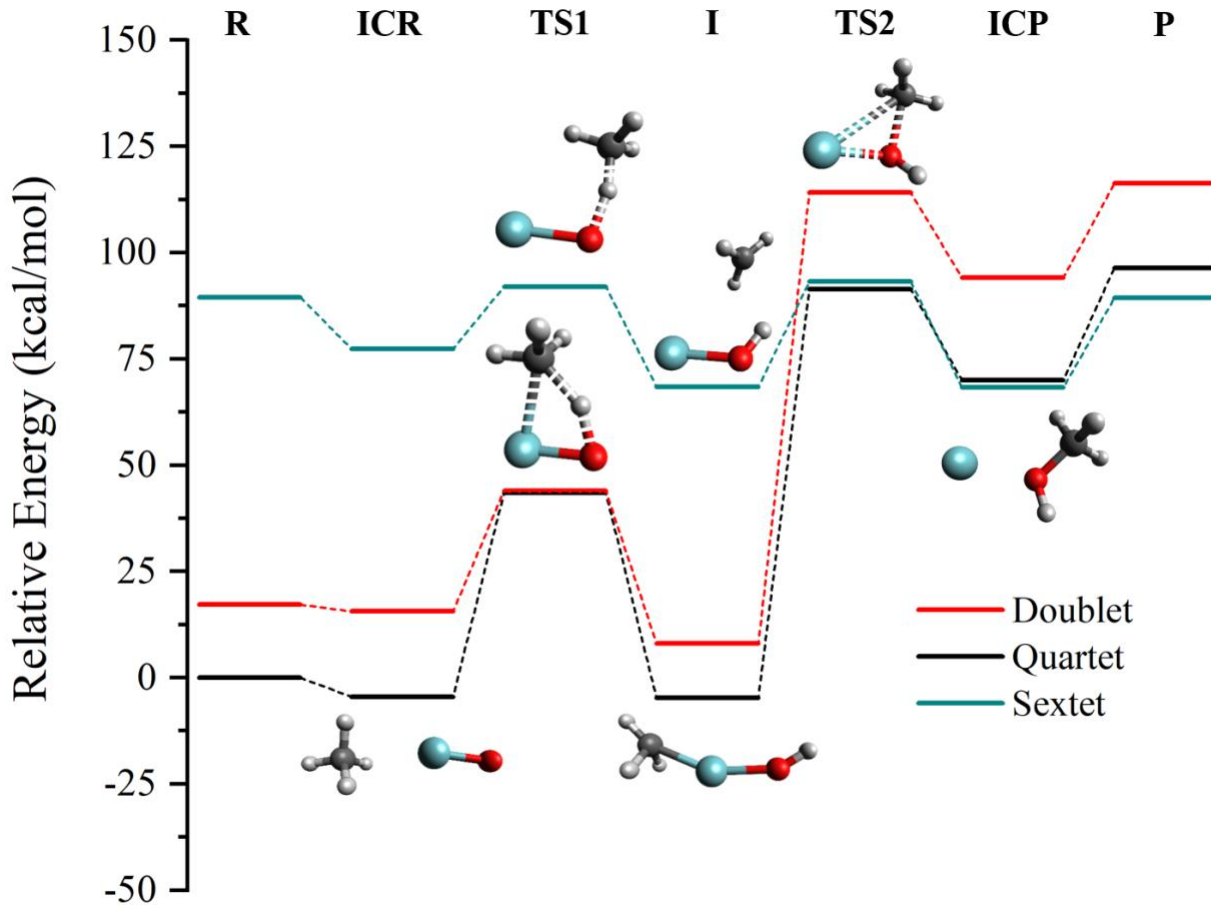
Figure 3.4: *Reaction Profile for NbO+CH₄→ Nb + CH₃OH*

4. Effect of spin on the energy landscape

During the electronic structure investigation, the S=5/2 states were incredibly high in energy compared to the S=1/2 and S=3/2 states, shown in Figure 3.1, and only further considered to explore the mechanistic ability of the high spin metal oxide pathway. Looking at the energy landscape in Figure 3.3 the lower spins, doublet and quartet, are much lower in energy than the sextet. Also, the doublet and quartet follow a different pathway, the 2+2 mechanism, than the sextet which proceeds down the radical pathway. As previously mentioned, the sextet state of NbO were much higher in energy than the lower spins that for the electronic structure discussion the

sextet was not considered reasonably attainable, however since it follows the radical mechanism this high spin pathway was included.

In terms of how the two mechanisms compare in terms of efficiency it can be broken down by spin. The doublet and quartet spins are the lowest energy pathways with the ground state reactants being the quartet. These spins undergo the 2+2 mechanism, and experience large energy barriers at both key steps, the CH bond activation and the OH reformation step. Alternatively, the sextet pathway undergoes the radical mechanism with small energy barriers at both key steps.

The ground state and lowest energy pathways were analyzed previously but the question remains: does the sextet spin pathway play a role in methane activation and if so, how? To answer this question three spins were considered for the reaction profile of NbO reacting with CH_4: doublet, quartet, and sextet.

The energy landscape is shown in Figure 3.3 lower spins, doublet and quartet, are the lowest energy pathways with ground state quartet followed by the doublet about 17 kcal/mol higher in energy. These pathways see a slight change to the intermediate complex but a 47.94 kcal/mol energy increase for the quartet and 28.34 kcal/mol difference for the doublet for the first transition state (CH activation step) resulting in comparable transition state energies (quartet only 0.5 kcal/mol lower). At the intermediate step (I) the quartet is stabilized over the doublet by ~12 kcal/mol, but to attain the second transition state about 100 and 125 kcal/mol is required for the doublet and quartet pathways respectively, and this energy remains rather constant through the product formation steps. The doublet and quartet 2+2 pathways result in endothermic products greater than ~100 kcal/mol above the reactant energy.

This all changes for the high spin radical pathway. Although it begins 89.46 kcal/mol above the quartet ground state the energy barriers are much lower. The energy required to proceed from

the reactant interacting complex to the first transition state is only 14.63 kcal/mol and only 24.71 kcal/mol needed to reach the second transition state from the intermediate step compared to the 106 kcal/mol and 96 kcal/mol required of the doublet and quartet 2+2 pathways respectively. It is at the second transition state step the sextet is stabilized of the quartet for the remainder of the reaction. The radical pathway yields an exothermic product only 0.111 kcal/mol lower than the reactants, and is stabilized over the quartet and doublet 2+2 pathways by 7.05 and 26.97 kcal/mol respectively. Both 2+2 pathways result in endothermic products that are ~96-99 kcal/mol above the reactants.

With this information we can see the direct impact of spin on the mechanisms. Generally, the low spins will proceed via the 2+2 pathway with selectivity for the CH bond of methane to be activated but at the expense of large energy barriers and yielding endothermic products. High spins however will generally proceed through the radical mechanism, which is much more efficient than the 2+2 counterpart and has much smaller barriers and an exothermic product. However, this mechanism does not have the selectivity for the CH bond of methanol that the 2+2 possesses.

The benefits of high spin metal oxides can aid in the development of a catalyst for the sake of efficiency, and low spin metal oxides for selectivity but could there exist a way for the selectivity and efficiency of both mechanisms to exist in one reaction?

As has been shown in this chapter the spin and metal oxygen character have an effect on the reactivity of methane to methanol transformation. Work with metal oxides and ligand effects have been studied with the zirconium oxide neutral complex and the iron oxide dication.[16,19]

5. Effect of Ligands on the Energy Landscape: The case of ZrO and FeO^{2+}

An additional factor for the stabilization of mechanistic pathways for methane to methanol transformation is the presence of a ligand. An analysis of ligand effects on a neutral metal oxide are discussed in Jackson et al where the reaction of zirconium oxide with methane for the formation of methanol was monitored for both non-ligated and ligated metal oxides.[16] In this study it was seen that a ligand can indeed stabilize one mechanism over another depending on the type of ligand utilized on which reaction. A weak field ligand is expected to stabilize an oxyl metal oxide (M^{3+}O$^{•-}$) over the oxo via a radical mechanism.
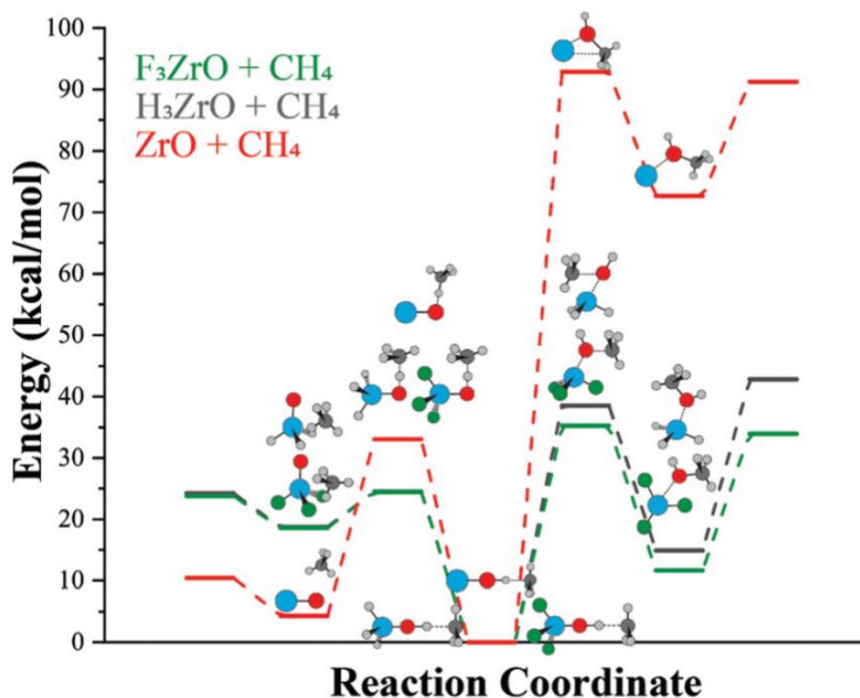
Figure 3.5: *Reaction Profile for ZrO + CH₄ ligated and non-ligated pathways*[16]

In Figure 3.5 the reaction of ZrO with methane is shown with a non-ligated pathway, a hydrogen ligated pathway representing a strong field ligand system, and a fluorine ligated pathway representing a weak field ligated pathway. In the reactant interacting complex the non-ligated

pathway is lowest in energy and the ligated pathways are nearly degenerate, in the C-H bond activation step the ligated pathways are stabilized over the non-ligated mechanism and again degenerate, in the bond reformation step there is an energetic separation of the ligated paths with the fluorine ligated path more stabilized for the remainder of the reaction but both ligated mechanisms stabilized more over the non-ligated pathways indicating the presence of ligands can affect the mechanistic behavior of the catalyst.

Another ligand study was completed by Kirkland, Khan, et al which saw the effects of ligands on a transition metal oxide dication.[19] Figure 3.6 displays the potential energy curves for the bare iron oxide dication and additional potential energy curves with two different ligand, ammonia and water. It is shown that a ligand such as water that lies in the middle of the spectrochemical series draws the oxo state from the bare metal oxide lower in energy, but the strong field ligand ammonia, further stabilizes the oxo state as the ground state of the system.
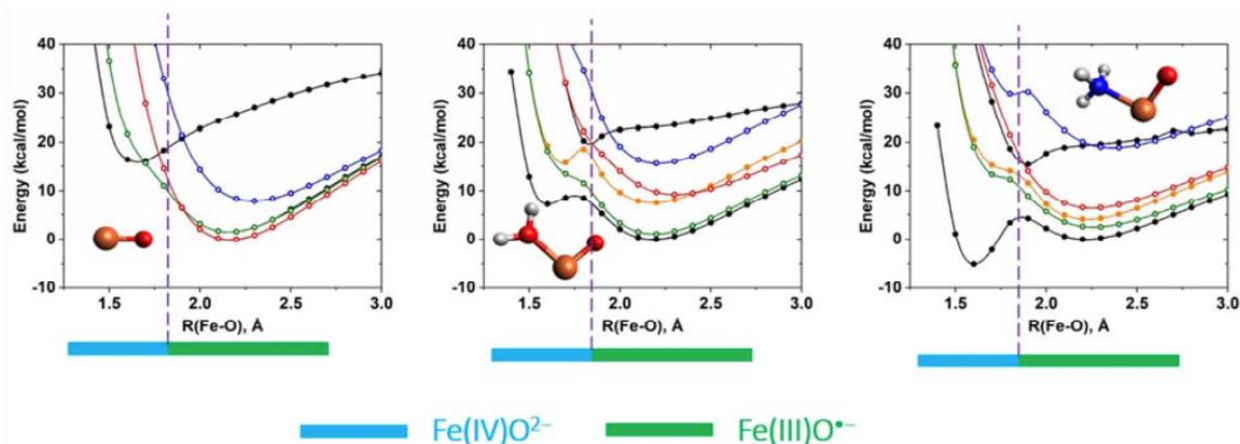
Figure 3.6: *Potential Energy Curves for FeO^{2+}, and ligand induced effects* [19]

A similar finding would be expected if the niobium oxide catalyst was bonded with weak field ligands. It was mentioned previously that the weak field ligands facilitate the radical mechanism, which seen previously for the NbO system is characterized by low energy barriers for the key steps and results in an exothermic product. Shown in Figure 3.7 is the oxo and oxyl form

of niobium oxide. The oxo form will have three available electrons to bond with chlorine ligands, and a fourth will remain in the periphery taking on the electron density held by oxygen. The oxyl form possesses another electron allowing it to bind to a fourth chlorine ligand which will stabilize this form over the oxo.
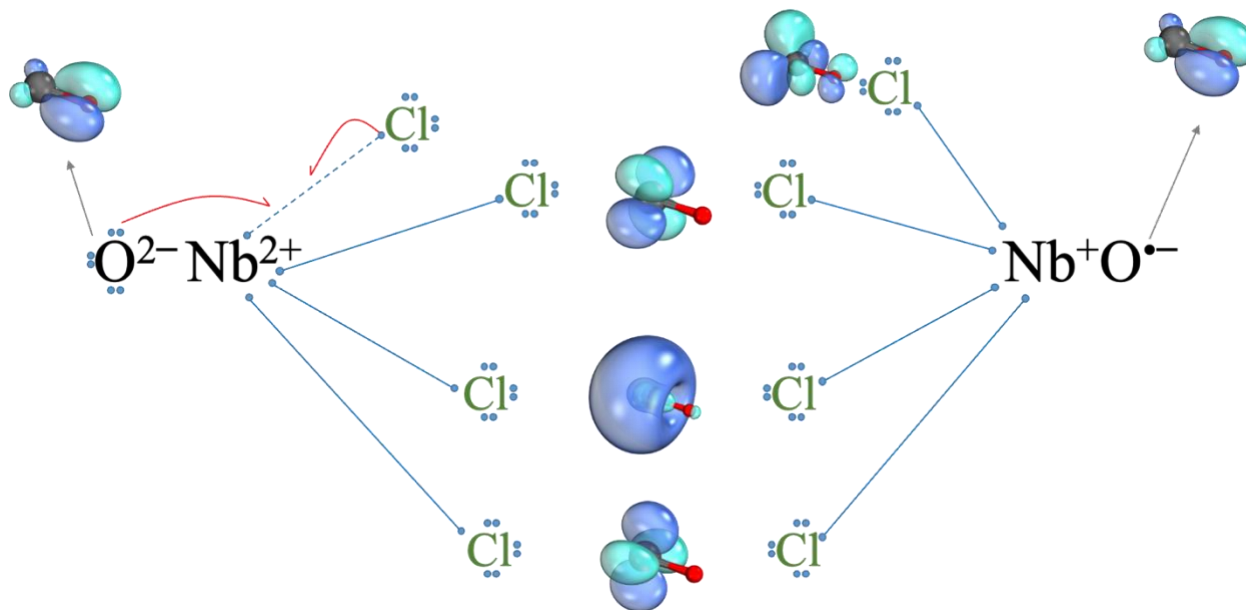
Figure 3.7: *Oxo and oxyl form of NbO stabilized with chlorine ligands*

Using metal oxide dications provides another pathway to influence mechanistic behavior, the electronic structure of the first-row transition metal oxide dications is discussed in Chapter 4. Ligand effects on the electronic structure and reactivity of these electron poor metal oxides are discussed in Chapter 5.

1   J. G. De Vries and S. D. Jackson, *Catal Sci Technol*, 2012, 2, 2009.

2   Process for the Manufacture of Methyl-alcohol from Methane, 1905.

3   E. H. Boomer and V. Thomas, THE OXIDATION OF METHANE AT HIGH PRESSURES: III. EXPERIMENTS USING PURE METHANE AND PRINCIPALLY COPPER AS CATALYST, *Can J Res*, 1937, **15b**, 414–433.

4   R. B. Anderson, K. C. Stein, J. J. Feenan and L. J. E. Hofer, Catalytic Oxidation of Methane, *Ind Eng Chem*, 1961, **53**, 809–812.

5   R. A. Periana, X. Y. Liu and G. Bhalla, Novel bis-acac-O,O-Ir(III) catalyst for anti-Markovnikov, hydroarylation of olefins operates by arene CH activation, *Chemical Communications*, 2002, 3000–3001.

6   C. N. R. Rao, Transition Metal Oxides, *Annu. Rev. Phys. Chem*, 1989, **40**, 291–326.

7   S. Sader and E. Miliordos, Being negative can be positive: metal oxide anions promise more selective methane to methanol conversion, *Physical Chemistry Chemical Physics*, 2022, **24**, 21583–21587.

8   S. N. Khan and E. Miliordos, Electronic Structure of RhO2+, Its Ammoniated Complexes (NH3)1-5RhO2+, and Mechanistic Exploration of CH4Activation by Them, *Inorg Chem*, 2021, **60**, 16111–16119.

9   I. R. Ariyarathna and E. Miliordos, Ab initio investigation of the ground and excited states of MoO+,2+,- and their catalytic strength on water activation, *Physical Chemistry Chemical Physics*, 2018, **20**, 12278–12287.

10   I. R. Ariyarathna and E. Miliordos, Ab initio investigation of the ground and excited states of TcO+ and RhO+, *J Quant Spectrosc Radiat Transf*, , DOI:10.1016/j.jqsrt.2022.108074.

11   I. R. Ariyarathna and E. Miliordos, Ab initio investigation of the ground and excited states of ZrO+ and NbO+, *J Quant Spectrosc Radiat Transf*, , DOI:10.1016/j.jqsrt.2020.107265.

12   C. N. Sakellaris, E. Miliordos and A. Mavridis, First principles study of the ground and excited states of FeO, FeO +, and FeO-, *Journal of Chemical Physics*, , DOI:10.1063/1.3598529.

13   I. R. Ariyarathna, N. M. S. Almeida and E. Miliordos, Ab initio investigation of the ground and excited states of RuO+,0,-and their reaction with water, *Physical Chemistry Chemical Physics*, 2020, **22**, 16072–16079.

14   N. M. S. Almeida, I. R. Ariyarathna and E. Miliordos, O-H and C-H Bond Activations of Water and Methane by RuO2+ and (NH3)RuO2+: Ground and Excited States, *Journal of Physical Chemistry A*, 2019, **123**, 9336–9344.

15   N. M. S. Almeida, I. R. Ariyarathna and E. Miliordos, Ab initio calculations on the ground and excited electronic states of neutral and charged palladium monoxide, PdO0,+,-, *Physical Chemistry Chemical Physics*, 2018, **20**, 14578–14586.

16   B. A. Jackson and E. Miliordos, Weak-field ligands enable inert early transition metal oxides to convert methane to methanol: The case of ZrO, *Physical Chemistry Chemical Physics*, 2020, **22**, 6606–6618.

17   E. E. Claveau and E. Miliordos, Quantum chemical calculations on NbO and its reaction with methane: Ground and excited electronic states, *Physical Chemistry Chemical Physics*, 2019, **21**, 26324–26332.

18   S. N. Khan and E. Miliordos, Methane to Methanol Conversion Facilitated by Transition-Metal Methyl and Methoxy Units: The Cases of FeCH3+ and FeOCH3+, *Journal of Physical Chemistry A*, 2019, **123**, 5590–5599.

19 J. K. Kirkland, S. N. Khan, B. Casale, E. Miliordos and K. D. Vogiatzis, Ligand field effects on the ground and excited states of reactive FeO2+ species, *Physical Chemistry Chemical Physics*, 2018, **20**, 28786.

20 E. Miliordos and A. Mavridis, Electronic structure and bonding of the early 3d-transition metal diatomic oxides and their ions: ScO0,±, TiO0,±, CrO0,±, and MnO0,±, *Journal of Physical Chemistry A*, 2010, **114**, 8536–8572.

21 E. E. Claveau and E. Miliordos, Electronic structure of the dicationic first row transition metal oxides, *Physical Chemistry Chemical Physics*, 2021, **23**, 21172–21182.

22 E. E. Claveau, S. Sader, B. A. Jackson, S. N. Khan and E. Miliordos, Transition metal oxide complexes as molecular catalysts for selective methane to methanol transformation: Any prospects or time to retire?, *Physical Chemistry Chemical Physics*, 2023, **25**, 5313.

23 C. Nico, T. Monteiro and M. P. F. Graça, Niobium oxides and niobates physical properties: Review and prospects, *Prog Mater Sci*, 2016, **80**, 1–37.

24 K. Kim, S. G. Woo, Y. N. Jo, J. Lee and J. H. Kim, Niobium oxide nanoparticle core–amorphous carbon shell structure for fast reversible lithium storage, *Electrochim Acta*, 2017, **240**, 316–322.

25 F. Nakagomi, S. E. Cerruti, M. R. de Freitas, E. S. Freitas Neto, F. V. de Andrade and G. O. Siqueira, Niobium pentoxide produced by a novel method microwave assisted combustion synthesis, *Chem Phys Lett*, 2019, **729**, 37–41.

26 N. P. de Moraes, F. N. Silva, M. L. C. P. da Silva, T. M. B. Campos, G. P. Thim and L. A. Rodrigues, Methylene blue photodegradation employing hexagonal prism-shaped niobium oxide as heterogeneous catalyst: Effect of catalyst dosage, dye concentration, and radiation source, *Mater Chem Phys*, 2018, **214**, 95–106.

27 N. T. do Prado and L. C. A. Oliveira, Nanostructured niobium oxide synthetized by a new route using hydrothermal treatment: High efficiency in oxidation reactions, *Appl Catal B*, 2017, **205**, 481–488.

28 D. E. Woon and T. H. Dunning, Gaussian basis sets for use in correlated molecular calculations. III. The atoms aluminum through argon, *J Chem Phys*, 1993, **98**, 1358.

29 T. H. Dunning, Gaussian basis sets for use in correlated molecular calculations. I. The atoms boron through neon and hydrogen, *J Chem Phys*, 1989, **90**, 1007–1023.

30 R. A. Kendall, T. H. Dunning and R. J. Harrison, Electron affinities of the first-row atoms revisited. Systematic basis sets and wave functions, *J Chem Phys*, 1992, **96**, 6796–6806.

31 K. A. Peterson, D. Figgen, M. Dolg and H. Stoll, Energy-consistent relativistic pseudopotentials and correlation consistent basis sets for the 4d elements Y-Pd, *Journal of Chemical Physics*, 2007, **126**, 124101.

32 R. D. Amos, J. S. Andrews, N. C. Handy, P. J. Knowles, J. S. Andrews, R. D. Amos, N. C. Handy, J. A. Pople, C. Hampel, H.-J. Werner, N. C. Handy, H.-J. Werner, P. J. Knowles, G. Knizia, F. R. Manby, M. Schütz, P. Celani, W. Györffy, D. Kats, T. Korona, R. Lindh, A. Mitrushenkov, G. Rauhut, K. R. Shamasundar, T. B. Adler, R. D. Amos, A. Bernhardsson, A. Berning, D. L. Cooper, M. J. O. Deegan, A. J. Dobbyn, F. Eckert, E. Goll, C. Hampel, A. Hesselmann, G. Hetzer, T. Hrenar, G. Jansen, C. Köppl, Y. Liu, A. W. Lloyd, R. A. Mata, A. J. May, S. J. McNicholas, W. Meyer, M. E. Mura, A. Nicklass, D. P. O'Neill, P. Palmieri, D. Peng, K. Pflüger, R. Pitzer, M. Reiher, T. Shiozaki, H. Stoll, A. J. Stone, R. Tarroni, T. Thorsteinsson, M. Wang and others, MOLPRO, version 2015.1, a package of ab initio programs, *Chem. Phys. Letters*, , DOI:10.1063/1.448627.

33   M. J. ; T. Frisch G. W.; Schlegel, H. B.; Scuseria, G. E.; Robb, M. A.; Cheeseman, J. R.; Scalmani, G.; Barone, V.; Petersson, G. A.; Nakatsuji, H.; Li, X.; Caricato, M.; Marenich, A. V.; Bloino, J.; Janesko, B. G.; Gomperts, R.; Mennucci, B.; Hratch, D. J., Gaussian 16, Rev. B.01, *Gaussian, Inc., Wallingford, CT*.

34   H. S. Yu, X. He, S. L. Li and D. G. Truhlar, MN15: A Kohn-Sham global-hybrid exchange-correlation density functional with broad accuracy for multi-reference and single-reference systems and noncovalent interactions, *Chem Sci*, 2016, **7**, 5032–5051.

35   D. E. Woon and T. H. Dunning, Gaussian basis sets for use in correlated molecular calculations. IV. Calculation of static electrical response properties, *J Chem Phys*, 1994, **100**, 2975–2988.

36   A. Kramida, Ralchenko and J. Reader, NIST Atomic Spectra Database .

37   G. Wang, S. Lai, M. Chen and M. Zhou, Matrix isolation infrared spectroscopic and theoretical studies on the reactions of niobium and tantalum mono- and dioxides with methane, *Journal of Physical Chemistry A*, 2005, **109**, 9514–9520.

38   K. J. De Almeida, T. C. Silva, J. L. Neto, M. V. J. Rocha, T. C. Ramalho, M. N. De Miranda and H. A. Duarte, Methane C-H bond activation by niobium oxides: Theoretical analyses of the bonding and reactivity properties of Nbo mn+ (m = 1, 2; N = 0, 1, 2), *J Organomet Chem*, 2016, **802**, 49–59.

39   Y. Cao, X. Zhao, B. Xin, S. Xiong and Z. Tang, Reactions of M+ and MO+(M = V, Nb, Ta) with methanol, *Journal of Molecular Structure: THEOCHEM*, 2004, **683**, 141–146.

Chapter 4: Electronic Structure of Transition Metal Oxide Dications

Dications are unique complexes in that the removal of two electrons allows for both the oxo and oxyl forms of the metal oxide to be potential catalytic candidates due to the comparable second ionization energy of the metal and first ionization of oxygen. The oxo form possesses a closed shell on oxygen ($M^{4+}O^{2-}$), and the oxyl form ($M^{3+}O^{\bullet-}$) an unpaired electron on oxygen.[1] These complexes are special in natural processes such as heme iron, enzymes, where the Fe(IV) oxo unit plays a large role in the C-H bond clevage.[2,3] Nature chooses dications for these processes since it has an easy path for the switching between oxo and oxyl. The manganese complex with Mn(II) and Mn(IV) oxidation states has been shown to be important for biological redox reactions as the high valent Mn oxo plays an important role in the activation of certain enzymes.[4] Metalloenzymes have been shown to be successful for the biological activation of C-H bonds through the use of abundant and cheap transition metals such as iron, copper, and manganese according to Ray *et. al.*[5] Hohenberger *et. al.* and Ye *et. al.* both show the C-H activation using high valent iron oxo complexes.[6,7] The iron oxo unit is one of the most widely studied transition metal oxide dications due to its presence in the intermediate forms of enzymes.[8] Recently the stability of vanadyl complexes under biological conditions lead to the prospect of obtaining crystal structures of the ferryl analog to map proteins.[9] This finding from Martinie *et. al.* indication vanadyl has the capability to be an analog of the ferryl intermediate with both structural and behavioral mimicry allowed for its use as a viable crystallographic tool to be generally applied to other enzymes.[9,10]

Transition metal oxide dications (TMO^{2+}) are considered potential catalysts due to the popularity and success of transition metal catalysts seen in the literature both theoretically and

experimentally and have been shown to efficiently activate the C-H bonds of saturated hydrocarbons. As seen in Chapter 3 the oxo and oxyl forms of the metal oxide can cause the reaction to proceed through a different mechanism. For example, the quartet of NbO of the oxo form ($Nb^{2+}O^{2-}$) proceeded down a 2+2 mechanism characterized by large barriers and an endothermic product, however the sextet NbO of oxyl character ($Nb^{3+}O^{\bullet-}$) causes the reaction with methane to proceed via a radical mechanism characterized by low energy barriers resulting in a favorable exothermic product.[11] It is possible with the dication that a sufficient ideal catalyst can be designed for a process depending on the need. If there is a need for selectivity for the CH bond of methane then an oxo dication can be used, but if efficiency is of utmost importance an oxyl dication can be used.

In order to determine their ability as catalysts to apply to methane to methanol transformation; we first need to understand the behavior of non-ligated first row transition metal oxide dications to classify the ground and excited states as either oxo or oxyl and understand any supposed trends across the row that may guide the catalyst development process. Herein we use *ab initio* techniques to investigate and describe the electronic structure for these complexes. Methods and results are discussed below and serve as a prequel to the reaction dynamics presented in future chapters.

1. Computational Techniques

Analysis of the electronic structure of the first-row transition metal oxide dications required the use of multireference techniques to solve the electronic Schrödinger equation due to the complexity of the wavefunction and the systems at hand.[12,13] CASSCF calculations were used to obtain the first order reference wavefunction. A nine orbital active space was chosen for the TMO^{2+} systems composed of the three 2p orbitals of oxygen, the 4s orbital of the metal, and the

3d orbital of the metal. Similar to the cationic, neutral, and anionic metal oxides the 2s of oxygen in the dications has little occupation therefore it is not included in the active. The 4s of the metal is included due to minimal occupation at CASSCF and is exchanged with other minimally populated orbitals of the metal of the same symmetry, which is expected since the metal has a 2+, 3+, or 4+ oxidation state which would not populate this 4s orbital, but it was kept to ensure no electronic states would be missing. MRCI was completed on top of CASSCF, using the reference wavefunction, allowing single and double promotions to the virtual space from the active space. Herein the dynamic correlation from the 2s electron on oxygen is included. Additional MRCI calculations including electron correlation of the $3s^2 3p^6$ metal electrons were completed (C-MRCI). MRCI+Q calculations were also completed to allow for the Davidson correction to remedy the size-extension of both MRCI and C-MRCI.[14]

Multireference analysis was completed using two different basis sets. Exploratory calculations and full potential energy curves (PEC) were done with cc-pVTZ on the metal, and aug-cc-pVTZ on the oxygen to accurately describe the polarized nature of the metal-oxygen bond.[15–18] Spectroscopic constant and additional numerical data were completed with a cc-pV5Z on the metal and aug-cc-pV5Z on oxygen.[15–18] Calculations at the C-MRCI level utilize the cc-pwCV5z weighted core basis for the metal.[15] CASSCF and MRCI calculations were completed using MOLPRO 2015 software.[17–20]

2. Electronic Structure

This study focused on the electronic structure analysis of the first-row transition metal oxide dications from titanium to copper in order to try and classify their behavior to understand potential catalytic activity for methane to methanol transformation. The investigation allowed for both the ground and excited states of the metal oxide dications to be classified as either oxo or

oxyl, characterized by either a closed shell oxygen or unpaired electron on oxygen respectively.[1] The results can be broken down into three groups based on their behavior and will be discussed in these groupings. Figure 4.1 shows the first oxo and oxyl electronic states for each of the first-row transition metal oxide dications. Solid lines correspond to oxo states, and dashed to oxyl. Titanium oxide dication has an oxo ground state ($^1\Sigma^+$) separated by ~55 kcal/mol from the $^1\Phi$ 1st excited state. Vanadium takes on a very similar behavior to its predecessor, oxo ground state ($^2\Delta$) and oxyl excited state ($^2\Pi$) about 55 kcal/mol higher in energy with a 0.138 Å bond elongation from oxo to oxyl. It is important to mention for these two metals that all states aside from the ground state are of oxyl character (full PEC for all metals discussed can be found in Appendix A). A shift in behavior occurs for the chromium oxide dication, where not all excited states are of oxyl character. The ground state ($^3\Sigma^-$) is oxo with a 1.529 Å metal oxygen distance typical of the early transition metal oxo states, however according to the full PEC in Appendix A the first excited state is a low lying (~11197 cm^{-1}) oxo $^1\Gamma$ state, the first oxyl state ($^5\Sigma^-$) lies 13100 cm^{-1} above the ground state with a metal oxygen bond distance 0.346 Å longer than the oxo ground state.

Manganese is the first representative metal from the middle transition metal family. The MnO^{2+} ground state is a $^4\Sigma^-$ of oxyl character with a metal oxygen bond length greater than 2 Å, and about 60 kcal/mol above the ground state lies the $^2\Delta$ oxo excited state which has a 0.683 Å small metal oxygen distance. Iron follows a similar pattern with the oxyl $^3\Delta$ ground state and oxo excited state ($^5\Sigma^+$) significantly lower in energy than the oxo counterpart for manganese.

The late transition metals, cobalt, nickel, and copper, have a very different story than the previously mentioned metal oxide dications. These three metals are characterized as having only oxyl states. CASSCF calculations for each metal were completed with ~30 states and all returned oxyl components. The only exception to this is a shoulder for one of the cobalt curves around 1.6

Å, when the CI vector was gathered for this distance, it was an oxo component which can potentially be drawn out with a strong field ligand and stabilized. All three metals have long metal oxygen bond distances ranging from 1.945-2.105 Å also indicative of an oxyl state.

These findings can be summarized breaking the metals into three groups: early, middle, and late transition metal oxide dications. Early TMO^{2+} consists of titanium, vanadium, and chromium are characterized as having oxo ground states and oxyl excited states, with ground states corresponding to $M^{4+}O^{2-}$. Middle TMO^{2+} are composed of manganese and iron where there exist oxyl ground states followed by low lying excited states indicating the likelihood of stabilization of one over the other; $M^{4+}O^{2-} \Leftrightarrow M^{3+}O^{\bullet-}$. Late TMO^{2+} are those with only oxyl states, cobalt, nickel, and copper where the configuration switches between the following: $M^{3+}O^{\bullet-} \Leftrightarrow M^{2+}O^{\bullet\bullet-}$. A note on chromium however, since there exists low lying oxyl states in this metal oxide it is almost a hybrid of the early and middle transition metals, where the close proximity of oxo and oxyl like in the middle transition metals may make it a good catalytic candidate.
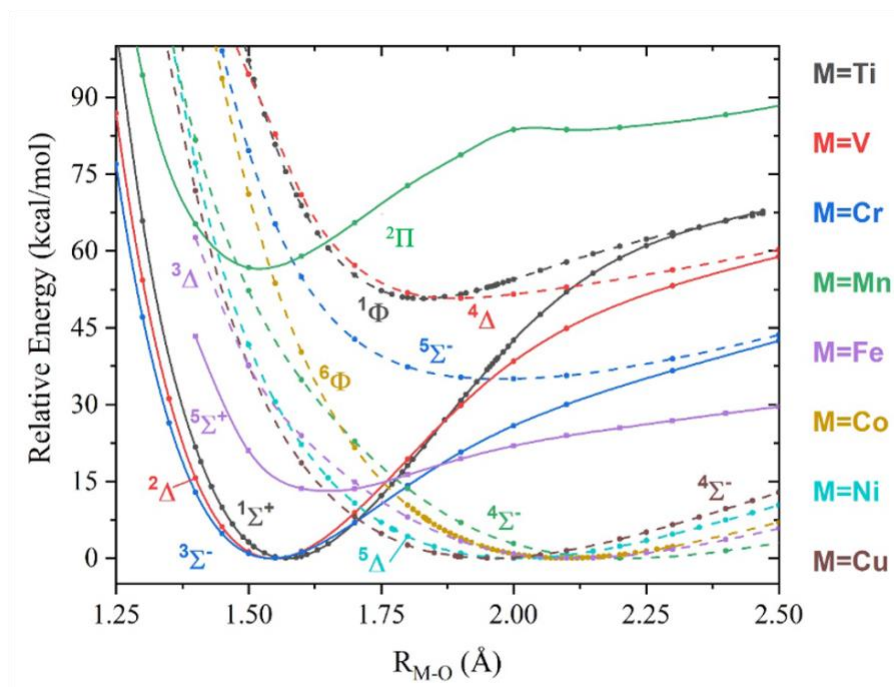
Figure 4.1: *Potential energy curves for oxo and oxyl states of first row TMO^{2+}*

In the table below the CI vectors for the curves displayed in Figure 4.1 are shown and differentiated by oxo and oxyl by metal, states listed in blue correspond to the ground state of the system, information for iron was gathered from Kirkland *et. al.*[21]

Table 4.1*: Electron configuration of oxo and oxyl component of analyzed* TMO^{2+}

	Oxo ($M^{4+}O^{2-}$)	Oxyl ($M^{3+}O^{\bullet-}$)
TiO^{2+}	$^1\Sigma^+ \rightarrow 1\sigma^2\,1\pi_x^2\,1\pi_y^2$	$^1\Phi \rightarrow 1\sigma^2\,1\pi_x^2\,1\pi_y^\beta\,\delta_{xy}^\alpha$
VO^{2+}	$^2\Delta \rightarrow 1\sigma^2\,1\delta_{x^2-y^2}^{2\alpha}\,1\pi_x^2\,1\pi_y^2$	$^4\Delta \rightarrow 1\sigma^2\,1\pi_x^\alpha\,2\pi_x^\beta 1\pi_y^\beta\,\delta_{xy}^\alpha$
CrO^{2+}	$^3\Sigma^- \rightarrow 1\sigma^2\,1\delta_{x^2-y^2}^{2\alpha}\,1\pi_x^2\,1\pi_y^2\,1\delta_{xy}^\alpha$	$^5\Sigma^- \rightarrow 1\sigma^2\,1\delta_{x^2-y^2}^{2\alpha}\,1\pi_x^\beta 2\pi_x^\alpha\,1\pi_y^\alpha\,2\pi_y^\alpha\,\delta_{xy}^\alpha$
MnO^{2+}	$^2\Delta \rightarrow 1\sigma^2\,1\delta_{x^2-y^2}^{2\alpha}\,1\pi_x^2\,1\pi_y^2\,2\pi_y^\beta\,\delta_{xy}^\alpha$	$^4\Sigma^- \rightarrow 1\sigma^2\,1\delta_{x^2-y^2}^{2\alpha}\,1\pi_x^\beta\,2\pi_x^\alpha\,1\pi_y^\beta\,2\pi_y^\alpha\,\delta_{xy}^\alpha$
FeO^{2+}	$^5\Sigma^+ \rightarrow 1\sigma^2\,2\sigma^2\,1\pi_x^2\,2\pi_x^\alpha\,1\pi_y^2\,2\pi_y^\alpha\,1\delta_+^\alpha 1\delta_-^\alpha$	$^3\Delta \rightarrow 1\sigma^2\,2\sigma^2\,3\sigma^\alpha\,1\pi_x^\beta\,2\pi_x^\alpha 1\pi_y^\beta\,2\pi_y^\alpha\,1\delta_+^\alpha\,1\delta_-^2$
CoO^{2+}	N/A	$^6\Phi \rightarrow 1\sigma^\alpha\,1\sigma_{x^2-y^2}^{2\alpha}\,2\sigma^2\,1\pi_x^2\,2\pi_x^2\,1\pi_y^\alpha\,2\pi_y^\alpha\,1\delta_{xy}^\alpha$
NiO^{2+}	N/A	$^5\Delta \rightarrow 1\sigma^\alpha\,1\delta_{x^2-y^2}^{22}\,2\sigma^2\,1\pi_x^2\,2\pi_x^\alpha\,1\pi_y^2\,2\pi_y^\alpha\,1\delta_{xy}^\alpha$
CuO^{2+}	N/A	$^4\Sigma^- \rightarrow 1\sigma^\alpha 1\delta_{x^2-y^2}^{22}\,2\sigma^2\,1\pi_x^2\,2\pi_x^\alpha\,1\pi_y^2\,2\pi_y^\alpha\,1\delta_{xy}^2$

Here the distinction between the three groups of transition metal oxide dications can be clearly distinguished as the oxo character (double occupation in the π orbitals) is slowly being phased out. Early transition metals have distinct oxo ground states with oxyl excited states. Middle transition metals characterize the ground states as oxyl, and the oxo states are excited states. Late transition metals see no participation of oxo states in the systems and complete the phasing out of oxo character. With this in mind we can adjust the structure of the known oxo wall. Traditionally, the wall has been placed between iron and cobalt indicating the change in character. While this wall still exists based on our analysis however another wall is placed between chromium and manganese to indicate the shift from oxo ground state to oxyl ground state while retaining oxo states as excited states.

3. Differences in trends

Proceeding down the first-row transition metals as the character changes from oxo to oxyl so does several other aspects, including but not limited to the metal oxygen bond length and orbital behavior.

3.1 Metal oxygen bond length

Perhaps an easy way to monitor the behavior of metal oxide dications is through the metal oxygen bond length. Generally, the bond length for oxo states is shorter than that of the oxyl states, but by how much and can a generalization be made across the row?

In the early transition metals titanium and vanadium it is easiest to see the metal oxygen bond length differentiation as there is significant separation between the oxo states and the oxyl states. The ground state for these metals is oxo and separated from the oxyl excited state by at least 55 kcal/mol. In the case of TiO^{2+}, the oxo $^1\Sigma^+$ ground state has a bond length of 1.554 Å and the oxyl first excited states possess bond lengths around 1.804 Å, a 0.24 Å elongation from ground to first excited state. The excited states of TiO^{2+} are all of oxyl character and average a 1.799 Å bond length, indicating a 1.799 ± 0.005 Å generalization. VO^{2+} at MRCI has an elongation of 0.138 Å from $^2\Delta$ ground state to $^4\Delta$ 1st excited state at MRCI. The higher density of states in the chromium oxide dication makes characterization a little more difficult as the oxo and oxyl separation is not as clear as the previous two metals. Nonetheless the oxo states range from 1.507 to 1.622 Å according to the CI vectors and the oxyl from 1.975-2.202Å.

Manganese sees the opposite happen from chromium, with oxyl ground and low-lying excited states and oxo excited states. The oxyl states range from 2.191 to 2.28 Å with the oxo states approximately 0.6 Å shorter ranging from 1.508 to 1.64Å. Lastly, the late transition metals, cobalt

nickel and copper are all of oxyl character and bond lengths range from 1.945 Å to 2.079 Å with decreasing metal oxygen distance from cobalt to copper.

3.2 Orbital Behavior

The orbital shapes change across the first-row transition metals. Actual orbitals occupying the active space remain the same however, the orbital behavior from titanium to copper give additional insight into their bonding behavior. Shown in Figure 4.2 is the active orbitals in this study for a representative metal of the early, middle and late transition metals.

These orbitals are shown at specific bond lengths 1.6 Å for early, and 2.0 Å for late. For the orbitals shown it is easily observed that int the early metals the orbital is localized across the bond between the metal and oxygen whereas the late transition metal representative, nickel, has more localization of the π orbitals on either the metal or on the oxygen, with no mixing along the bond. The other major difference comes in

Figure 4.2: *Early transition metal vs. late transition metal active orbitals*

the π* and σ* orbitals, in the early transition metals the π* orbital has most the orbital density around the metal with a small portion on the oxygen, but for the late transition metal the orbital density is placed solely on oxygen. The σ* orbital sees something similar, in the early transition metals the orbital density is very similar to that of the sigma bonding orbital spanning almost equally across the metal oxygen bond, but for the late transition metals, the orbital density is places almost exclusively on the metal with very little on the oxygen.

4. Oxo vs Oxyl character for ligand

With an understanding of the electronic structure of these metal oxide dications adjustments can be made to their behavior through the introduction of ligands to stabilize one form over the other as was mentioned in the previous chapter. Ligands are chosen from the spectrochemical series, a list of ligands ranking their interactions with metal ions. It has been shown in the literature that strong field ligands stabilize the oxo forms of the metal oxide and weak field ligands stabilize the oxyl forms.[21]

The effects of strong field ligands will be addressed in the next chapter, again looking into the electronic structure of the complexes followed by an analysis into their reactivity with methane.

1   Y. Shimoyama and T. Kojima, Metal-Oxyl Species and Their Possible Roles in Chemical Oxidations, *Inorg Chem*, 2019, **58**, 9517–9542.

2   C. Krebs, D. G. Fujimori, C. T. Walsh and J. M. Bollinger, in *Accounts of Chemical Research*, 2007, vol. 40, pp. 484–492.

3   A. Bassan, M. R. A. Blomberg, T. Borowski and P. E. M. Siegbahn, *J Inorg Biochem*, 2006, 100, 727–743.

4   M. Balamurugan, N. Saravanan, H. Ha, Y. H. Lee and K. T. Nam, *Nano Converg*, 2018, 5.

5   K. Ray, F. F. Pfaff, B. Wang and W. Nam, Status of reactive non-heme metal-oxygen intermediates in chemical and enzymatic reactions, *J Am Chem Soc*, 2014, **136**, 13942–13958.

6   J. Hohenberger, K. Ray and K. Meyer, The biology and chemistry of high-valent iron-oxo and iron-nitrido complexes, *Nat Commun*, 2012, **3**, 1–13.

7   S. Ye and F. Neese, Nonheme oxo-iron(IV) intermediates form an oxyl radical upon approaching the C-H bond activation transition state, *Proceedings of the National Academy of Sciences*, 2010, **108**, 1228–1233.

8   V. C. C. Wang, S. Maji, P. P. Y. Chen, H. K. Lee, S. S. F. Yu and S. I. Chan, *Chem Rev*, 2017, 117, 8574–8621.

9   R. J. Martinie, C. J. Pollock, M. L. Matthews, J. M. Bollinger, C. Krebs and A. Silakov, Vanadyl as a Stable Structural Mimic of Reactive Ferryl Intermediates in Mononuclear Nonheme-Iron Enzymes, *Inorg Chem*, 2017, **56**, 13382–13389.

10   A. J. Mitchell, N. P. Dunham, R. J. Martinie, J. A. Bergman, C. J. Pollock, K. Hu, B. D. Allen, W. C. Chang, A. Silakov, J. M. Bollinger, C. Krebs and A. K. Boal, Visualizing the reaction cycle in an Iron(II)- and 2-(Oxo)-glutarate-dependent hydroxylase, *J Am Chem Soc*, 2017, **139**, 13830–13836.

11   E. E. Claveau and E. Miliordos, Quantum chemical calculations on NbO and its reaction with methane: Ground and excited electronic states, *Physical Chemistry Chemical Physics*, 2019, **21**, 26324–26332.

12   D. F. Leto, A. A. Massie, D. B. Rice and T. A. Jackson, Spectroscopic and Computational Investigations of a Mononuclear Manganese(IV)-Oxo Complex Reveal Electronic Structure Contributions to Reactivity, *J Am Chem Soc*, 2016, **138**, 15413–15424.

13   H. Johansen and K. Tanaka, Ab initio RHF, CI, and MC SCF calculations on the vanadyl ion, *Chem Phys Lett*, 1985, **116**, 155–159.

14   S. R. Langhoff and E. R. Davidson, Configuration interaction calculations on the nitrogen molecule, *Int J Quantum Chem*, 1974, **8**, 61–72.

15   N. B. Balabanov and K. A. Peterson, Systematically convergent basis sets for transition metals. I. All-electron correlation consistent basis sets for the 3d elements Sc-Zn, *Journal of Chemical Physics*, 2005, **123**, 064107.

16   R. A. Kendall, T. H. Dunning and R. J. Harrison, Electron affinities of the first-row atoms revisited. Systematic basis sets and wave functions, *J Chem Phys*, 1992, **96**, 6796–6806.

17   T. H. Dunning, Gaussian basis sets for use in correlated molecular calculations. I. The atoms boron through neon and hydrogen, *J Chem Phys*, 1989, **90**, 1007–1023.

18   D. E. Woon and T. H. Dunning, Gaussian basis sets for use in correlated molecular calculations. IV. Calculation of static electrical response properties, *J Chem Phys*, 1994, **100**, 2975–2988.

19   D. E. Woon and T. H. Dunning, Gaussian basis sets for use in correlated molecular calculations. III. The atoms aluminum through argon, *J Chem Phys*, 1993, **98**, 1358.

20   H.-J. Werner and P. J. Knowles, MOLPRO, version 2015.1, a package of ab initio programs, *Chem. Phys. Letters*, , DOI:10.1063/1.448627.

21   J. K. Kirkland, S. N. Khan, B. Casale, E. Miliordos and K. D. Vogiatzis, Ligand field effects on the ground and excited states of reactive FeO2+ species, *Physical Chemistry Chemical Physics*, 2018, **20**, 28786.

Chapter 5: Ligand Effects on Electronic Structure and Reactivity of Transition metal Oxide Dications

Transition metal oxides in both the molecular and crystalline forms have been widely studied as they find applications in industry. Bare (early) transition metal mono-oxides have been found in the observable regions of high temperature outer planetary atmospheres and to classify M supergiants, while metal oxide heterogeneous catalysts are promising candidates for a variety of industrial applications. [1–3] For example, platinum oxide was found to be a good catalyst for direct low temperature methane conversion to methanol derivatives.[4,5] From the molecular viewpoint, transition metal oxides have been used for the reactions with several molecules such as alkanes, nitrile compounds, and aromatics, due to their unique catalytic ability.[6,7] The present computational work focuses on their significant role in the search for cleaner energy solution, such as a better method for methane to methanol conversion. Earlier studies have investigated their electronic structure and reactivity with multireference, density functional theory (DFT), and machine learning methods.[5,8,9] Transition metal oxides seem promising as potential catalysts for this process, if certain issues can be overcome. One significant problem, presented by Ravi *et al.* in 2017 and Latimer *et al.* in 2018, is product reactivity where methanol will continue to react, therefore both a method and suitable catalyst need to be found to allow for efficient reactivity with a mechanism that can be selective for the activated CH bond. [5,10,11] This presents a potential problem because the C-H bond of methanol is highly reactive, so a proper catalyst and reaction are necessary to carry out the CH bond activation of methane and not that of methanol.[8] No industrially viable solution has been identified up to date.[12]

Transition metal oxide dications may be suitable catalysts for these processes. Nature chooses dications for several natural and biological processes such as the heme iron complexes

in blood and are found in enzymes for their ability to switch between the two forms of the metal oxide.[13–18] These dications have important industrial applications, such as the presence in chemical oxidation processes as a chemical intermediate.[15,18] Dicationic transition metal oxides can take on two forms; oxo and oxyl. The oxo form is characterized by a closed shell oxygen side, and the oxyl form has significant electronic spin density on oxygen.[19] Each form follows a different mechanism. The oxo form will follow either the 2+2 mechanism or the proton coupled electron transfer (PCET) mechanism.[20] Both of these mechanisms can be selective but usually possess high energy barriers that the reaction must overcome. The oxyl form utilizes the radical mechanism, otherwise known as hydrogen atom transfer (HAT). The HAT mechanism is not selective but is characterized by having low energy barriers.

Our group has done extensive analysis on transition metal oxide cation, neutral, and anions to understand their electronic structure and potential reactivity.[21–31] The metal anions were shown to interact weakly with the produced methanol which allows for its quick removal from the catalytic cycle to avoid overoxidation and experimental work has shown single transition metal anions have the capability to activate the C-H bond of methane.[21,31] Investigations into transition metal oxide dications have been ongoing for both first and second row transition metal oxides to categorize metals as oxo or oxyl based on their electronic structure as well as investigations into their potential catalytic activity for water and methane activation.[20,29,32–35]

The effect of different ligands on transition metal oxide dications to stabilize the oxo or oxyl character has begun to be investigated in the literature.[35,36] In a study of FeO^{2+} by Kirkland *et al.* in 2018 it was shown that a strong field ligand, ammonia, can stabilize a higher energy oxo state to the ground state of the system.[35] Yang et. al discusses a study of multiple $(H_2O)_6MO^{n+}$ complexes to resemble hematite, and of the dications mentioned (V-Cu) all had a higher spin

ground state as a result of ligand attachment indicated a possible correlation between ligand effects and metal oxide stabilization.[36] It is expected that the 2+2 and PCET mechanisms to be favored with a strong field ligand such as ammonia, similar to what is shown in the FeO^{2+} study. For radical mechanisms, an electron withdrawing ligand such as halogens is expected to stabilize the system as was the case for ZrO.[26]

Many DFT studies have been done concerning the quantification of the oxophilicity, ability to form a metal oxygen bond, for transition metal oxides.[37–39] Work has also been done at the DFT level, and using machine learning methods, to try and characterize proper functionals to give a reliable description of the ground state for neutral transition metal oxides.[40,41] Several multirefrence studies have been carried out on neutral and singly charged transition metal oxides, however few exist for the dication systems.[36,42–45]

Here we present a more systematic work on transition metal dications by adding a single ammonia ligand to the metal and monitor the changes in the electronic structure of the metal oxygen unit and in the potential energy curves. To further investigate the ligand effect and higher symmetry, the first coordination sphere is saturated, with the addition of five ammonias, and again monitor the electronic structure of the metal oxygen unit.

1. Computational details

The geometry of the ground state for each $(NH_3)MO^{2+}$ was optimized at the DFT/MN15 level of theory with the cc-pVTZ(N,H,M)/aug-cc-pVTZ(O) basis sets.[23,46–48] The MN15 functional was used for this process as it is designed for characterizing transition metals, and the aug-cc-pVTZ basis set used on the oxygen to account for the polarized character of the metal oxygen bond. Using this geometry, the potential energy curves as a function of the metal-oxygen

distance are made at through multi-reference techniques CASSCF and MRCI. The active space of the reference CASSCF calculation consists of the three 2p orbitals of oxygen, and the five 3d and one 4s orbitals of the metal resulting in a nine orbital active space. Electronic configurations gathered at distances of interest (minima, shoulders) for the ground and several low-lying excited states. These calculations were completed using the Gaussian 16 and MOLPRO 2021 software packages. [49,50]

For the $(NH_3)_5MO^{2+}$ coordination complexes, calculations were carried out using Gaussian 16 software and the MN15 functional to first optimize the geometries ensuring only real frequencies were returned from harmonic frequency calculations. The same triple-ζ basis was used here, and natural orbitals are analyzed at the same level of theory to describe the chemical bonding in the complexes.

To investigate the reaction of these clusters with methane and methanol, the relative encounter complexes $[(NH_3)_5MO^{2+}(CH_4)]$, and transition states are obtained. The latter returned only one imaginary frequency from harmonic frequency calculations. These optimizations were completed using the same MN15/triple-ζ methodology.

Calculations were completed by completing IRC calculations in the forward a reverse direction starting at the optimized ground state 1et transition state geometry for the complex. Once the IRC calculations were complete several points along the IRC were chosen to describe the reaction and to pull the geometries to run single point energies to construct the potential energy curves.

Single point energies were calculated at CASSCF using a cc-pVDZ basis set on Ti, N, and H, and an aug-cc-pVDZ basis set on O and C, with a 12 orbital active space, consisting of the σ_{M-O}, two π_{M-O}, δ_M, two $\pi_{M-O}*$, $\sigma*_{M-O}$, $\delta*_M$, the σ and $\sigma*$ of the activated CH bond, and two

additional orbitals to allow for proper convergence (usually outer p orbitals). These calculations

were run as state averaged calculations for four singlet and three triplet states.

2. Structure and Orbitals

Equilibrium geometries for the ground states gathered from DFT calculations are shown

in Figure 5.1. The ammonia ligand binds to the metal oxygen unit on the metal side at an angle

ranging from 100-140° where iron is responsible for the smallest bond angle, and cobalt the

largest.

$(H_3N)TiO^{2+}$ $(H_3N)VO^{2+}$ $(H_3N)CrO^{2+}$ $(H_3N)MnO^{2+}$
(S=0)   (S=1/2)   (S=1)   (S=3/2)

$(H_3N)FeO^{2+}$ $(H_3N)CoO^{2+}$ $(H_3N)NiO^{2+}$ $(H_3N)CuO^{2+}$
(S=3)   (S=5/2)   (S=0)   (S=3/2)
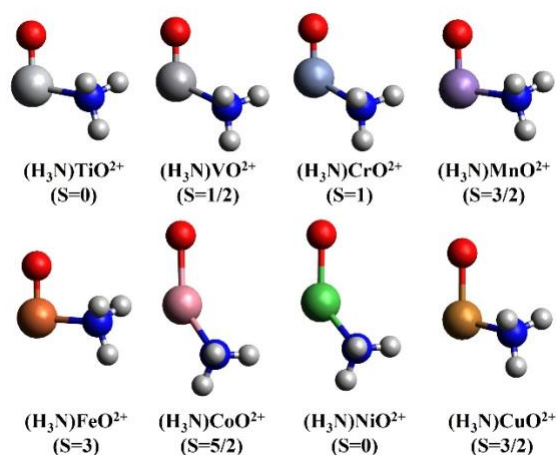
Figure 5.1 *Optimized equilibrium geometries for $(NH_3)MO^{2+}$ species*

This structure was implemented throughout the entire mono-ligand analysis. C_s symmetry is

imposed in these complexes and this reduced symmetry has an effect on the shape of the orbitals

in the active space as well as the states in the potential energy curves.

The active space remains composed of nine orbitals (see comp details section) however

the shape of the orbitals are different compared to the MO^{2+} complexes discussed in Chapter 4.

The active orbitals are shown in Figure 5.2 for chromium and nickel, to represent the distinct

change from early and late transition metals. Due to the lower symmetry, the σ and one of the π

orbitals of the MO bond belong to the same (a′) irreducible representation, allowing the orbitals

to mix, which results in the 1a′ and 2a′ orbitals of $(NH_3)CrO^{2+}$. However, this is not the case for the $(NH_3)NiO^{2+}$ complex, as these are denoted as σ_{MO}, π_{MO}, $\sigma_{MO}*$, $\pi_{MO}*$, and δ_M. An important note regarding the 6a′/virt orbital which is included to account for the 4s orbital of the metal, and remains minimally occupied in all cases, but was necessary for proper characterization of complexes.
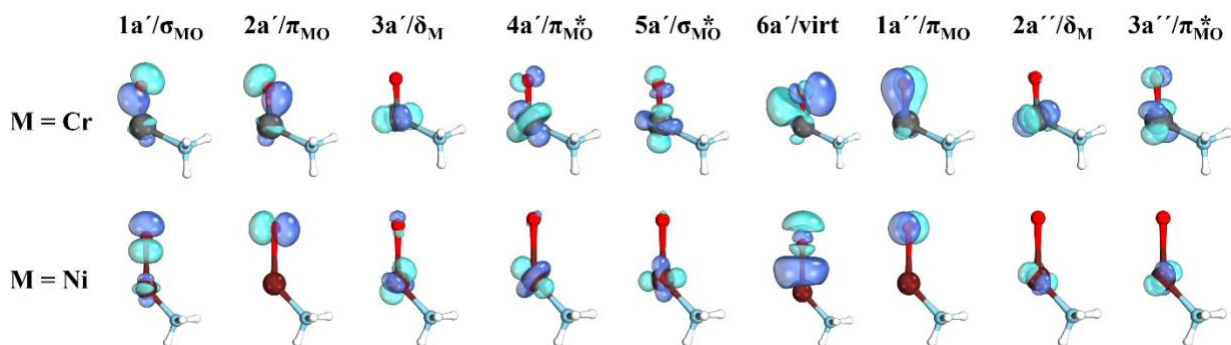
Figure 5.2: Active Orbitals for $(NH_3)MO^{2+}$ species (M=Cr, Ni)

3. Potential Energy Curves: Ligand influence on energetic gaps

Potential Energy curves were constructed for the $(NH_3)MO^{2+}$ complexes using the equilibrium geometries from the previous section and varying the metal oxygen bond length. The shift to C_s symmetry causes a split in states from the MO^{2+} states.

Addition of a strong field ligand would cause a stabilization of oxo states over oxyl states. For the TiO^{2+} there is a 50-60kcal/mol separation between oxo ground state and the oxyl states, and the same is observed previously for the VO^{2+} and the curves for the $(NH_3)TiO^{2+}$ and the $(NH_3)VO^{2+}$ complexes show a 60-70 kcal/mol separation of the oxo ground state to oxyl excited states. In the case of CrO^{2+} the oxyl quintet states were in a range of 50-60 kcal/mol above the oxo ground state, but in the $(NH_3)CrO^{2+}$ complex this gap become ~70 kcal/mol. The effects of the strong filed ligand on the metal oxide dication are more pronounced in the middle and late transition metals.

The $^4\Pi$ oxo state of MnO^{2+} is more than 20 kcal/mol higher than the $^{4,6,8}\Sigma^-$ cluster of oxyl states (see Fig. 1 of ref.[32]), but creates the local and global minima of the lowest energy $^4A''$ and $^4A'$ PECs, respectively, of Figure 5.3. These are less than 13 kcal/mol higher than the global minimum of oxyl character of the ground $^4A''$ state. The case of iron is even more interesting since the $^5\Sigma^+$ oxo state of FeO^{2+} is 13 kcal/mol higher than the $^3\Delta$ ground oxyl state and becomes the ground $^5A'$ state of $(NH_3)FeO^{2+}$ separated by 4 kcal/mol from the first oxyl $^7A'$ state (pertaining to the $^7\Delta$ state of FeO^{2+}; see Fig. 1 of ref. [32,35]). This stabilization of the oxo state has been observed in the literature for the $(NH_3)FeO^{2+}/ FeO^{2+}$ pair, [32,35] but the present PECs are more complete as they include more states, such as the aforementioned $^7A'$ state. Finally, in some of the PECs of $(NH_3)CoO^{2+}$ ($^4A'$ and $^4A''$) we see the appearance of local minima and shoulders at 1.6-1.7 Å and 20-23 kcal/mol, which are of oxo character. These were not present in the CoO^{2+} and are expected to stabilize even further when more ammonia ligands are coordinated to cobalt. The CASSCF PECs for $(NH_3)CoO^{2+}$ show these shoulders at energies of about 40 kcal/mol. Such shoulders are not present at the CASSCF PECs for $(NH_3)NiO^{2+}$ and $(NH_3)CuO^{2+}$ with the 60 kcal/mol range, and oxo minima are not expected to play an important role.
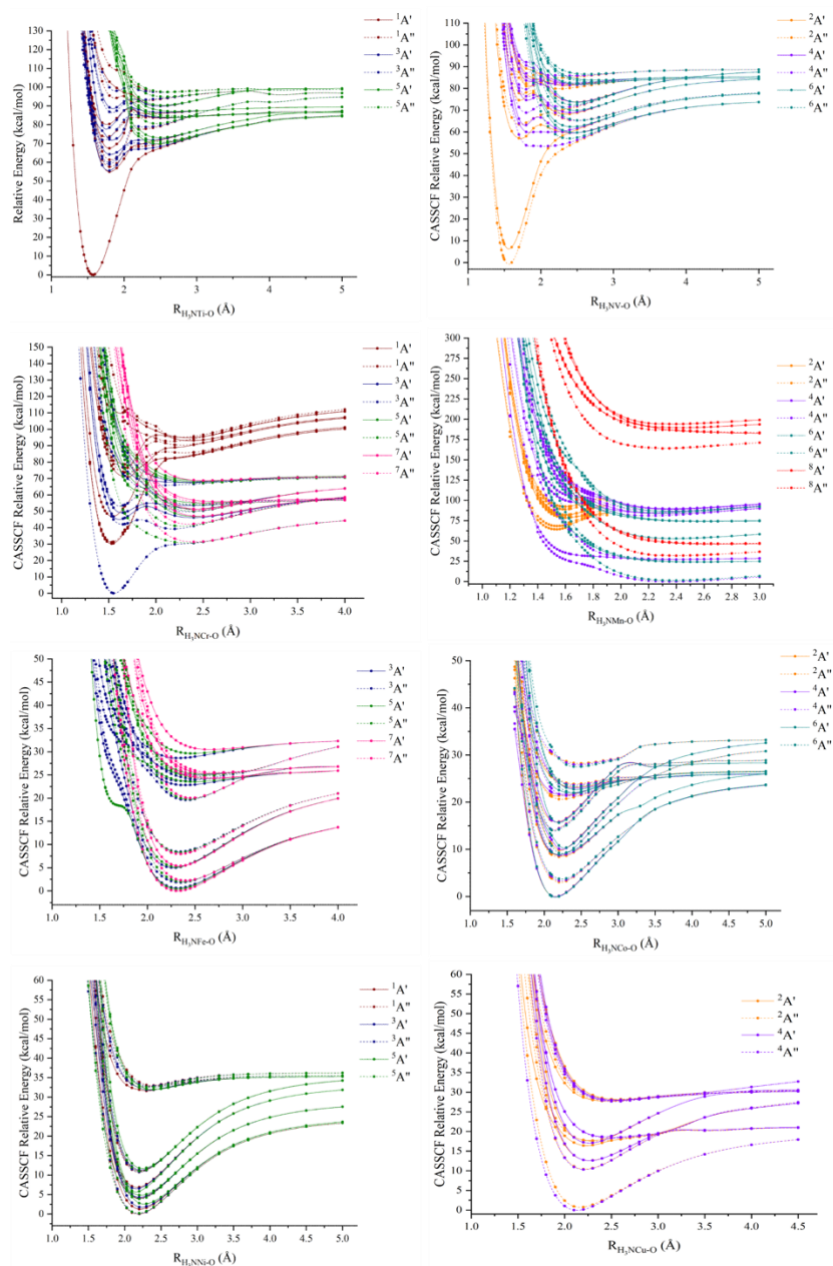
Figure 5.3: *CASSCF Potential energy curves of $(NH_3)MO^{2+}$*

4. Influence of a Fully Coordinated System on Oxo Oxyl Character

To understand how to further stabilize the oxo states in the ligated complexes, the fully coordinated metal oxide dications were explored. $(NH_3)_5MO^{2+}$ complexes were optimized at DFT using MN15 for all metals and spins explored in previous sections. Table 5.1 displays the

energies, metal oxygen bond distance, electron configurations based on a natural orbital analysis, and the spin density for each complex to understand the trends in oxo and oxyl species for the fully coordinated units.

Table 5.1. *Metal-oxygen bond length (r_{MO} in Å), relative energies (ΔE in cm^{-1}), electronic configurations (see Figure 5.4 for orbitals), and Mulliken spin density on the oxygen atom (ρ_S/O) for the lowest energy spin states of $(NH_3)_5MO^{2+}$ species, M = Ti-Cu, at the MN15 level of theory.*

Species	S	r_{MO}	ΔE	σ_{MO}	π_{MO}	π_{MO}	δ_M	π^*_{MO}	π^*_{MO}	δ^*_M	σ^*_{MO}	ρ_S/O
$(NH_3)_5TiO^{2+}$	0	1.579	0.0	2	2	2						0.00
	1	1.841	19496	2	2	α	α					0.95
$(NH_3)_5VO^{2+}$	1/2	1.547	0.0	2	2	2	α					0.18
	3/2	1.832	18959	2	2	α	α	α				0.96
$(NH_3)_5CrO^{2+}$	0	1.520	0.0	2	2	2	2					0.00
	1	1.613	627	2	2	2	α	α				0.38
	2	1.875	7056	2	2	α	α	α	α			0.99
$(NH_3)_5MnO^{2+}$	1/2	1.558	1470	2	2	2	2	α				0.06
	3/2	1.620	0.0	2	2	2	α	α	α			0.62
	5/2	1.810	4750	2	2	α	α	α	α	α		0.96
$(NH_3)_5FeO^{2+}$	0 [a]	1.603	2645	2	2	2	2	α	β			0.00
	1	1.602	0.0	2	2	2	2	α	α			0.84
	2	1.594	380	2	2	2	α	α	α	α		0.81
	3	1.878	8166	2	2	α	α	α	α	α	α	1.45
$(NH_3)_5CoO^{2+}$	1/2	1.768	0.0	2	2	2	2	2	α			1.01
	3/2	1.643	1587	2	2	2	2	α	α	α		1.18
	5/2	1.756	7936	2	2	2	α	α	α	α	α	1.64
$(NH_3)_5NiO^{2+}$	0 [a]	1.759	338	2	2	2	2	2	α	β		1.14
	1	1.761	0.0	2	2	2	2	2	α	α		1.13
	2	1.777	3217	2	2	2	2	α	α	α	α	1.77
$(NH_3)_5CuO^{2+}$	1/2	1.844	149	2	2	2	2	2	α	2		
	3/2	2.546	0.0	2	2	2	2	2	α	α	α	1.94

[a] The spin contamination for these two open-shell singlets is 0.66 and 0.39 for $(NH_3)_5FeO^{2+}$ and $(NH_3)_5NiO^{2+}$, respectively.
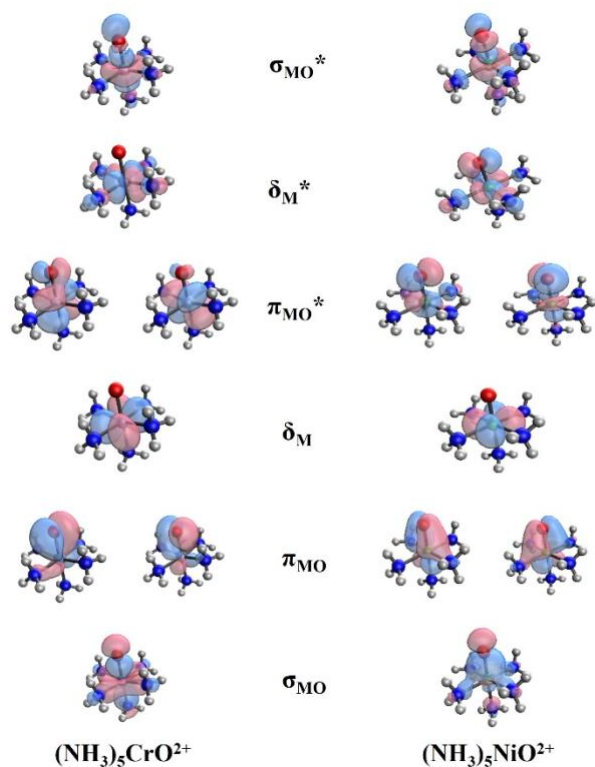
Figure 5.4. *Frontier orbitals for (NH$_3$)$_5$CrO^{2+} and (NH$_3$)$_5$NiO^{2+}*

The electronic structure of (NH$_3$)$_5$TiO^{2+} and (NH$_3$)$_5$VO^{2+} closely resembles that of the plain or mono-ligated metal oxide dications. The ground states retain their $\sigma_{MO}^2\pi_{MO}^4$ and $\sigma_{MO}^2\pi_{MO}^4\delta_M^1$ oxo character being 50-60 kcal/mol (~19,000 cm^{-1}) away from the oxyl states created from the promotion of electron(s) to the δ_M for the singlet/doublet and δ_M and π_{MO}^* for the triplet and quartet.

The electronic structure of the (NH$_3$)$_5$CrO^{2+} lowest energy states is affected by the destabilization of δ_M^*. The ground state ($^3\Sigma^-$) of CrO^{2+} has a $\sigma_{MO}^2\pi_{MO}^4\delta_M^1\delta_M^{*1}$ configuration, but the lowest energy triplet of (NH$_3$)$_5$CrO^{2+} replaces the δ_M^* with the lower energy π_{MO}^* orbital, which is still highly localized on Cr (see Figure 5.4). [32] However, the introduced anti-bonding orbital pushes the triplet state of (NH$_3$)$_5$CrO^{2+} higher in energy than the singlet state, which was an excited state for CrO^{2+} with more than 30 kcal/mol excitation energy. CrO^{2+} had two low-lying singlet states ($^1\Gamma$, $^1\Sigma^+$) made of all three $\sigma_{MO}^2\pi_{MO}^4(\delta_M\delta_M^*)^2$ configurations.[32] Only

the $\sigma_{MO}^2\pi_{MO}^4\delta_M^2$ configuration survives (no population of anti-bonding orbitals) and is the dominant configuration for the ground singlet state. The singlet and triplet states of $(NH_3)_5CrO^{2+}$ are within 2 kcal/mol (627 cm^{-1}) and can be both categorized as oxo states with bond lengths of 1.520 and 1.613 Å respectively. On the other hand, the quintet state of $(NH_3)_5CrO^{2+}$ has a bond length of 1.875 Å and a configuration $\sigma_{MO}^2\pi_{MO}^3\delta_M^1\pi_{MO}^{*2}$, which makes it an oxyl state, and is higher than the ground state by 7056 cm^{-1} (~20 kcal/mol).

The electronic structure changes dramatically for manganese as well. The $(NH_3)_5MnO^{2+}$ complex has oxo ground states as opposed to MnO^{2+} and $(NH_3)MnO^{2+}$, which have oxyl ground states and low-lying oxo states. The lowest doublet and quartet states of $(NH_3)_5MnO^{2+}$ have $\sigma_{MO}^2\pi_{MO}^3\delta_M^2\pi_{MO}^{*1}$ and $\sigma_{MO}^2\pi_{MO}^4\delta_M^1\pi_{MO}^{*2}$ configurations, respectively, with bond lengths 1.558 and 1.620 Å. The quartet state is the ground state separated from the doublet state by 1470 cm^{-1}. The sextet oxyl state is 4750 cm^{-1} higher with a bond length of 1.810 Å and a $\sigma_{MO}^2\pi_{MO}^3\delta_M^1\pi_{MO}^{*2}\delta_M^{*1}$ configuration. Overall, the oxo and oxyl states remain competitive but the oxo states are more stable in the $(NH_3)_5MnO^{2+}$ complex.

The oxo states for iron are also stabilized further going from $(NH_3)FeO^{2+}$ to $(NH_3)_5FeO^{2+}$. The $^5A'$ state of $(NH_3)FeO^{2+}$ with a $1a'^2 2a'^2 1a''^2 3a'^1 2a''^1 4a'^1 3a''^1$ (see Figure 5.2) ~ $\sigma_{MO}^2\pi_{MO}^4\delta_M^1\pi_{MO}^{*2}\delta_M^{*1}$ configuration (see Figure 5.4) remains among the lowest energy states, but two other states, a singlet and a triplet, where the two $\delta_M^1\delta_M^{*1}$ electrons couple together in the δ_M orbital. The two π_{MO}^{*2} electrons couple into an open-shell singlet or a triplet spin state. All three states are within 8 kcal/mol and they have very similar r_{MO} values (1.60 ± 0.01 Å). The open-shell singlet state has considerable spin contamination, and a more accurate description of the wavefunction would require multi-reference methods. The septet state is the lowest energy oxyl state, with a $\sigma_{MO}^2\pi_{MO}^3\delta_M^1\pi_{MO}^{*2}\delta_M^{*1}\sigma_{MO}^{*1}$ configuration.

The lowest energy state of $(NH_3)_5CoO^{2+}$ is a doublet with a bond length of 1.768 Å. This length lies in between the bond lengths encountered so far for oxo (~1.6 Å) and oxyl (>1.8 Å) states. Its configuration is $\sigma_{MO}^2\pi_{MO}^4\delta_M^2\pi_{MO}^{*3}$ but now the π_{MO}^* orbital has larger contribution from the *2p* of oxygen similarly to the $(NH_3)_5NiO^{2+}$ orbitals of Figure 5.4. Therefore, this is the first oxyl state not corresponding to a half-filled π_{MO} orbital but has considerable Mulliken spin density on oxygen (1.0 electron). All of the π_{MO}^3 states mentioned above have a spin density of 0.95 (except the S=3 of iron having 1.45) on oxygen. In the quartet state, one electron moves from π_{MO}^* to δ_M^*, which leads to contraction of the MO bond to 1.643 Å, and corresponds to the configuration of the shoulders observed in the PECs of $(NH_3)CoO^{2+}$ at around 20-25 kcal/mol (see above). Finally, the sextet state follows at 7936 cm^{-1} and populates σ_{MO}^* (spin density of 1.6).

Finally, all studied states of the last two oxides, $(NH_3)_5NiO^{2+}$ and $(NH_3)_5CuO^{2+}$, have long bond lengths (>1.75 Å) and their configurations all have $\sigma_{MO}^2\pi_{MO}^4\delta_M^2$ in common. The remaining electrons populate the π_{MO}^* and δ_M^* orbitals, and only for the highest spin states the σ_{MO}^* is populated. The metal-oxygen bond in the quartet state of $(NH_3)_5CuO^{2+}$ is clearly ruptured and better described as $(NH_3)_5Cu^{2+}+O(^3P)$. In all of these states the spin density on oxygen is between 1.1 and 1.8; the spin density for S=3/2 of $(NH_3)_5CuO^{2+}$ is 1.94.

Chapter 4 involved a discussion on metal oxygen bond length trends for oxo and oxyl components and whether or not a generalization can be made concerning this information. In fact, one can connect the bond lengths to the spin density in terms of oxo and oxyl. A metal-oxygen bond length of ~1.6 Å is the interchange point for metal oxide character. For species with a M-O bond length less than 1.6 Å the spin density is in turn less than 1.0, and though the occupation of π_{MO}^* orbitals is observed, this is localized more so on the metal as opposed to the

oxygen. For those species with a bond length greater than 1.6Å in the metal oxygen unit, the spin density is greater than 1.0 and predominantly oxyl, with unpaired electrons occupying the π_{MO} orbitals which are located on oxygen.

5. Effects of Hydrogen Bonding in Activation Energies

For the formation of methanol from methane, the transfer of a hydrogen atom from CH_4 to CH_3OH is involved via either the HAT or PCET mechanism with the eventual release of CH_3 or CH_2OH radical as a product. Ideally the reaction involving CH_4 would proceed slower to avoid the over oxidation of CH_3OH to unwanted side products and to increase the yield of CH_3OH. However, due to the strength of the CH bond in methane, the methanol is at an immediate disadvantage and makes the search for an ideal selective catalyst even more difficult

Upon investigation into the reaction of $(NH_3)_5VO^{2+} + CH_4$ and subsequent methanol analysis, hydrogen bonding between the OH group and the ammonia ligands was observed and could potentially affect the activation energies of the methane and methanol species, if this is the case could present a new avenue to pursue the investigation into an ideal catalyst.

Analysis of methane and methanol activation energies began with the optimization of the reactants (R), transition states (TS), and products (P) of the $(NH_3)_5VO^{2+} + CH_4$ reaction and the partial optimization of the $(NH_3)_5VO^{2+} + CH_3OH$ reaction, the structures for which are displayed in Figure 5.5.
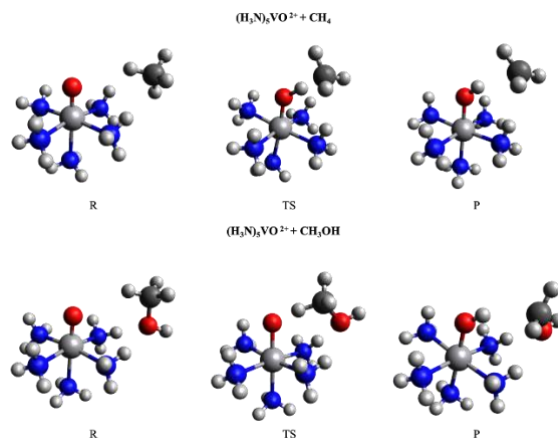
Figure 5.5. *Structures for the reactants (R), transition states (TS), and products (P) of the reaction between (NH₃)₅VO²⁺ (S=1/2) and CH₄ (a) or CH₃OH (b). The structures in (c) correspond to partially optimized (PO) species for the reaction with CH₃OH, where the OH group points away from the ammonia ligands (see text for more details).*

The methanol pathway is partially optimized (PO) by using the optimized structure of the methane species and replacing the hydrogen on methane furthest away from the catalyst with OH to form methanol, and only the OH group of methanol is optimized.

With the optimization of each stage of the reaction for each metal, the activation energies for the methane and methanol pathways could be calculated and compared to understand any potential influence of hydrogen bonding. The calculated activation energies are shown in Figure 5.6 where the methane energies are depicted as circles, methanol as diamonds, and the color denoting low spin (LS), intermediate spin (IS), high spin (HS), or the S=3 of iron.
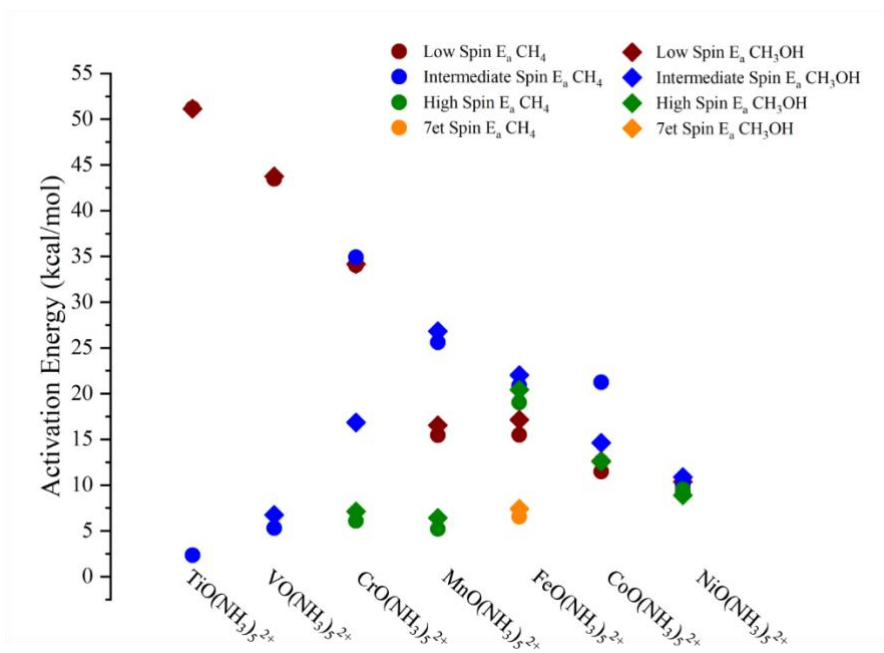
Figure 5.6. *Activation energies for the reactions of $(NH_3)_5MO^{2+}$ with CH_4 and CH_3OH for M=Ti-Ni and for LS, IS, and HS spin states.*

In all cases E_a values are competitive (within 1.6 kcal/mol) for methane and methanol, and in nearly all cases the E_a value for methanol is slightly larger. These results are in complete contrast with the literature reports. For example, Norskøv and co-workers found that the E_a values for methanol are always 0.57 eV (13.1 kcal/mol) lower than methane for a large number/variety of heterogeneous catalysts.[10] Similar differences can be implied for molecular catalysts based on the selectivity plots Ravi *et. al*.[11] Our results confirm that hydrogen bonding can be a future very promising strategy that needs to be explored further.

The largest activation barriers correspond to states that have characterized as oxo states. For example, the LS of $(NH_3)_5TiO^{2+}$ and $(NH_3)_5VO^{2+}$, LS/IS for $(NH_3)_5CrO^{2+}$ and $(NH_3)_5MnO^{2+}$, LS/IS/HS(S=2) for $(NH_3)_5FeO^{2+}$, and maybe IS for $(NH_3)_5CoO^{2+}$. Interestingly, the E_a values for these states decrease in a linear fashion going from early to late transition metals, which indicates that the radical character of the oxo states increases. This is also confirmed by the Mulliken spin

densities on oxygen for these states: 0.00 (Ti/LS), 0.18 (V/LS), 0.00 (Cr/LS), 0.38 (Cr/IS), 0.06 (Mn/LS), 0.62 (Mn/IS), 0.00 (Fe/LS), 0.84 (Fe/IS), 0.81 (Fe/HS), 1.18 (Co/IS). The Fe/LS state is the open-shell singlet sister state of Fe/IS and thus the spin density is 0.00 due to cancelation of the two π_{MO}^* electron spins. Therefore, a fairer picture could be to use the spin density for the direction along which the C−H bond of CH_4 or CH_3OH approaches. Due to symmetry these values are half of the previous values and is 0.41 for Fe/LS. The resulting values (averaged over the various spins) also show a linear trend 0.00, 0.18, 0.19, 0.34, 0.41, and 0.59 for Ti, V, Cr, Mn, Fe, and Co, respectively.

A different explanation can be provided based on the potential energy curves of ref.[12] along the reaction coordinate of $(NH_3)_5TiO^{2+} + CH_4$. According to Figure 5.7 and corresponding discussion of this work, the activation barrier of the ground oxo state (Ti/LS/S=0) is controlled by the excitation energy to the oxyl state (Ti/HS/S=1). The lower the excitation energy, the lower the E_a value is expected to be. Indeed, the oxo → oxyl energy difference drops as we go from Ti to Mn (19496, 18959, 7056, and 4750 cm^{-1}; see Table 5.1) but increases for Fe (8166 cm^{-1}). Overall, the combination of the spin density on the oxygen atom and oxo → oxyl excitation energies can be considered as good descriptors for predicting the activation barriers of the reaction of metal oxides with methane.

On the other hand, the E_a values for the remaining states of clear oxyl character are very small (of the order of 10 kcal/mol or smaller) and present a rather increasing trend. The two lines converge to the same values for $(NH_3)_5NiO^{2+}$.

6. Importance of Excited States in Reactions

When investigating the clusters the $TiO(NH_3)_5$ with methane it was noticed that in order to fully understand the mechanism of this system , the excited states would need to be further investigated. Using the single points along the intrinsic reaction coordinate constructed a reaction pathway for the reaction of TiO5A with CH_4. Multireference calculations were completed with state averaged CASSCF involving a 12 orbital active space consisting of the σ_{M-O}, two π_{M-O}, δ_M, two $\pi_{M-O}*$, $\sigma*_{M-O}$, $\delta*_M$, the σ and $\sigma*$ of the activated CH bond, and two additional orbitals to allow for proper convergence (usually outer p orbitals). Due to the complexity of the calculations the calculations were completed using a lower basis set: cc-pVDZ on the metal, nitrogen, and hydrogen; and aug-cc-pVDZ on the oxygen and carbon, using the MOLPRO 2021 suite of software.[50]

It was originally believed that the ground state singlet proceeds through a proton coupled electron transfer mechanism (PCET). The PCET for this singlet would involve the oxygen taking the proton and the electron going to the metal breaking the CH_3-H bond. However, concerning the product with the OH group, this had 2 unpaired electrons, which could produce either a singlet or a triplet depending on the spin of the unpaired electrons on the metal and the methyl radical. To investigate the effect of the triplet pathway on the ground state singlet pathway we constructed potential energy curves for several states, focusing on the ground state singlet, a higher energy singlet, and the lowest energy triplet. The potential energy curves for the system are shown in Figure 5.7. The states shown in red are the singlet and green is the triplet, and a 2+ charge is retained by the catalyst throughout the reaction.
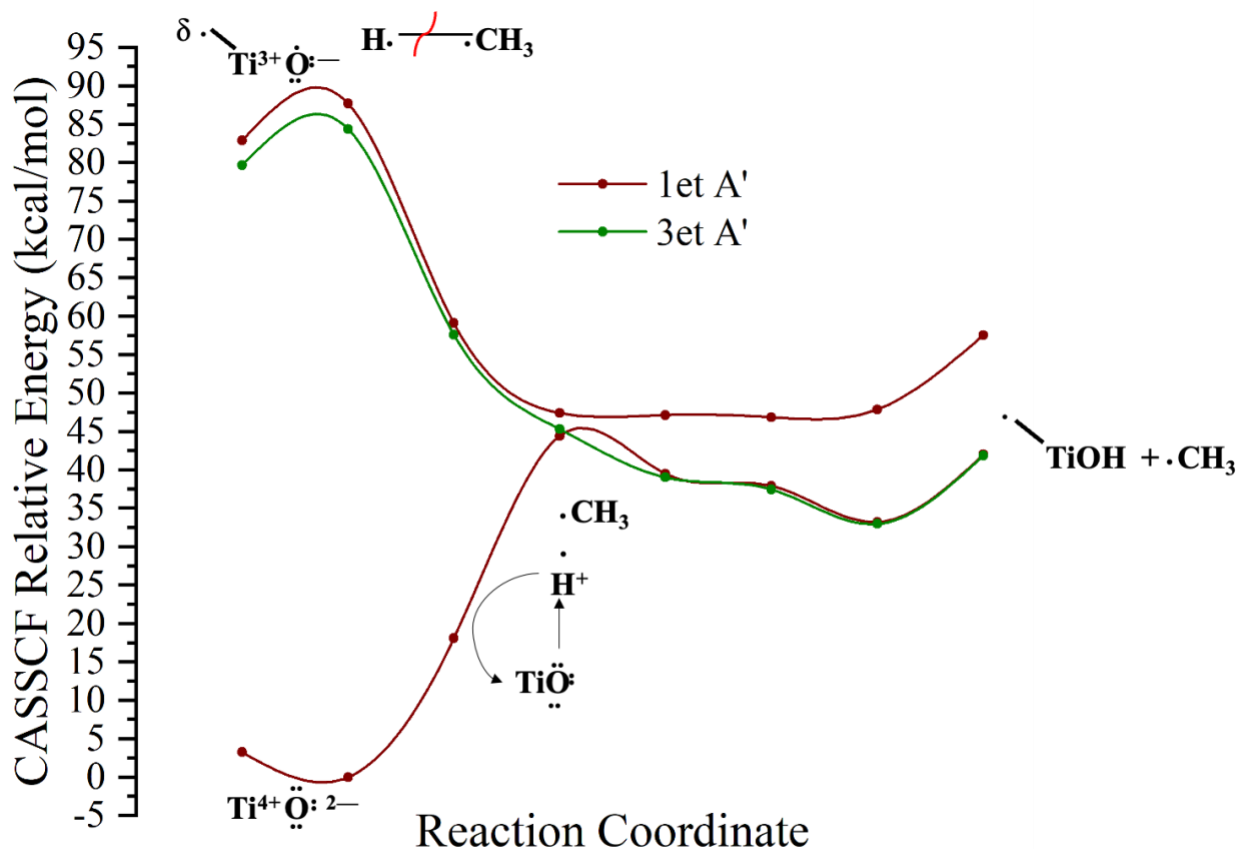
Figure 5.7: *potential energy curves for the $(NH_3)_5TiO^{2+}$ +CH_4 reaction to form a cluster with an OH group and a methyl group*

The lowest singlet begins as a closed shell $Ti^{4+}O^{2-}$ cluster reacting with closed shell CH_4 which is expected to result in a repulsive curve, the oxygen grabs the H and one of the electrons in the CH_3-H bond moves to the metal, the resulting product is the TiOH cluster with an electron on the metal and the methyl radical. The triplet product is the same but with a different configuration resulting from a spin flip. The higher energy singlet also plays an effect as it begins with an open shell singlet metal oxide cluster and undergoes the Hydrogen Atom transfer (HAT) mechanism when reacting with closed shell methane, this is expected to be an attractive process. However, when the two singlets interact with each other there is an avoided crossing

since the same spin cannot cross which does not result in a repulsive and attractive curve for the singlet states but instead they divert away from each other. This behavior yields the ground state singlet curve with the same product as the triplet and the higher energy singlet state will not stabilize, instead end in a high energy product. With this in mind we can confidently say that the ground state singlet does not undergo the PCET mechanism due to the effect of the behavior of the higher energy singlet, without which the ground state singlet would have ended high in energy with a repulsive curve, rather what the ground state singlet is undergoing is more of the hydrogen atom transfer mechanism and the PCET implies an excited state undergoing the HAT mechanism. Essentially, the PCET provides an explanation for the behavior of the ground state singlet on its own and neglecting its interaction with excited states.

1   A. J. Merer, SPECTROSCOPY OF THE DIATOMIC 3d TRANSITION METAL OXIDES, *Annu. Rev. Phys. Chem*, 1989, **40**, 407–445.

2   E. Sedaghati, H. M. J. Boffin, R. J. MacDonald, S. Gandhi, N. Madhusudhan, N. P. Gibson, M. Oshagh, A. Claret and H. Rauer, Detection of titanium oxide in the atmosphere of a hot Jupiter, *Nature*, 2017, **549**, 238–241.

3   N. M. White Lowell Observatory and R. F. Wing, PHOTOELECTRIC TWO-DIMENSIONAL SPECTRAL CLASSIFICATION OF M SUPERGIANTS, *Astrophys J*, 1978, **222**, 209–219.

4   K. A. Jørgensen, Transition-Metal-Catalyzed Epoxidations, *Chem Rev*, 1989, **89**, 431–458.

5   R. A. Periana, D. J. Taube, S. Gamble, H. Taube, T. Satoh and Fujii Hiroshi, Platinum Catalysts for the High-Yield Oxidation of Methane to Methanol Derivative, *Science (1979)*, 1988, **280**, 560–564.

6   K. Eller and H. Schwarz, Organometallic Chemistry in the Gas Phase, *Chem. Rev.*, 1991, **91**, 1121–1177.

7   J. Xu, M. T. Rodgers, J. B. Griffin and P. B. Armentrouf, Guided ion beam studies of the reactions of V+n (n=2-17) with O2: Bond energies and dissociation pathways, *Journal of Chemical Physics*, 1998, **108**, 9339–9350.

8   C. A. Gaggioli, J. Sauer and L. Gagliardi, Hydrogen Atom or Proton Coupled Electron Transfer? C-H Bond Activation by Transition-Metal Oxides, *J Am Chem Soc*, 2019, **141**, 14603–14611.

9   A. Nandy, C. Duan, C. Goffinet and H. J. Kulik, New Strategies for Direct Methane-to-Methanol Conversion from Active Learning Exploration of 16 Million Catalysts, *J Am Chem Soc*, 2022, **2**, 1200–1213.

10   A. A. Latimer, A. Kakekhani, A. R. Kulkarni and J. K. Nørskov, Direct Methane to Methanol: The Selectivity-Conversion Limit and Design Strategies, *ACS Catal*, 2018, **8**, 6894–6907.

11   M. Ravi, M. Ranocchiari and J. A. van Bokhoven, The Direct Catalytic Oxidation of Methane to Methanol - A Critical Assessment, *Angewandte Chemie*, 2017, **129**, 16684–16704.

12   E. E. Claveau, S. Sader, B. A. Jackson, S. N. Khan and E. Miliordos, Transition metal oxide complexes as molecular catalysts for selective methane to methanol transformation: Any prospects or time to retire?, *Physical Chemistry Chemical Physics*, 2023, **25**, 5313.

13   A. J. Mitchell, N. P. Dunham, R. J. Martinie, J. A. Bergman, C. J. Pollock, K. Hu, B. D. Allen, W. C. Chang, A. Silakov, J. M. Bollinger, C. Krebs and A. K. Boal, Visualizing the reaction cycle in an Iron(II)- and 2-(Oxo)-glutarate-dependent hydroxylase, *J Am Chem Soc*, 2017, **139**, 13830–13836.

14   R. J. Martinie, C. J. Pollock, M. L. Matthews, J. M. Bollinger, C. Krebs and A. Silakov, Vanadyl as a Stable Structural Mimic of Reactive Ferryl Intermediates in Mononuclear Nonheme-Iron Enzymes, *Inorg Chem*, 2017, **56**, 13382–13389.

15   J. Hohenberger, K. Ray and K. Meyer, The biology and chemistry of high-valent iron-oxo and iron-nitrido complexes, *Nat Commun*, 2012, **3**, 1–13.

16   T. L. Poulos, Heme enzyme structure and function, *Chem Rev*, 2014, **114**, 3919–3962.

17   A. H. Follmer, S. Tripathi and T. L. Poulos, Ligand and Redox Partner Binding Generates a New Conformational State in Cytochrome P450cam (CYP101A1), *J Am Chem Soc*, 2019, **141**, 2678–2683.

18   K. Ray, F. F. Pfaff, B. Wang and W. Nam, Status of reactive non-heme metal-oxygen intermediates in chemical and enzymatic reactions, *J Am Chem Soc*, 2014, **136**, 13942–13958.

19   Y. Shimoyama and T. Kojima, Metal-Oxyl Species and Their Possible Roles in Chemical Oxidations, *Inorg Chem*, 2019, **58**, 9517–9542.

20   S. N. Khan and E. Miliordos, Electronic Structure of RhO2+, Its Ammoniated Complexes (NH3)1-5RhO2+, and Mechanistic Exploration of CH4Activation by Them, *Inorg Chem*, 2021, **60**, 16111–16119.

21   G. Liu, Z. Zhu, S. M. Ciborowski, I. R. Ariyarathna, E. Miliordos and K. H. Bowen, Selective Activation of the C−H Bond in Methane by Single Platinum Atomic Anions, *Angewandte Chemie*, 2019, **131**, 7855–7859.

22   I. R. Ariyarathna, N. M. S. Almeida and E. Miliordos, Ab initio investigation of the ground and excited states of RuO+,0,-and their reaction with water, *Physical Chemistry Chemical Physics*, 2020, **22**, 16072.

23   S. N. Khan and E. Miliordos, Methane to Methanol Conversion Facilitated by Transition-Metal Methyl and Methoxy Units: The Cases of FeCH3+ and FeOCH3+, *Journal of Physical Chemistry A*, 2019, **123**, 5590–5599.

24   E. E. Claveau and E. Miliordos, Quantum chemical calculations on NbO and its reaction with methane: Ground and excited electronic states, *Physical Chemistry Chemical Physics*, 2019, **21**, 26324–26332.

25   N. M. S. Almeida, I. R. Ariyarathna and E. Miliordos, Ab initio calculations on the ground and excited electronic states of neutral and charged palladium monoxide, PdO0,+,-, *Physical Chemistry Chemical Physics*, 2018, **20**, 14578–14586.

26   B. A. Jackson and E. Miliordos, Weak-field ligands enable inert early transition metal oxides to convert methane to methanol: The case of ZrO, *Physical Chemistry Chemical Physics*, 2020, **22**, 6606–6618.

27   I. R. Ariyarathna and E. Miliordos, Ab initio investigation of the ground and excited states of ZrO + and NbO +, *J Quant Spectrosc Radiat Transf*, 2020, **255**, 107265.

28   I. R. Ariyarathna and E. Miliordos, Ab initio investigation of the ground and excited states of TcO+ and RhO+, *J Quant Spectrosc Radiat Transf*, 2022, **280**, 108074.

29   I. R. Ariyarathna and E. Miliordos, Ab initio investigation of the ground and excited states of MoO+,2+,- and their catalytic strength on water activation, *Physical Chemistry Chemical Physics*, 2018, **20**, 12278–12287.

30   I. R. Ariyarathna and E. Miliordos, Radical abstraction: Vs. oxidative addition mechanisms for the activation of the S - H, O - nd C - H bonds using early transition metal oxides, *Physical Chemistry Chemical Physics*, 2021, **23**, 1437–1442.

31   S. Sader and E. Miliordos, Methane to methanol conversion facilitated by anionic transition metal centers: The case of Fe, Ni, Pd, and Pt, *Journal of Physical Chemistry A*, 2021, **125**, 2364–2373.

32   E. E. Claveau and E. Miliordos, Electronic structure of the dicationic first row transition metal oxides, *Physical Chemistry Chemical Physics*, 2021, **23**, 21172–21182.

33   N. M. S. Almeida, I. R. Ariyarathna and E. Miliordos, O-H and C-H Bond Activations of Water and Methane by RuO2+ and (NH3)RuO2+: Ground and Excited States, *Journal of Physical Chemistry A*, 2019, **123**, 9336–9344.

34   S. N. Khan and E. Miliordos, Scandium in Neutral and Positively Charged Ammonia Complexes: Balancing between Sc2+and Sc3+, *Journal of Physical Chemistry A*, 2020, **124**, 4400–4412.

35   J. K. Kirkland, S. N. Khan, B. Casale, E. Miliordos and K. D. Vogiatzis, Ligand field effects on the ground and excited states of reactive FeO2+ species, *Physical Chemistry Chemical Physics*, 2018, **20**, 28786.

36   Y. Yang, M. A. Ratner and G. C. Schatz, Multireference Ab initio study of ligand field d-d transitions in octahedral transition-metal oxide clusters, *Journal of Physical Chemistry C*, 2014, **118**, 29196–29208.

37   K. P. Kepp, A quantitative scale of oxophilicity and thiophilicity, *Inorg Chem*, 2016, **55**, 9461–9470.

38   K. A. Moltved and K. P. Kepp, The chemical bond between transition metals and Oxygen: Electronegativity, d-Orbital Effects, and Oxophilicity as Descriptors of Metal-Oxygen Interactions, *Journal of Physical Chemistry C*, 2019, **123**, 18432–18444.

39   G. O. Kayode and M. M. Montemore, Factors controlling oxophilicity and carbophilicity of transition metals and main group metals, *J Mater Chem A Mater*, 2021, **9**, 22325–22333.

40   I. Østrøm, M. A. Hossain, P. A. Burr, J. N. Hart and B. Hoex, Designing 3d metal oxides: selecting optimal density functionals for strongly correlated materials, *Phys Chem Chem Phys*, 2022, **24**, 14119–14139.

41   H. J. Kulik, F. Liu and C. Duan, Rapid detection of strong correlation with machine learning for transition-metal complex high-throughput screening, *Journal of Physical Chemistry Letters*, 2020, **11**, 8067–8076.

42   T. Jiang, Y. Chen, N. A. Bogdanov, E. Wang, A. Alavi and J. Chen, A full configuration interaction quantum Monte Carlo study of ScO, TiO, and VO molecules, *Journal of Chemical Physics*, 2021, **154**, 164302.

43   Y. Nakao, K. Hirao and T. Taketsugu, Theoretical study of first-row transition metal oxide cations, *Journal of Chemical Physics*, 2001, **114**, 7935–7940.

44   E. Miliordos and A. Mavridis, Electronic structure and bonding of the early 3d-transition metal diatomic oxides and their ions: ScO0,±, TiO0,±, CrO0,±, and MnO0,±, *Journal of Physical Chemistry A*, 2010, **114**, 8536–8572.

45   M. R. A. Blomberg and P. E. M. Siegbahn, Theoretica Chimica Acta A comparison between multireference CI and effective medium theories for diatomic FeN, *Theor Chim Acta*, 1992, **81**, 365–374.

46   N. B. Balabanov and K. A. Peterson, Systematically convergent basis sets for transition metals. I. All-electron correlation consistent basis sets for the 3d elements Sc-Zn, *Journal of Chemical Physics*, 2005, **123**, 064107.

47   T. H. Dunning, Gaussian basis sets for use in correlated molecular calculations. I. The atoms boron through neon and hydrogen, *J Chem Phys*, 1989, **90**, 1007–1023.

48   D. E. Woon and T. H. Dunning, Gaussian basis sets for use in correlated molecular calculations. IV. Calculation of static electrical response properties, *J Chem Phys*, 1994, **100**, 2975–2988.

49   M. J. Frisch, G. W. Trucks, H. E. Schlegel, G. E. Scuseria, M. A. Robb, J. R. Cheeseman, G. Scalmani, V. Barone, G. A. Petersson, Farkas. O., J. B. Foresman and J. D. Fox, *Gaussian, Inc., Wallingford CT,* 2016.

50   H.-J. Werner and P. J. Knowles, MOLPRO, version 2015.1, a package of ab initio programs, *Chem. Phys. Letters*, , DOI:10.1063/1.448627.

Chapter 6: Effectiveness of DFT Functionals on Ground and Excited States of Penta-Ammonia Coordinated Transition Metal Oxide Dications Compared to Multireference Methods

Transition metal complexes, specifically transition metal oxides have been shown to be promising candidates for many industrial processes. Studies have shown their ability to act as suitable catalysts as well as present in several new industrial advancements such as solar cells and gas sensors.[1–10] Transition metal complexes are generally of multireference character and have complex electronic structure.[11–24] In principle, they should be studied with multireference techniques, however these techniques are expensive and these systems cannot be studied catalytically without the presence of one or two small ligands.[25]

Density functional theory (DFT) has revolutionized quantum chemistry by providing a sound basis for the development of new strategies to determine energetics, structures and properties of a multitude of compounds for much cheaper cost than other methodologies.[26] DFT is a less costly method than multireference, but has its drawbacks, and depending on which functionals are used to characterize a system, can yield very different results for the system. Functional hierarchy is characterized using "Jacob's ladder" first mentioned in the literature by Perdew and Schmidt where each rung of the ladder represents a family of density functional approximations climbing upwards towards chemical accuracy.[27] The first rung showcases the simplest density functionals, the local spin density approximations, where the exchange correlation energy depends only on the density.[27–29] LDAs tend to overbind molecules and although they have shown successful results in material science they are inaccurate for most chemical purposes.[28,29] The next rung features the Generalized Gradient Approximations (GGA) which rely on not only the density at each point, but also the gradient (i.e. how the density

changes in space). The GGA family is typically more accurate compared to LDA however no universal form exists. [28] The meta-GGA occupies the next rung dependent on Kohn Sham kinetic energy densities, and is the highest rung of the ladder not containing a computationally demanding requirement; hybrid functionals, those with added percent of HF exchange, and hyper GGAs occupy higher rungs of the ladder towards chemical accuracy.[27] Here we consider these functionals and their performance. A larger range is studied by Kulik *et.al.* but only ground state properties and energetics are investigated.[30] Here excited states are explored as will due to their importance for reactivity.

The GGA functional BLYP is a one parameter functional shown to fit exact exchange energies for noble gases helium to radon. [31,32] The Minnesota 2006 local functional (M06-L) belongs to the meta-GGA family designed by Zhao and Truhlar and parameterized to have good performance with both main group elements and transition metals.[33] GGA hybrids, the most popular being B3LYP and PBE0, mix the GGA component with some HF exchange, and the goal of the meta-GGA types of functionals is to perform comparable to hybrid functionals without the high cost associated with hybrid functionals.[28,34–36] Range-separated (RS) hybrid family includes the ωb97x functional developed to be free of long range self-interaction.[37] The hybrid version of the Tao, Perdew, Staroverov, and Scuseria functional (TPSSh), Minnesota 15 (MN15), and M06 functionals belong to meta-GGA-hybrid. TPSSh according to Kossman shows significant superiority to the non-hybrid version (TPSS).[38] A bioinorganic study by Jensen et al in 2008, suggests promising results for the use of the TPSSh functional in the bioinorganic field.[39] MN15 showed much broader accuracy than previous Minnesota functionals and has been shown the greatly characterize non-covalent interactions and a good functional for studying transition metals.[40,41] The M06 functional, an improvement over the previously mentioned M06-

L functional, is known for its broad applicability, parameterized to include both transition metals and non-metals, and recommended for organo- and inorganometallic chemistry and noncovalent interactions.[42]

Among the double hybrid family is the Perdew, Burke, and Enzerhof 0 double hybrid (PBE0-dh) functional showed a significant improvement compared to its parent functional, PBE, with the ratio of Hartree Fock, Kohn-Sham, and perturbation term participation.[28,43]

Density functional theory (DFT) is certainly a necessary tool, but in order to do things correctly we need to benchmark our functionals for some manageable systems and apply to other systems. Quantities of interest for these purposes of benchmarking are geometries, most notably the metal oxygen bond that changes with character, and chemical activity. The bond between a transition metal and oxygen is important across many fields of research: catalysis, biology, astrophysics, as well as other areas of chemistry. Moltved *et. al.* investigated the M-O bond for neutral and cationic transition metal oxides too understand their behavior and found that their strength decreased across the periodic table from early to late, and the bond directs the reaction energetics of the transition metal systems.[44]

Transition metals have many excited states which can be just as catalytically important as the ground state, which means an investigation into their chemical activity is as beneficial as benchmarking ground state energies.[45] In terms of chemical activity, efforts are focused on the activation barriers due to the importance of excited states. The effect of excited states on ground state chemistry can be seen with the reaction of $(H_3N)_5TiO^{2+}$ with methane, where the activation barrier is lowered if the metal oxide excited state is also lower, and the behavior of the excited state shifts the ground state behavior.[45]

Benchmarking requires the use of a manageable system. The system used here is transition metal oxide dication complexes. Transition metal oxide dications have been shown to be beneficial catalytically due to their unique electronic structure, and their ability to be oxo or oxyl with the help of ligands.[11,15,19,21,46] Machine learning guided analyses have been completed investigating transition metal complexes characterization with DFT and determining multireference character.[30,47] A study in 2021 investigated the electronic structure of these complexes to understand and categorize their behavior, but a question lies in what is the best way to characterize their behavior.[21] These catalysts have also been shown to be useful in water and methane activation.[11,15,46]

Here, we studied nine functionals across different DFT families for first-row $(H_3N)_5MO^{2+}$ and compared against multiple multi-reference methods to determine if a DFT functional can describe the ground and excited states of these systems as well as multireference methods. In Section II we describe the computational tools used in this study. Section III displays the results and discusses the performance of each functional compared to the wavefuntion (multireference and CCSD(T)) methods. Finally, section IV describes the conclusions of this study.

1. Computational Details

DFT optimizations were completed across six different families of functionals with nine representative functionals considered. One GGA (BLYP), one meta-GGA (M06-L), two GGA hybrid (B3LYP, PBE0), one RS hybrid (ωB97X), three meta-GGA hybrid (MN15, TPSSh, M06), and one double hybrid (PBE0-DH) to account for different parameterization factors. MN15 was used to optimize all geometries at the start due to its ability to characterize transition metals well, and these optimized geometries were used as the starting geometries for the

remaining functionals.[18] Most of the harmonic vibrational frequencies were found to be real, however some systems had small imaginary frequencies ~ -10 cm^{-1} corresponding to the internal rotations of ammonia, and despite our efforts we were not able to eliminate them.

A cc-pVTZ basis was placed on the metal, nitrogen, and hydrogen, and an aug-cc-pVTZ basis was placed on the oxygen to account for the anionic nature of the oxygen and polar nature of the metal-oxygen bond. Electronic configurations were obtained using the *stable=opt* keyword and applied to the optimization step with *guess=read*, DFT optimizations were calculated using Gaussian 16 software.[48,49]

Multireference calculations were completed at the CASSCF, MRCI, MRCI+Q, and CASPT2 levels of theory using Molpro software with the optimized geometries from DFT/MN15.[50] The use of DFT geometries for subsequent ab initio calculations is a common practice in the literature.[51–53] In all cases, the geometries have a near-C$_s$ symmetry, and thus they were symmetrized to C$_s$ for the subsequent CASSCF calculation to reduce the computational cost. The ten orbitals included in this active space are the 4s and 3d orbitals of the metal, the 2p orbitals of the oxygen, and a virtual A´´ orbital necessary to help convergence. The 2s orbital of oxygen and valence electrons of ammonia were kept inactive at CASSCF. At MRCI and CASPT2 the lone pairs of the five ammonia ligands were correlated (31 inactive/core orbitals). For the multireference calculations, a cc-pVDZ (DZ) basis was placed on the metal, nitrogen, and hydrogen and an aug-cc-pVDZ on oxygen for all methods except the CASPT2/TZ method, which used the corresponding triple-ζ (TZ) basis sets.

CCSD(T) calculations were done using the Gaussian 16 software[48,49] using the optimized geometry and electronic configurations obtained at the MN15 level. Different orbital spaces have been used for the electron correlation. FV-CCSD(T) pertains to the electron correlation of all

valence electrons (15 core orbitals), PV-CCSD(T) corresponds to the same space used for MRCI and CASPT2 (31 core orbitals), and C-CCSD(T) includes all valence electrons plus the $3s^2 3p^6$ subvalence electrons of the metal (11 core orbitals). Due to the increased computational cost, the DZ basis set is used for the CCSD(T) calculations. C-CCSD(T)/TZ energies were estimated by adding the difference between the CASPT2/DZ and CASPT2/TZ energies to the C-CCSD(T)/DZ energies.

2. Geometric Trends

Geometry optimization across multiple functionals and spins allows for the characterization of bond lengths of the complex to understand how they change. Figures 6.1, 6.2, and 6.3 display the bond length trends for the metal-oxygen bond (6.1), metal-axial ammonia bond (6.2), and the metal-equatorial ammonia bond (6.3). The bond lengths are characterized by spin on the x axis resulting in three columns; low spin (L), intermediate spin (I), and high spin (H). Each of the nine functionals is denoted by a different color diamond. Each plot has three rows of points, the bottom row corresponding to the minimum bond length of a particular functional, the middle row corresponding to the average bond length of the functional, and the top row for the maximum bond length of the functional. Generally, six of the nine functionals agree within 0.05 Å regardless of bond type, with the exception of outliers BLYP, M06-L, and PBE0-DH. BLYP, M06-L and PBE0-DH are the consistent outliers due to over or underestimation depending on the system and the remaining functionals agree within 0.05 Å regardless of bond type.

2.1 Metal-Oxygen Bond

The trends for the metal-oxygen bond are shown in Figure 6.1. For this bond type there is an overall increase in the bond length from low spin to high spin; with the averages starting at 1.65 Å for the low spin, 1.70 Å for the intermediate spin, and 1.96 Å for the high spin. This is as expected since the high spin is more commonly responsible for drawing out the oxyl character of the metal oxide as well as bond breakage. Moving from low to intermediate spin the range of bond lengths is similar for low and intermediate spin, and the average bond lengths are closer to the minimum bond lengths, which signifies that our sample has more (oxo) states with shorter bond lengths. The high spin however has the maximum bond lengths more separated from the minimum and average (~0.5-0.6 Å) compared to the smaller 0.20 Å separation for low and intermediate spins.
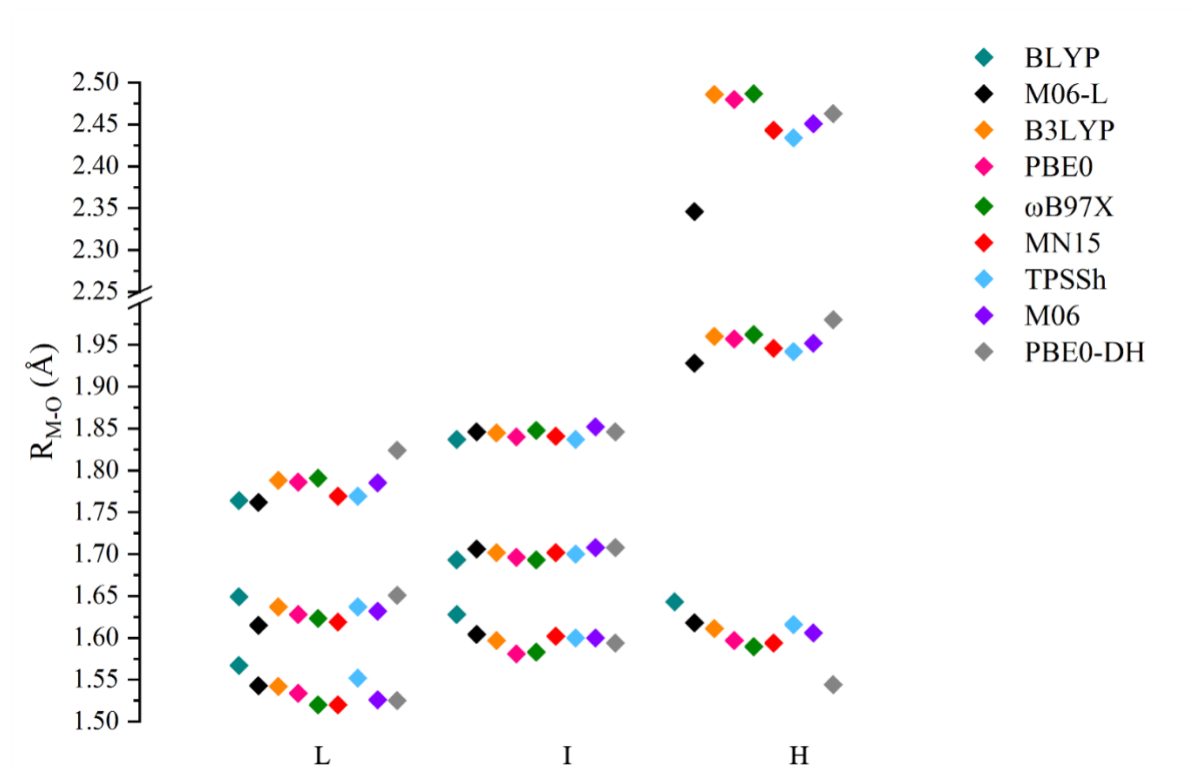
Figure 6.1: *Geometry MO bond across functionals, min avg and max for low int and high spin*

2.2 Metal-Axial Ammonia Bond

The average bond lengths between the metal and the axial ammonia are more consistent than for the metal oxygen bond ranging about 2.1-2.3 Å across all spins. However, they reveal the exact opposite trends compared to metal oxygen bonds regarding the ranges as they decrease going from low to high spin from 0.6 Å to 0.2 Å.

This opposing set of behavior between the metal oxygen bond and metal axial ammonia bond is likely due to a phenomenon known as trans influence. Trans influence is the impact of a ligand on the length of the bond trans to it in a tug of war manner.[54,55] In this case the two bonds are the metal oxygen bond and the metal ammonia bond trans to it. This can be easily visualized through the comparison of Figure 6.1 and 6.2. The metal axial ammonia bonds (Figure 6.2) decrease whenever the metal oxygen bonds increase.

Low spin metal axial ammonia bond is within 0.6 Å whereas for the metal oxygen is between 0.3 Å. Intermediate spin at 0.4 vs 0.3 Å for metal oxygen, and high spin metal axial 0.3 vs 1.0 Å for metal oxygen. Average bond length is relatively in the middle of the minimum and maximum bond lengths for the low spin and high spin realm. Intermediate spin realm has some favoritism for the maximum bond length.
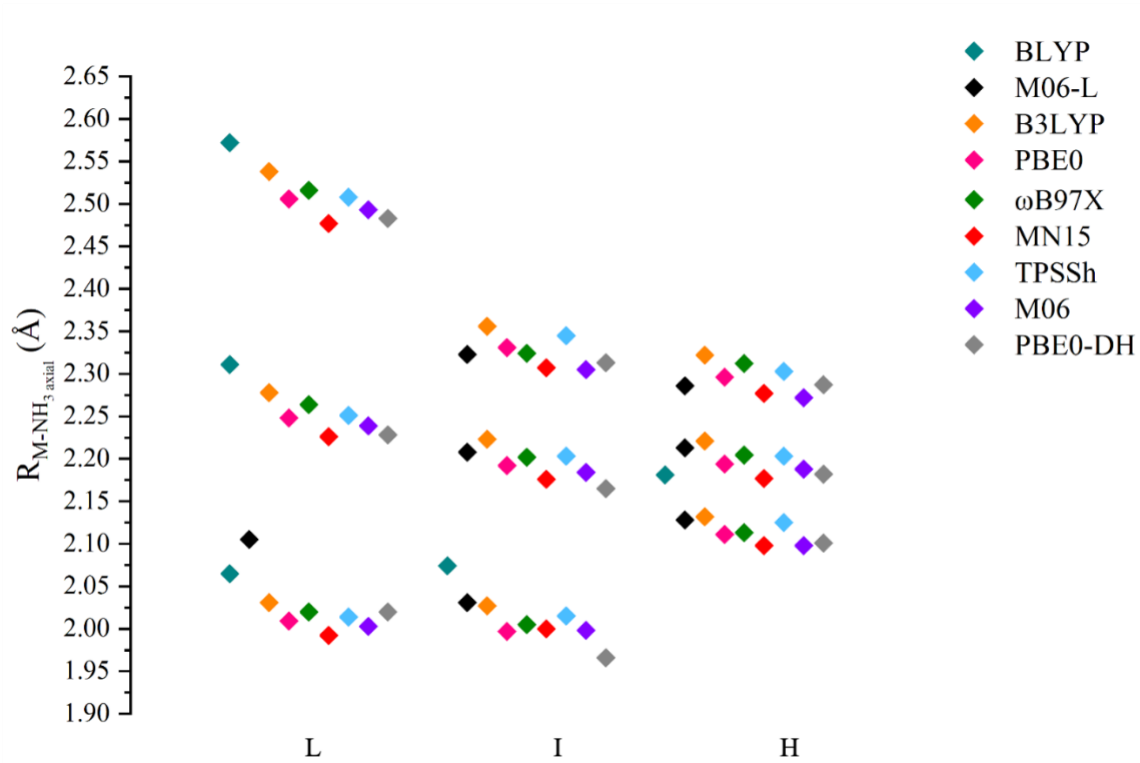
Figure 6.2: *Geometry M-NH₃ axial bond across functionals, min avg and max for low int and*

high spin

2.3 Metal-Equatorial Ammonia bond

Metal-equatorial ammonia bonds are shorter than the axial ammonia bonds, less than 2.35 Å everywhere whereas the axial ammonia bond ranges within 2.0 and 2.6 Å. The distance increases from low to high spin resembling the behavior of the metal oxygen bond and each spin bearing a similar range in bond length within 0.2 Å and unaffected by trans influence unlike the metal oxygen bond. The average bond length for this bond type is more evenly split between the maximum and minimum bond lengths as there are four contributing metal ammonia bonds.
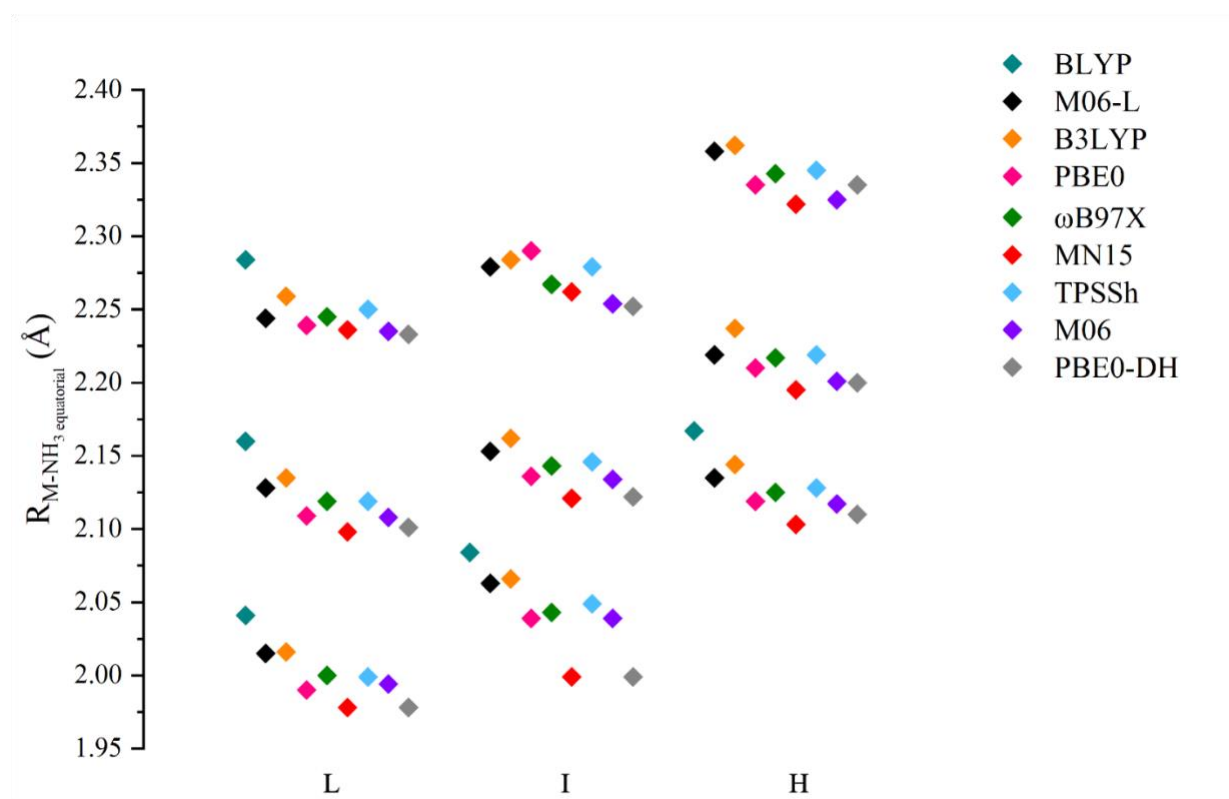
Figure 6.3: *Geometry M-NH₃ equatorial bond across functionals, min avg and max for low int and high spin*

3. Excitation Energies

The excitation energies for the first low spin, intermediate spin, and high spin states of each $(NH_3)_5MO^{2+}$ complex (M=Ti-Ni) and at different methods are listed in Table 6.1 (wavefunction-based methods) and 6.2 (DFT). The MN15 geometries have been used for all wavefunction based methods since the MN15 metal-oxygen and metal-nitrogen bond lengths are always in the middle of the range for the various functionals (see above). The multi-reference calculations indicated that the majority of the states can be described fairly well with a single Slater determinant (CI coefficient 0.8 or larger). Exceptions are low (S=0) and highest (S=3) spin states of Fe and all spin states for Ni, which have two major determinants with coefficients between 0.5 and 0.75. We confirmed that the CCSD(T) and DFT electronic configurations are identical to the major configuration of each state.

The increase of the basis set from DZ to TZ at the CASPT2 level of theory changes the excitation energies by $\sim\pm2,000$ cm^{-1} (maximum decrease 1540 cm^{-1} and maximum increase 2333 cm^{-1}). The average change is -14 cm^{-1}. A similar change is observed comparing CASPT2 and MRCI (maximum decrease 2439 cm^{-1}, maximum increase 2000 cm^{-1}, and average drop 51 cm^{-1}). The differences between CASPT2 and PV-CCSD(T) are considerably larger, and in the Fe case we observe differences of $\sim10,000$ cm^{-1} or larger. Recall that the same electrons are correlated in the two methods. We believe that the CCSD(T) results are more accurate since the considered states are of single-reference nature and that the CASPT2 results will be improved if we were able to increase the active space. Similar remarks have been made in the literature for non-transition metal containing molecules, and this is expected to be amplified for the present transition metal complexes due to the richer electronic structure.[25,56]The utilization of a second 3d-shell in the

active space has been suggested in the literature to improve CASPT2 results for transition metal compounds.[57]

The number of electrons that are correlated in the post-Hartree Fock of post-CASSCF methods is also important as indicated by the PV-CCSD(T)/DZ, FV-CCSD(T)/DZ, and C-CCSD(T)/DZ calculations. Besides the metallic electrons and the electrons of the metal-oxygen bond, the first includes the correlation from the lone pairs of ammonia, the second includes all valence electrons, and the last one includes also the subvalence metallic electrons. The excitation energies can change dramatically (several thousands of cm^{-1} in some cases) going from one method to the other, which shows the difficulty of studying accurately such complexes with wavefunction-based methods. Both the static and dynamic electron correlation are equally important. Here, we will consider that the C-CCSD(T)/TZ provides the best results.

The DFT values are compared graphically with the C-CCSD(T)/TZ and CASPT2/TZ results in Figure 6.4. The values for various density functionals are depicted with red circles (low spin), blue squares (intermediate spin) and green diamonds (high spin). For Fe only we included an even higher spin state (S=3) shown with purple stars. The C-CCSD(T)/TZ and CASPT2/TZ values are also represented with solid and dashed lines, respectively.

The first two metals, Ti and V, have very similar electronic structures. The low spin oxo state is well separated from the intermediate spin oxyl state, and the excitation energies at the C-CCSD(T)/TZ and CASPT2/TZ levels agree very well (within less than 10%). All functionals predict the low spin state as the ground state but they generally underestimate the excitation energy by a couple of thousands of wavenumbers (~10%). BLYP and M06 are closer to the ab initio values, while PBE0-DH has the clearly largest discrepancy. The rest of the functionals agree within 2,000 cm^{-1} with each other.

The low and intermediate spin states for Cr have very competitive energies with one or the other being the ground state depending on the level of theory. The only outlier is PBE0-DH, which erroneously predict that the intermediate spin state is very high in energy and actually lower than the high spin state, which is clearly the highest energy state in every other method. Similarly to Ti and V, the excitation energy for the high spin state is smaller in DFT compared to the C-CCSD(T)/TZ and CASPT2/TZ values.

The ground state for Mn is always the quartet state (intermediate spin state) except for PBE0-DH, which again overly favors the high spin state. The low spin doublet state is the first excited state for all methods except M06. The B3LYP, wB97x, MN15, and TPSSh excitation energies are within 200 cm^{-1} from the C-CCSD(T)/TZ. Finally, once again the high spin oxyl state is stabilized in DFT compared to C-CCSD(T)/TZ.

The case of iron is the most didactic one. Here the C-CCSD(T)/TZ and CASPT2/TZ results are very different from each other. The ground state in both cases is the high spin quintet state, but the excitation energies for the other spins are much higher for CASPT2/TZ (see solid and dashed lines in Figure 6.4). At C-CCSD(T)/TZ, the intermediate spin triplet state lies less than 1,000 cm^{-1} above the ground state, the low spin singlet state is less than 1,000 cm^{-1} higher, and the highest spin septet state is at ~8,000 cm^{-1}. Putting aside the BLYP, TPSSh, M06, and PBE0-DH, the rest of the functionals predict the correct energy order with the best agreement achieved by MN15. Finally, it should be stated that DFT agrees better with C-CCSD(T)/TZ and not CASPT2/TZ, supporting further our belief that C-CCSD(T)/TZ is more accurate.

For Co, the CASPT2/TZ excitation energy for the low spin state is much higher than C-CCSD(T)/TZ but the two methods agree for the high spin state. Except PBE0-DH, the remaining functionals predict the low and intermediate spin states energetically very close to each other. In

contrast with the previous observations, the excitation energy for the high spin state now is overestimated with the DFT methods. Finally, the Ni case is also very different with the CASPT2/TZ values being closer to DFT now, and not the C-CCSD(T)/TZ ones. Recall that the nickel complexes have the larger multi-reference character and this renders the CCSD(T) results less trustworthy. Both the CASPT2/TZ and DFT (except MN15 and PBE0-DH) results predict the three spin states to lie within 2,000 cm^{-1}.

Conclusively, we confirm the computational challenges known for transition metal complexes originating from their complex electronic structure. Our results show the importance of describing the static and dynamic correlation properly. We generally suggest that a good strategy is first perform CASSCF calculations. If the wavefunction appears to be dominated by a single electron configuration, then DFT calculations with a proper functional can be quite accurate. Among the functionals examined presently, the BLYP, M06, and PBE0-DH showed the poorest performance, while the remaining functionals are quite equivalent performing better or worse in a case-by-case basis. A general observation is that DFT underestimates the excitation energies of the high spin oxyl states, which implies that DFT may increase the radical character of metal oxygen bonds leading to lower activation barriers for the reaction of metal oxides with other molecules, such as CH_4 of H_2S but not H_2O.[58] The present conclusions cannot be generalized for highly multi-reference systems since the present systems are admittedly single reference and only the dynamic correlation is probed. The use of MRCI or CASPT2 seems to be more applicable to early transition metals, while for metal beyond Mn an extended active space (double 3d-shell) is necessary.
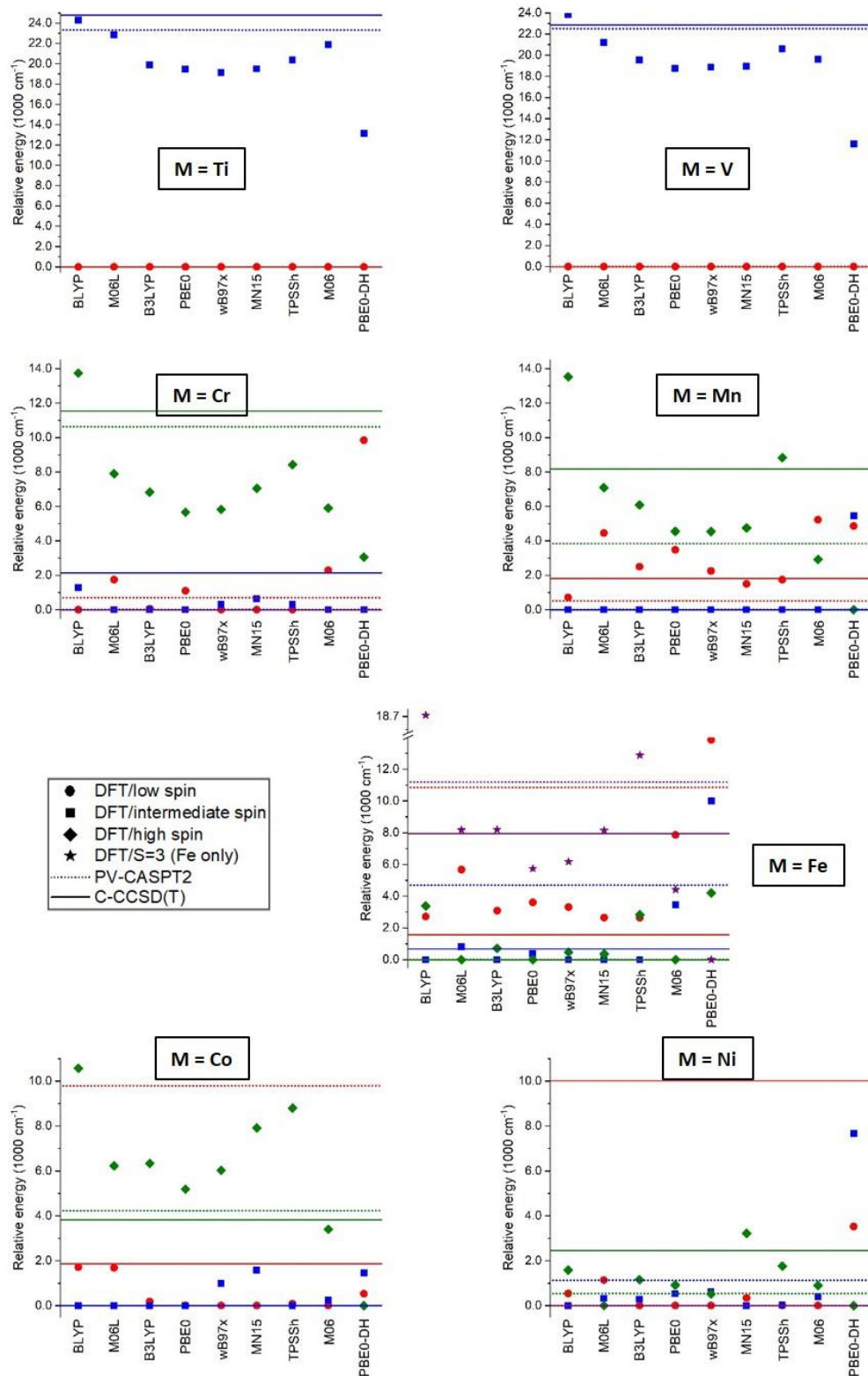
Figure 6.4: *Excitation energies for* $(NH_3)_5MO^{2+}$ *(M=Ti-Ni) at the DFT, CASPT2, and CCSD(T)*

levels of theory; see text for more details.

Table 6.1: *Relative energies (cm^{-1}) for the first low/intermediate/high spin states of $(NH_3)_5MO^{2+}$ at various wavefunction methods.*

M	MRCI/DZ	MRCI+Q/DZ	CASPT2/DZ	CASPT2/TZ	PV-CCSD(T)/DZ	FV-CCSD(T)/DZ	C-CCSD(T)/DZ	C-CCSD(T)/TZ
Ti (S=0)	0	0	0	0	0	0	0	0
Ti (S=1)	22258	22375	22558	23322	20956	21822	24013	24777
V (S=$^1/_2$)	0	0	0	0	0	0	0	0
V (S=$^3/_2$)	21749	21661	21607	22508	17295	20120	21974	22875
Cr (S=0)	1982	1874	1727	696	0	245	0	0
Cr (S=1)	0	0	0	0	3329	0	1101	2131
Cr (S=2)	9289	9414	9738	10637	4599	7326	9621	11551
Mn (S=$^1/_2$)	1480	2806	1246	509	10481	2429	2568	1831
Mn (S=$^3/_2$)	0	0	0	0	3034	0	0	0
Mn (S=$^5/_2$)	1099	3307	1507	3841	0	3891	5836	8169
Fe (S=0)	12292	10604	11932	10850	26230	8250	2641	1560
Fe (S=1)	6619	4508	5570	4695	11164	2952	1546	671
Fe (S=2)	0	0	0	0	3196	0	0	0
Fe (S=3)	7983	6833	9719	11195	0	5016	6453	7930
Co (S=$^1/_2$)	6873	3988	9312	9787	6037	1972	1386	1861
Co (S=$^3/_2$)	0	0	0	0	0	0	0	0
Co (S=$^5/_2$)	4170	4298	5770	4230	1443	4652	5371	3831
Ni (S=0)	3028	2373	1160	0	6411	9076	9939	10014
Ni (S=1)	4360	3223	2360	1125	0	208	0	0
Ni (S=2)	0	0	0	538	845	0	676	2448

Table 6.2: *Relative energies (cm^{-1}) for the first low/intermediate/high spin states of $(NH_3)_5MO^{2+}$ with various density functionals.*

M	BLYP	M06L	B3LYP	PBE0	wB97X	MN15	TPSSh	M06	PBE0-DH
Ti (S=0)	0	0	0	0	0	0	0	0	0
Ti (S=1)	24308	22816	19862	19444	19141	19499	20380	21850	13128
V (S=$^1/_2$)	0	0	0	0	0	0	0	0	0
V (S=$^3/_2$)	23863	21186	19549	18769	18854	18964	20595	19618	11587
Cr (S=0)	0	1743	60	1098	0	0	0	2293	9849
Cr (S=1)	1295	0	0	0	297	626	305	0	0
Cr (S=2)	13747	7898	6825	5661	5827	7056	8428	5906	3055
Mn (S=$^1/_2$)	713	4455	2498	3472	2256	1494	1741	5224	4862
Mn (S=$^3/_2$)	0	0	0	0	0	0	0	0	5468
Mn (S=$^5/_2$)	13533	7098	6087	4551	4541	4751	8837	2923	0
Fe (S=0)	2719	5675	3083	3611	3318	2648	2639	7855	13848
Fe (S=1)	0	817	0	371	0	0	0	3462	9990
Fe (S=2)	3375	0	714	0	466	363	2836	0	4199
Fe (S=3)	18752	8170	8196	5739	6170	8146	12883	4413	0
Co (S=$^1/_2$)	1711	1680	186	1	0	0	88	0	529
Co (S=$^3/_2$)	0	0	0	0	983	1572	0	236	1458
Co (S=$^5/_2$)	10570	6229	6333	5191	6031	7913	8800	3401	0
Ni (S=0)	546	1144	0	0	0	339	0	0	3524
Ni (S=1)	0	324	288	535	615	0	31	396	7661
Ni (S=2)	1586	0	1157	914	517	3220	1758	903	0

1   K. A. Jørgensen, Transition-Metal-Catalyzed Epoxidations, *Chem Rev*, 1989, **89**, 431–458.
2   R. A. Periana, D. J. Taube, S. Gamble, H. Taube, T. Satoh and Fujii Hiroshi, Platinum Catalysts for the High-Yield Oxidation of Methane to Methanol Derivative, *Science (1979)*, 1988, **280**, 560–564.
3   K. Eller and H. Schwarz, Organometallic Chemistry in the Gas Phase, *Chem. Rev.*, 1991, **91**, 1121–1177.
4   J. Xu, M. T. Rodgers, J. B. Griffin and P. B. Armentrouf, Guided ion beam studies of the reactions of V+n (n=2-17) with O2: Bond energies and dissociation pathways, *Journal of Chemical Physics*, 1998, **108**, 9339–9350.
5   C. A. Gaggioli, J. Sauer and L. Gagliardi, Hydrogen Atom or Proton Coupled Electron Transfer? C-H Bond Activation by Transition-Metal Oxides, *J Am Chem Soc*, 2019, **141**, 14603–14611.
6   A. Nandy, C. Duan, C. Goffinet and H. J. Kulik, New Strategies for Direct Methane-to-Methanol Conversion from Active Learning Exploration of 16 Million Catalysts, *J Am Chem Soc*, 2022, **2**, 1200–1213.
7   K. Nassiri Nazif, A. Daus, J. Hong, N. Lee, S. Vaziri, A. Kumar, F. Nitta, M. E. Chen, S. Kananian, R. Islam, K. H. Kim, J. H. Park, A. S. Y. Poon, M. L. Brongersma, E. Pop and K. C. Saraswat, High-specific-power flexible transition metal dichalcogenide solar cells, *Nat Commun*, , DOI:10.1038/s41467-021-27195-7.
8   I. Becerril-Romero, D. Sylla, M. Placidi, Y. Sánchez, J. Andrade-Arvizu, V. Izquierdo-Roca, M. Guc, A. Pérez-Rodríguez, S. Grini, L. Vines, B. Pusay, R. Almache, J. Puigdollers, P. Pistor, E. Saucedo and M. Espíndola-Rodríguez, Transition-Metal Oxides for Kesterite Solar Cells Developed on Transparent Substrates, *ACS Appl Mater Interfaces*, 2020, **12**, 33656–33669.
9   Y. Kim, S. Lee, J.-G. Song, K. Yong Ko, W. Je Woo, S. Woo Lee, M. Park, H. Lee, Z. Lee, H. Choi, W.-H. Kim, J. Park, H. Kim, Y. Kim, S. Lee, J. Song, K. Y. Ko, W. J. Woo, J. Park, H. Kim, S. W. Lee, Z. Lee, K. M. Park, H. Lee, H. Choi and W. Kim, Transition Metal Dichalcogenide Heterostructures for p-and n-Type Photovoltaic Self-Powered Gas Sensor, *Adv Funct Mater*, 2020, **30**, 2003360.
10   E. Lee, Y. S. Yoon and D. J. Kim, Two-Dimensional Transition Metal Dichalcogenides and Metal Oxide Hybrids for Gas Sensing, *ACS Sens*, 2018, **3**, 2045–2060.
11   I. R. Ariyarathna and E. Miliordos, Ab initio investigation of the ground and excited states of MoO+,2+,- and their catalytic strength on water activation, *Physical Chemistry Chemical Physics*, 2018, **20**, 12278–12287.
12   I. R. Ariyarathna and E. Miliordos, Ab initio investigation of the ground and excited states of TcO+ and RhO+, *J Quant Spectrosc Radiat Transf*, 2022, **280**, 108074.
13   I. R. Ariyarathna and E. Miliordos, Ab initio investigation of the ground and excited states of ZrO + and NbO +, *J Quant Spectrosc Radiat Transf*, 2020, **255**, 107265.
14   N. M. S. Almeida, I. R. Ariyarathna and E. Miliordos, Ab initio calculations on the ground and excited electronic states of neutral and charged palladium monoxide, PdO0,+,-, *Physical Chemistry Chemical Physics*, 2018, **20**, 14578–14586.

15   N. M. S. Almeida, I. R. Ariyarathna and E. Miliordos, O-H and C-H Bond Activations of Water and Methane by RuO2+ and (NH3)RuO2+: Ground and Excited States, *Journal of Physical Chemistry A*, 2019, **123**, 9336–9344.

16   I. R. Ariyarathna, N. M. S. Almeida and E. Miliordos, Ab initio investigation of the ground and excited states of RuO+,0,-and their reaction with water, *Physical Chemistry Chemical Physics*, 2020, **22**, 16072.

17   S. N. Khan and E. Miliordos, Electronic Structure of RhO2+, Its Ammoniated Complexes (NH3)1-5RhO2+, and Mechanistic Exploration of CH4Activation by Them, *Inorg Chem*, 2021, **60**, 16111–16119.

18   S. N. Khan and E. Miliordos, Methane to Methanol Conversion Facilitated by Transition-Metal Methyl and Methoxy Units: The Cases of FeCH3+ and FeOCH3+, *Journal of Physical Chemistry A*, 2019, **123**, 5590–5599.

19   J. K. Kirkland, S. N. Khan, B. Casale, E. Miliordos and K. D. Vogiatzis, Ligand field effects on the ground and excited states of reactive FeO2+ species, *Physical Chemistry Chemical Physics*, 2018, **20**, 28786.

20   E. E. Claveau and E. Miliordos, Quantum chemical calculations on NbO and its reaction with methane: Ground and excited electronic states, *Physical Chemistry Chemical Physics*, 2019, **21**, 26324–26332.

21   E. E. Claveau and E. Miliordos, Electronic structure of the dicationic first row transition metal oxides, *Physical Chemistry Chemical Physics*, 2021, **23**, 21172–21182.

22   B. A. Jackson and E. Miliordos, Weak-field ligands enable inert early transition metal oxides to convert methane to methanol: The case of ZrO, *Physical Chemistry Chemical Physics*, 2020, **22**, 6606–6618.

23   S. Sader and E. Miliordos, Methane to methanol conversion facilitated by anionic transition metal centers: The case of Fe, Ni, Pd, and Pt, *Journal of Physical Chemistry A*, 2021, **125**, 2364–2373.

24   J. Wang, S. Manivasagam and A. K. Wilson, Multireference Character for 4d Transition Metal-Containing Molecules, *J Chem Theory Comput*, 2015, **11**, 5865–5872.

25   K. D. Vogiatzis, M. V. Polynski, J. K. Kirkland, J. Townsend, A. Hashemi, C. Liu and E. A. Pidko, Computational Approach to Molecular Catalysis by 3d Transition Metals: Challenges and Opportunities, *Chem Rev*, 2019, **119**, 2453–2523.

26   P. Geerlings, F. De Proft and W. Langenaeker, Conceptual density functional theory, *Chem Rev*, 2003, **103**, 1793–1873.

27   J. P. Perdew, Jacob's ladder of density functional approximations for the exchange-correlation energy, *AIP Conf Proc*, 2003, **577**, 1–20.

28   D. Rappoport, N. R. M. Crawford, F. Furche and K. Burke, *Which functional should I choose?*, 2008.

29   W. Kohn and L. J. Sham, PHYSICAL REVIEW Self-Consistent Equations Including Exchange and Correlation Effects*, *Physical Review*, 1965, **140**, 1133–1138.

30   C. Duan, S. Chen, M. G. Taylor, F. Liu and H. J. Kulik, Machine learning to tame divergent density functional approximations: A new path to consensus materials design principles, *Chem Sci*, 2021, **12**, 13021–13036.

31   A. D. Becke, Density-functional exchange-energy approximation with correct asymptotic behavior, *Phys Rev A (Coll Park)*, 1988, **38**, 3098–3100.

32   C. Lee, W. Yang and R. G. Parr, Development of the Colic-Salvetti correlation-energy formula into a functional of the electron density, *Phys Rev B*, 1988, **37**, 785–789.

33   Y. Zhao and D. G. Truhlar, A new local density functional for main-group thermochemistry, transition metal bonding, thermochemical kinetics, and noncovalent interactions, *Journal of Chemical Physics*, 2006, **125**, 194101.

34   P. J. Stephens, F. J. Devlin, C. F. Chabalowski and M. J. Frisch, LETTERS Ab Initio Calculation of Vibrational Absorption and Circular Dichroism Spectra Using Density Functional Force Fields, *Journal of Physical Chemistry*, 1994, **98**, 11623–11627.

35   A. D. Becke, Density-functional thermochemistry. III. The role of exact exchange, *J Chem Phys*, 1993, **98**, 5648–5652.

36   J. Heyd, G. E. Scuseria and M. Ernzerhof, Hybrid functionals based on a screened Coulomb potential, *Journal of Chemical Physics*, 2003, **118**, 8207–8215.

37   J. Da Chai and M. Head-Gordon, Systematic optimization of long-range corrected hybrid density functionals, *Journal of Chemical Physics*, 2008, **128**, 084106.

38   S. Kossmann, B. Kirchner and F. Neese, Performance of modern density functional theory for the prediction of hyperfine structure: Meta-GGA and double hybrid functionals, *Mol Phys*, 2007, **105**, 2049–2071.

39   K. P. Jensen, Bioinorganic chemistry modeled with the TPSSh density functional, *Inorg Chem*, 2008, **47**, 10357–10365.

40   H. S. Yu, X. He, S. L. Li and D. G. Truhlar, MN15: A Kohn-Sham global-hybrid exchange-correlation density functional with broad accuracy for multi-reference and single-reference systems and noncovalent interactions, *Chem Sci*, 2016, **7**, 5032–5051.

41   S. N. Khan and E. Miliordos, Methane to Methanol Conversion Facilitated by Transition-Metal Methyl and Methoxy Units: The Cases of FeCH3+ and FeOCH3+, *Journal of Physical Chemistry A*, 2019, **123**, 5590–5599.

42   Y. Zhao and D. G. Truhlar, The M06 suite of density functionals for main group thermochemistry, thermochemical kinetics, noncovalent interactions, excited states, and transition elements: Two new functionals and systematic testing of four M06-class functionals and 12 other functionals, *Theor Chem Acc*, 2008, **120**, 215–241.

43   E. Brémond and C. Adamo, Seeking for parameter-free double-hybrid functionals: The PBE0-DH model, *Journal of Chemical Physics*, 2011, **135**, 024106.

44   K. A. Moltved and K. P. Kepp, The chemical bond between transition metals and Oxygen: Electronegativity, d-Orbital Effects, and Oxophilicity as Descriptors of Metal-Oxygen Interactions, *Journal of Physical Chemistry C*, 2019, **123**, 18432–18444.

45   E. E. Claveau, S. Sader, B. A. Jackson, S. N. Khan and E. Miliordos, Transition metal oxide complexes as molecular catalysts for selective methane to methanol transformation: Any prospects or time to retire?, *Physical Chemistry Chemical Physics*, 2023, **25**, 5313.

46   S. N. Khan and E. Miliordos, Electronic Structure of RhO2+, Its Ammoniated Complexes (NH3)1-5RhO2+, and Mechanistic Exploration of CH4Activation by Them, *Inorg Chem*, 2021, **60**, 16111–16119.

47   H. J. Kulik, F. Liu and C. Duan, Rapid detection of strong correlation with machine learning for transition-metal complex high-throughput screening, *Journal of Physical Chemistry Letters*, 2020, **11**, 8067–8076.

48   M. J. Frisch, G. W. Trucks, H. E. Schlegel, G. E. Scuseria, M. A. Robb, J. R. Cheeseman, G. Scalmani, V. Barone, G. A. Petersson, Farkas. O., J. B. Foresman and J. D. Fox, *Gaussian, Inc., Wallingford CT,* 2016.

49   M. J. ; T. Frisch G. W.; Schlegel, H. B.; Scuseria, G. E.; Robb, M. A.; Cheeseman, J. R.; Scalmani, G.; Barone, V.; Petersson, G. A.; Nakatsuji, H.; Li, X.; Caricato, M.; Marenich,

A. V.; Bloino, J.; Janesko, B. G.; Gomperts, R.; Mennucci, B.; Hratch, D. J., Gaussian 16, Rev. B.01, *Gaussian, Inc., Wallingford, CT*.

50   H.-J. Werner and P. J. Knowles, MOLPRO, version 2015.1, a package of ab initio programs, *Chem. Phys. Letters*, , DOI:10.1063/1.448627.

51   A. V. Marenich, S. V. Jerome, C. J. Cramer and D. G. Truhlar, Charge model 5: An extension of hirshfeld population analysis for the accurate description of molecular interactions in gaseous and condensed phases, *J Chem Theory Comput*, 2012, **8**, 527–541.

52   M. G. Delcey, K. Pierloot, Q. M. Phung, S. Vancoillie, R. Lindh and U. Ryde, Accurate calculations of geometries and singlet-triplet energy differences for active-site models of [NiFe] hydrogenase, *Physical Chemistry Chemical Physics*, 2014, **16**, 7929–7938.

53   V. Bernales, A. B. League, Z. Li, N. M. Schweitzer, A. W. Peters, R. K. Carlson, J. T. Hupp, C. J. Cramer, O. K. Farha and L. Gagliardi, Computationally Guided Discovery of a Catalytic Cobalt-Decorated Metal-Organic Framework for Ethylene Dimerization, *Journal of Physical Chemistry C*, 2016, **120**, 23576–23583.

54   M. Gregson, E. Lu, D. P. Mills, F. Tuna, E. J. L. McInnes, C. Hennig, A. C. Scheinost, J. McMaster, W. Lewis, A. J. Blake, A. Kerridge and S. T. Liddle, The inverse-trans-influence in tetravalent lanthanide and actinide bis(carbene) complexes, *Nat Commun*, , DOI:10.1038/ncomms14137.

55   A. Takahashi, D. Yamaki, K. Ikemura, T. Kurahashi, T. Ogura, M. Hada and H. Fujii, Effect of the axial ligand on the reactivity of the oxoiron(IV) porphyrin π-cation radical complex: Higher stabilization of the product state relative to the reactant state, *Inorg Chem*, 2012, **51**, 7296–7305.

56   Z. Azizi, B. O. Roos and V. Veryazov, How accurate is the CASPT2 method?, *Physical Chemistry Chemical Physics*, 2006, **8**, 2727.

57   L. Freitag, S. Knecht, S. F. Keller, M. G. Delcey, F. Aquilante, T. Bondo Pedersen, R. Lindh, M. Reiher and L. González, Orbital entanglement and CASSCF analysis of the Ru-NO bond in a Ruthenium nitrosyl complex, *Physical Chemistry Chemical Physics*, 2015, **17**, 14383–14392.

58   G. He, S. Huang, L. F. Villalobos, J. Zhao, M. Mensi, E. Oveisi, M. Rezaei and K. V. Agrawal, High-permeance polymer-functionalized single-layer graphene membranes that surpass the postcombustion carbon capture target, *Energy Environ Sci*, 2019, **12**, 3305–3312.

Appendix A: Supporting Material for Chapter 3

Appendix A contains a full copy of the following article

Emily. E. Claveau and **E. Miliordos**, *Physical Chemistry Chemical Physics* <u>21</u>, 26324 (2019)

PCCP

PAPER

Check for updates

Quantum chemical calculations on NbO and its reaction with methane: ground and excited electronic states†

Emily E. Claveau and Evangelos Miliordos ⓘ *

Multi-reference configuration interaction and coupled cluster calculations were performed in conjunction with large basis sets for neutral NbO. We report accurate bond lengths, harmonic vibrational frequencies, anharmonicities, excitation energies, dipole moments, binding energies, and spin–orbit splittings, for the ground state $^4\Sigma^-$ and several excited electronic states. Potential energy curves were constructed for both the anion and neutral species. The potential energy curves for NbO$^-$ revealed its ground state as $^3\Sigma^-$, the same as for NbO$^+$. The calculated ionization energies and electron affinities are in excellent agreement with experiment. Bonding patterns were proposed for several electronic states. Doublet and quartet states are better described as Nb^{2+}O^{2-} with a closed shell oxygen terminal and a niobium center with three localized electrons. The reaction of these states with CH$_4$ occurs *via* a [2+2] mechanism and leads to a highly endothermic reaction with large activation energy barriers. On the other hand, the lowest sextet state of NbO (Nb^{3+}O$^{\bullet-}$) can produce methanol through a radical mechanism with small energy barriers.

I. Introduction

Studies of transition metal compounds especially transition metal oxides have been motivated by their many industrial applications. The energy band structure and the multiple crystal structures of solid niobium oxides (NbO, NbO$_2$, or Nb$_2$O$_5$) have enabled their use in gas sensors, electrochromics, solid electrolytic capacitors, transparent conductive oxides, and most recently rechargeable batteries.[1–3] Nb$_2$O$_5$ has also shown promise as a catalyst for the degradation of toxic organic dyes such as methylene blue.[4] Niobium has the ability to play multiple roles in catalysis, working as the active phase, dopant, and support. This high catalytic activity of niobium results from its redox property, high acidity, and strong interaction between the metal and support materials.[5] The presence of small amounts of niobium oxides enhances the activity, selectivity, and life of the catalyst.[6,7] On a different note, the presence of NbO in stellar bodies is still debatable,[8–10] as opposed to its first row transition metal analog, VO.[11,12] Given the importance of niobium oxides, there have been several experimental studies on the electronic structure of the base NbO unit.

Department of Chemistry and Biochemistry, Auburn University, Auburn, AL 36849-5312, USA. E-mail: emiliord@auburn.edu

† Electronic supplementary information (ESI) available: Optimal geometries, harmonic vibrational frequencies, and energetics for all intermediates and transition states for the NbO + CH$_4$ reaction. The MRCI PECs for NbO$^-$ are also given. See DOI: 10.1039/c9cp05408a

In 1987, Dyke *et al.* recorded the first photoelectron spectrum of NbO and measured its first ionization energy as IE = 7.91 ± 0.02 eV.[13] The authors performed Hartree–Fock calculations on the ground state, referred to as $^4\Sigma^-$, and calculated the NbO distance r_e = 1.682 Å and harmonic vibrational frequency ω_e = 983 cm^{-1}. These values are in agreement with the earlier experimental data of r_e = 1.691 Å and ω_e = 989 cm^{-1}.[14] The same year Merer *et al.* observed the B$^4\Pi$ ← X$^4\Sigma^-$ transition of the optical spectrum, and detected a second order spin–orbit splitting of 62 cm^{-1} between the higher X$^4\Sigma_{3/2}$ and lower X$^4\Sigma_{1/2}$ energy components.[15] Langhoff and Bauschlicher theoretically explored five low-lying electronic states (X$^4\Sigma^-$, A$^4\Phi$, B$^4\Pi$, C$^4\Pi$, and a$^2\Delta$) by means of multireference configuration interaction (MRCI).[16] Four years later, Siegbahn applied the modified coupled pair functional technique reporting r_e = 1.71 Å and a binding energy D_e of 159.7 kcal mol^{-1}.[17] Dolg *et al.* used MRCI methodologies to study the ground and first excited electronic states of NbO providing r_e, ω_e, D_e, and dipole moments μ_e.[18]

The first systematic spectroscopic work on the doublet manifold belongs to Launila *et al.*, who listed several spectroscopic constants for a$^2\Delta$, b$^2\Sigma^-$, c$^2\Pi$, d$^2\Delta$, e$^2\Phi$, and f$^2\Pi$.[19] The reaction of Nb with ^{16}O$_2$ and ^{18}O$_2$ is examined with matrix isolation IR by Zhou and Andrews and the vibrational frequencies of the produced Nb^{16}O and Nb^{18}O are given as 970.6 and 923.5 cm^{-1} respectively.[20] In 1998, Loock *et al.* measured the ionization energy of NbO by means of photoionization efficiency spectroscopy and mass-analyzed threshold ionization.[21] Their value of 7.154 ± 0.001 eV is ~0.75 eV smaller than that of

121

Dyke *et al.* (see above). Using an earlier reported binding energy for NbO$^+$ and its IE, Loock *et al.* estimated the binding energy for the ground state of NbO to be equal to 7.53 ± 0.11 eV. Next, Kingston *et al.* analysed the hyperfine structure of the B$^4\Pi$ ← X$^4\Sigma$ transition providing rotational and spin–orbit constants for the B$^4\Pi$ $_{1/2,1/2,3/2,5/2}$ components.[22] To our knowledge, the most recent work on NbO belongs to Kharat, who performed density functional theory (DFT) calculations on the ground quartet and first doublet electronic states.[23]

Presently, we perform the first systematic high level electronic structure investigation on NbO reporting bond lengths, excitation energies, spectroscopic constants, dipole moments, binding energies, bonding patterns, ionization energies, electron affinities, and spin–orbit coupling constants for the lowest eighteen electronic states. This work is part of our ongoing investigation regarding first and second-row transition metal monoxides.[12,24–28] Our results are compared with the existing experimental data and are expected to assist future spectroscopic studies. We also compare the electronic structure of NbO with its first-row transition metal oxide counterpart (VO). In addition, we examine the reaction of the low lying states of NbO with methane in an attempt to clarify the role of the electronic structure in the C–H activation process. In Section II, we describe the employed methods. In Section III, we report and discuss our results. Our findings are summarized in Section IV.

II. Computational details

The multi-reference configuration interaction (MRCI) technique was employed to solve the electronic Schrödinger equation. All valence electrons are correlated, and the reference wave function was obtained at the complete active space self-consistent field (CASSCF) level. The active space consists of nine electrons allocated in twelve orbitals. These twelve orbitals at infinity correspond to 2p of oxygen, and 5s, 4d, and 5p of niobium. Although the 5p orbitals of niobium are only partially occupied at every Nb–O distance, they were found to be necessary for the smooth convergence of the CASSCF iterations. The 2s electrons of oxygen are not included in the CASSCF active space, but they are promoted to virtual orbitals at the MRCI level. The Davidson correction (MRCI+Q) was also applied to account for part of the missing dynamic correlation and alleviate the size extensivity errors. In addition, for selected states with dominant single reference character, the coupled cluster singles, doubles, and perturbatively connected triples method, CCSD(T), was considered. For CCSD(T), we performed calculations where the sub-valence 4s^{2}4p^6 electrons of niobium are correlated, this is denoted as C-CCSD(T). Finally, we performed spin–orbit coupling calculations by adding the Breit–Pauli spin–orbit operator to the electronic Hamiltonian and diagonalizing the new Hamiltonian matrix in the basis of the unperturbed MRCI wave functions at 1.7 Å.

The correlation consistent family of basis sets is currently used, specifically the cc-pV5Z-PP and aug-cc-pV5Z sets for niobium and oxygen, respectively.[29–32] The former includes

the Stuttgart relativistic effective core pseudopotential replacing the first 28 electrons of niobium, 1s^{2}2s^{2}2p^{6}3s^{2}3p^{6}3d^{10}. The latter basis set is equipped with a series of diffuse functions to facilitate the description of the polarized Nb$^{\delta+}$O$^{\delta-}$ bond. The total number of basis functions for the two atoms are 7s7p6d4f3g2h1i (Nb) and 7s6p5d4f3g2h (O). When excitations from the inner 4s^{2}4p^6 electrons of niobium are allowed, the corresponding weighted-core cc-pwCV5Z set is used resulting in the addition of 2s2p2d1f1g1h1i functions on niobium.[32]

The highest Abelian C_{2v} subgroup of the full $C_{\infty v}$ molecular point group was selected. Spectroscopic constants were evaluated by numerically solving the ro-vibrational Schrödinger equation. Dipole moments are calculated as expectation values and as the linear response to an applied electric field (μ_{FF}) of intensity ±0.001 a.u. along the interatomic axis (finite field approach). All multi-reference and coupled cluster electronic structure calculations were done with MOLPRO2015.[33]

For the NbO + CH$_4$ reaction, we performed CASSCF, CCSD(T), and density functional theory (DFT) calculations using the MN15 functional.[34] CASSCF was used to study the first step of the reaction, NbO + CH$_4$ → CH$_3$NbOH. The active space for this study consists of eleven electrons in eleven orbitals. These orbitals correspond to nine molecular orbitals of NbO and the bonding and anti-bonding molecular orbitals of the activated C–H bond. The three orbitals of NbO corresponding to niobium 5p orbitals at long distances remain inactive since their contribution at equilibrium distances is minor (see below). For the two-step reaction NbO + CH$_4$ → Nb + CH$_3$OH, we performed CCSD(T) single point energy calculations using the MN15 optimized structures (CCSD(T)//MN15). We found that this approach for a similar CH$_4$ + N$_2$O → CH$_3$OH + N$_2$ reaction facilitated by FeCH$_3^+$ gives reasonable agreement with CCSD(T)// CCSD(T).[35] To assess the multi-reference character of all intermediates and transition states we used two criteria. First, using the same active space (11 electrons/11 orbitals) we performed CASSCF calculations and recorded the largest coefficient of the CI vector. Second, we monitored the T1 diagnostic obtained at the CCSD level. Substantial single reference character in almost all cases (see below) validates the use of CCSD(T). Triple-ζ basis sets are used for these calculations. All DFT calculations were done with Gaussian16.[36]

III. Results and discussion

IIIA. NbO

The ground state of Nb is a ^{6}D state with a 5s^{1}4d^4 electronic configuration. Besides Cr and Mo, which prefer the high-spin s^{1}d^5 half-filled valence shell, Nb is the only other metal with an s^1 ground state configuration. Its first excited state ^{4}F of s^2 character (5s^{2}4d^3) lies 1486 cm^{-1} (M_J averaged difference) above the ground state.[37] The combination of the ground state fragments Nb(^{6}D) + O(^{3}P) generates one Σ^+, two Σ^-, three Π, two Δ, and one Φ state of quartet, sextet, and octet spin multiplicities, grouped succinctly as ^{4,6,8}[Σ^+(1), Σ^-(2), Π(3), Δ(2), Φ(1)]. The next channel Nb(^{4}F) + O(^{3}P) produces the ^{2,4,6}[Σ^+(2), Σ^-(1), Π(3), Δ(3), Φ(2), Γ(1)] manifold of

122

states. Electronic states coming from the first and second channels are expected to have a local (*in situ*) $5s^1$ and $5s^2$ niobium center, respectively.

Considering the ionic (M^+O^-) nature of the first and second row transition metal oxides,[12,26,27] electronic states stemming from the combination of the low-lying states of Nb^+ with O should be taken into account. The first two states of Nb^+ $^5D(4d^4)$ and $^5F(5s^14d^3)$ produce the $^{4,6}[\Sigma^+(2), \Sigma (1), \Pi(3), \Delta(1), \Phi(1)]$ and $^{4,6}[\Sigma^+(2), \Sigma (1), \Pi(3), \Delta(3), \Phi(2), \Gamma(1)]$ groups, respectively. Overall, the contributions of the neutral and ionic species are expected to create a plethora of multi-reference low-lying electronic states for NbO. Indeed, this is the case for the first eighteen states, which are of doublet and quartet spin multiplicities and have $4s^0$, $4s^1$, and $4s^2$ *in situ* niobium character. The dominant electronic configurations for all of these states are listed in Table 1 and the corresponding molecular orbitals are shown in Fig. 1. In all cases the 1σ, 2σ, and 1π orbitals corresponding to 1s(O), Nb–O σ and Nb–O π-bonds are doubly occupied. The remaining three valence electrons reside at orbitals mainly localized on niobium determining the overall symmetry of each state. The three molecular orbitals corresponding to niobium 5p orbitals at long Nb–O distances, which are part of the active space, are not shown in Fig. 1 and not listed in Table 1. Although they were found to be necessary for technical reasons (convergence issues), their occupation is small and they do not contribute to the dominant equilibrium configurations.

The ground state is $^4\Sigma^-$ with the three symmetry determining electrons occupying the 3σ and 1δ orbitals. The bonding scheme is presented in Fig. 2 showing the valence-bond-Lewis (vbL) diagram, where the niobium atomic orbitals are depicted as lines. In this scheme the $^4\Sigma^-$ state is formed from $Nb^+(^5F; 5s^14d^3)$ and $O^-(^2P)$. The $2p_x$ and $2p_y$ electrons of oxygen are only partially donated to niobium, while the σ-bond between the $4d_{z^2}$ orbital of niobium and the $2p_z$ orbital of oxygen is largely polarized towards oxygen (see Fig. 1). Overall, the equilibrium wave function points more towards a metal–oxo (O^{2-}) picture.

The first excited state $^2\Delta$ can be produced from the ground state by promoting one 1δ electron to the 3σ orbital. The $3\sigma^21\delta^1$ configuration signals an *in situ* $5s^2$ niobium terminal suggesting the origin of this state as $Nb(^4F; 5s^24d^3) + O(^3P)$. The binding between neutral niobium and oxygen atoms is depicted in Fig. 2. The $2p_z^2$ electron pair of oxygen makes a partial dative bond with the $4d_{z^2}$ orbital of Nb with its $5s^2$ electrons becoming polarized away from oxygen. The presence of an electron pair at the back of niobium is expected to oppose the dipole moment of the strong ionic character of the 2σ and 1π bonds resulting in a smaller overall dipole moment for $^2\Delta$.

The next three states are of doublet spin multiplicity and bear a $3\sigma^11\delta^2$ configuration. In the lowest state $1^2\Sigma^-$ the three orbitals are singly occupied similar to the ground $X^4\Sigma^-$ state, but one of the electrons has opposite spin. In the $1^2\Gamma$ and $1^2\Sigma^+$ states the 1δ electrons are coupled into a singlet and occupy either $1\delta_{xy}$ or $1\delta_{x^2-y^2}$. The two different configurations are combined with either a negative or a positive sign to give the $1^2\Gamma$ and $1^2\Sigma^+$ wave functions, respectively (see Table 1 and Fig. 2).

Table 1 Dominant electronic configurations for the lowest electronic states of NbO. $1\sigma^22\sigma^21\pi^4$ is implied for all states (MOs are shown in Fig. 1)

State	Coef.	3σ	4σ	$2\pi_x$	$2\pi_y$	$1\delta_{xy}$	$1\delta_{x^2-y^2}$
$X^4\Sigma^-$	0.94	α	0	0	0	α	α
$1^2\Delta^a$	0.86	2	0	0	0	α	0
$1^2\Sigma^-$	0.71	β	0	0	0	α	α
	−0.36	α	0	0	0	β	α
	−0.36	α	0	0	0	α	β
$1^2\Gamma^a$	0.66	α	0	0	0	2	0
	−0.66	α	0	0	0	0	2
$1^2\Sigma^+$	0.66	α	0	0	0	2	0
	0.66	α	0	0	0	0	2
$1^4\Phi^b$	0.68	α	0	0	α	0	α
	0.68	α	0	α	0	α	0
$1^4\Pi^b$	0.66	α	0	0	α	0	α
	−0.66	α	0	α	0	α	0
$1^2\Pi^b$	0.40	2	0	α	0	0	0
	−0.35	α	0	0	β	0	α
	0.35	α	0	0	α	0	β
	−0.35	α	0	α	0	β	0
	0.35	α	0	β	0	α	0
$2^4\Pi^b$	0.95	0	0	α	0	α	α
$1^2\Phi^b$	0.47	β	0	0	α	0	α
	0.47	β	0	α	0	α	0
	−0.34	α	0	0	β	0	α
	−0.34	α	0	β	0	α	0
$2^2\Delta^a$	0.72	0	0	0	0	α	2
$2^2\Pi^b$	0.36	β	0	0	α	0	α
	−0.36	β	0	α	0	α	0
	0.45	α	0	0	β	0	α
	−0.45	α	0	β	0	α	0
$1^4\Delta^a$	0.94	α	α	0	0	α	0
$2^2\Phi^b$	0.52	α	0	β	0	α	0
	0.52	α	0	α	0	β	0
	−0.34	α	0	0	β	0	α
	−0.34	α	0	0	α	0	β
$2^4\Sigma^-$	0.95	α	0	α	0	α	α
$3^3\Pi^b$	0.52	2	0	α	0	0	0
	0.26	α	0	0	β	0	α
	−0.26	α	0	β	0	α	0
	−0.34	0	0	α	0	2	0
	−0.34	0	0	α	0	0	2
1^2H^b	0.48	0	0	0	α	α	β
	−0.48	0	0	0	α	β	α
	0.48	0	0	α	0	2	0
	−0.48	0	0	α	0	0	2
$2^4\Delta^a$	0.96	2	0	α	α	0	α

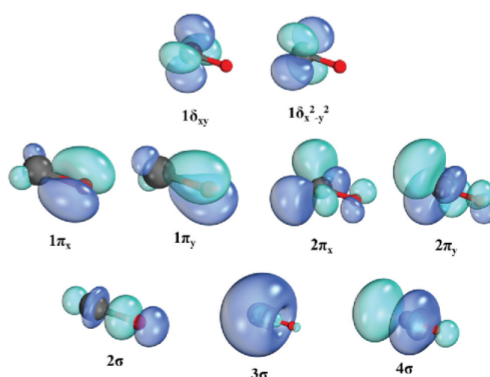^{a} Only the A_1 component is listed. ^{b} Only the B_1 component is listed.

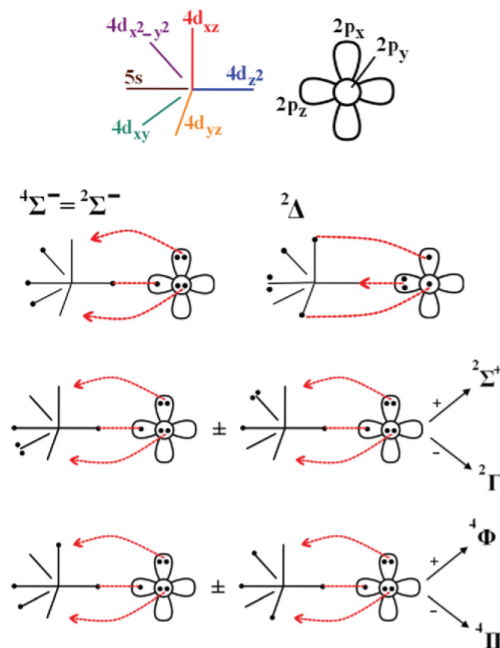**Fig. 1** Valence molecular orbitals for NbO at equilibrium.

123

Fig. 2   Valence bond Lewis diagrams for the first seven states of NbO.

The next higher energy states are the $1^4\Phi$, $1^4\Pi$, $1^2\Pi$, and $1^2\Phi$ states of primary $3\sigma^2 2\pi^1 1\delta^1$ nature. It should be noted that the $1^2\Pi$ state is highly multireference and has significant contribution from the $3\sigma^2 2\pi^1$ configuration. As a result, this state involves both *in situ* Nb($5s^1$) and Nb($5s^2$) characters. The configurations for $2^2\Pi$, $2^2\Phi$, and $3^2\Pi$ are similar to their lower energy counterparts, but with different combinations of sign.

Finally, three states have an unoccupied 3σ orbital, the single reference $2^4\Pi$, $2^2\Delta$, and $2^4\Sigma^-$ states. The three symmetry determining electrons occupy the 4σ, 2π, and 1δ orbitals (see Table 1). All of the orbitals are of high metallic character suggesting a clear *in situ* Nb^{2+} center. These three states are expected to have large dipole moments.

The chemical bonding and electronic structure of the low-lying electronic states of NbO share large similarities with its first-row transition metal oxide analogue VO. Specifically, they both have the same $^4\Sigma^-$ ground state with a $\sigma^1\delta^2$ configuration.[12] In addition, the first eight excited states of NbO and VO have the exact same electronic terms and bonding patterns, but differ in energy order. The nearly identical electronic structure of the two metal oxides can be connected to the very similar electronic structure of the two metals. The two lowest energy states of Nb and V of s^1d^4 and s^2d^3 character are within 2000 cm^{-1}. The s^1d^4 state corresponds to the ground state of Nb but the first excited state for V. The d^4 and s^1d^3 states of the corresponding cations Nb$^+$ and V$^+$ are separated by about 3000 cm^{-1}, the former state being the ground state in both cations. The nearly identical

electronic structure of the two neutral and ionic metals results in the very similar electronic structure of the produced oxides.

Table 2 lists our calculated spectroscopic constants for the states described above at the MRCI, MRCI+Q, CCSD(T), and C-CCSD(T) levels when appropriate. The Nb–O distance for the ground state is 1.696 Å and changes by only 0.002 Å going to MRCI+Q and CCSD(T) levels. Adding core-correlation, the bond length reduces by 0.015 Å at the coupled cluster level. The same difference for VO is 0.01 Å.[12] Our most accurate C-CCSD(T) value for NbO is 1.683 Å and is in very good agreement with the experimental value of 1.690 Å.[14] The harmonic vibrational frequency ranges from 972 (MRCI+Q) to 999 (C-CCSD(T)) cm^{-1}. The experimental value of 989.0 cm^{-1} is in the middle of this range and closer to the more accurate C-CCSD(T) value. The anharmonicity constants $\omega_e x_e$ are also in harmony with the experimental value of 3.83 cm^{-1}.

The first excited state ($1^2\Delta$) is experimentally 4025.6 cm^{-1} above the ground state with an equilibrium bond length of 1.6721 Å and a frequency of 1015.2 cm^{-1}.[19] Our MRCI values for T_e, r_e, and ω_e are 4765 cm^{-1}, 1.682 Å, and 1000 cm^{-1}, respectively. MRCI+Q and CCSD(T) elongate the bond only slightly to 1.686 Å, and the C-CCSD(T) result of 1.671 Å is in remarkable agreement with the experiment. As in the ground state, the core correlation shortens the bond by 0.015 Å. MRCI+Q reduces the excitation energy by $\sim$400 cm^{-1} pushing it towards the experimental value and CCSD(T) moves it even closer to experiment. The core correlation seems to increase the excitation energy moving it away from experiment. Finally, our CCSD(T) and C-CCSD(T) frequencies are 1012 and 1033 cm^{-1}, both of which are in good agreement with experiment.

The same numerical trends are observed for higher lying electronic states. Specifically, the core correlation shortens the NbO bond by 0.014 $\pm$ 0.001 Å and increases the vibrational frequencies by 20 $\pm$ 10 cm^{-1} (see states $1^2\Gamma$, $1^2\Sigma^+$, $1^2\Sigma^-$, $1^4\Phi$, $1^4\Pi$, and $1^4\Delta$). Additionally, the MRCI and MRCI+Q bond lengths and frequencies differ only by a few milli-Å and by less than 10 cm^{-1} except for $1^2\Pi$, while the excitation energies in the two levels generally agree within 1000 cm^{-1}. The MRCI and MRCI+Q anharmonicities are also in good agreement, and for all states we report $\Delta G_{1/2}$ alongside $\omega_e x_e$ values. A last comment relates to the CCSD(T) calculations of the $1^2\Gamma$ and $1^4\Phi$ states. The wave functions of these two states include two major electronic configurations with equal weights (see Table 1). Despite the fact that the reference Hartree–Fock Slater determinant corresponds only to one of these electronic configurations, the CCSD(T) calculation was able to recover the contribution of the second one and provide results comparable to MRCI(+Q); see Table 2.

The most comprehensive spectroscopic study is that of Launila *et al.* published in 1997.[19] The authors summarize the existing experimental data, which include four quartet and six doublet states. They also performed configuration interaction calculations which compare favorably with ours. Our excitation energies for $1^2\Sigma^-$, $1^2\Pi$, and $2^4\Pi$ (see Table 2) are in remarkable agreement (within 300 cm^{-1}) with the experimental values of ref. 19 and 22. The discrepancy between theory and experiment becomes larger upon going to higher excited

This journal is © the Owner Societies 2019

Phys. Chem. Chem. Phys., 2019, **21**, 26324–26332 | **26327**

124

Table 2 Equilibrium energy E_e (a.u.), bond length r_e (Å), harmonic vibrational frequency ω_e (cm^{-1}), anharmonicity $\omega_e x_e$ (cm^{-1}), $\Delta G_{1/2}$ (cm^{-1}), excitation energy T_e (cm^{-1}), and dipole moments μ (D) for the lowest electronic states of ^{41}Nb^{16}O

State	Method	$-E_e$	r_e	ω_e	$\omega_e x_e$	$\Delta G_{1/2}$	T_e	μ^a
X$^4\Sigma^-$	MRCI	131.478795	1.696	976	3.8	968	0	3.78 (3.72)
	MRCI+Q	131.496502	1.697	972	3.6	965	0	3.81
	CCSD(T)	131.497082	1.698	980	3.4	974	0	3.58
	C-CCSD(T)	131.884164	1.683	999	3.5	992	0	3.58
	Expt^b		1.690	989	3.83			
1$^2\Delta$	MRCI	131.457083	1.682	1000		1009	4765	2.10 (2.07)
	MRCI+Q	131.476687	1.686	983		988	4349	2.29
	CCSD(T)	131.477758	1.686	1012	3.7	1004	4241	1.87
	C-CCSD(T)	131.862652	1.671	1033	3.7	1025	4721	1.91
	Expt^c		1.6721	1015.2	3.896		4025	
1$^2\Sigma^-$	MRCI	131.446935	1.689	982		981	6993	1.68 (1.26)
	MRCI+Q	131.465368	1.690	975		974	6833	1.96
	Expt^c		1.6766	993			6747	
1$^2\Gamma$	MRCI	131.443514	1.687	996	2.5	991	7743	3.51 (2.53)
	MRCI+Q	131.461547	1.689	988	1.6	984	7672	3.17
	CCSD(T)	131.461936	1.693	991	3.4	984	7714	2.98
	C-CCSD(T)	131.846749	1.678	1011	3.5	1004	8211	3.03
1$^2\Sigma^+$	MRCI	131.438554	1.691	972		973	8832	2.89 (2.23)
	MRCI+Q	131.457652	1.693	975	0.2	970	8526	3.06
1$^4\Phi$	MRCI	131.436862	1.729	915	4.1	909	9203	3.00 (2.85)
	MRCI+Q	131.453572	1.731	910	4.0	904	9422	2.99
	CCSD(T)	131.450829	1.732	912	2.4	909	10 151	2.79
	C-CCSD(T)	131.834801	1.719	924	3.1	918	10 834	2.86
1$^4\Pi$	MRCI	131.426558	1.731	891	4.1	884	11 465	2.86 (2.75)
	MRCI+Q	131.443888	1.732	892	4.1	885	11 547	2.84
1$^2\Pi$	MRCI	131.413419	1.712	967	8.5	959	14 348	2.70 (3.03)
	MRCI+Q	131.433644	1.720	938	6.0	932	13 796	2.72
	Expt^c		1.7181	901	4.166		13 458	
2$^4\Pi$	MRCI	131.408919	1.741	873	3.9	865	15 336	4.79 (5.08)
	MRCI+Q	131.428140	1.742	873	4.2	865	15 004	4.66
	Expt^d		1.7259			913 ± 34	15 139 ± 276	
1$^2\Phi$	MRCI	131.397561	1.759	941	11.4	923	17 829	4.17 (3.70)
	MRCI+Q	131.418498	1.751	951	9.6	930	17 120	3.93
2$^2\Delta$	MRCI	131.394367	1.701	917		905	18 530	
	MRCI+Q	131.418117	1.703	933		915	17 203	
	Expt^c		1.700	922	2.2		15 875	
2$^2\Pi$	MRCI	131.393782	1.725	910	5.2	900	18 658	2.38 (2.79)
	MRCI+Q	131.415365	1.732	903	5.0	896	17 807	2.52
1$^4\Delta$	MRCI	131.393110	1.762	857	4.1	849	18 806	0.18 (−0.05)
	MRCI+Q	131.410227	1.763	857	4.0	849	18 935	0.17
	CCSD(T)	131.412042	1.761	841		868	18 664	
	C-CCSD(T)	131.794204	1.746	869		878	19 744	
2$^2\Phi$	MRCI	131.385542	1.708	999	9.5	983	20 467	1.40 (2.18)
	MRCI+Q	131.406251	1.709	943	4.7	930	19 808	1.48
	Expt^c		1.732	900	3.6		16 737	
2$^4\Sigma^-$	MRCI	131.384408	1.764	830	3.3	823	20 716	1.91 (2.39)
	MRCI+Q	131.402863	1.766	832	3.3	825	20 551	1.72
	Expt^b		1.7572	850.5	3.37		21 835.3	
3$^2\Pi$	MRCI	131.378634	1.758	917	7.6	906	21 983	4.05 (3.62)
	MRCI+Q	131.401541	1.750	929	7.1	902	20 842	3.76
	Expt^c		1.720	893	3.0		17 698	
1^{2}H	MRCI	131.378404	1.712	890	5.2	889	22 033	4.18 (4.79)
	MRCI+Q	131.399204	1.726	892	5.3	891	21 354	4.09
2$^4\Delta$	MRCI	131.362792	1.786	822	2.9	816	25 460	3.86 (4.01)
	MRCI+Q	131.381554	1.788	813	3.1	807	25 228	3.78

^{a} μ_{FF} values and expected values (in parentheses). ^{b} Ref. 14; collection from different sources. ^{c} Ref. 19; electronic spectroscopy. ^{d} Ref. 22; laser excitation spectroscopy. The range reported for the $\Delta G_{1/2}$ and T_e values covers the values given by the authors of ref. 22 for the four spin–orbit components of the B$^4\Pi$ state. The listed T_e value corresponds to experimental T_0.

states, and especially the heavily multi-reference doublet states. For example, the difference in excitation energy for 2$^4\Sigma$ is ~800 cm^{-1} and for 2$^2\Delta$, 2$^2\Phi$, and 3$^2\Pi$ is ~1500, ~3000 and ~3000 cm^{-1}, respectively. The only other high-level theoretical work of Langhoff and Bauschlicher reports CASSCF, MRCI, and MCPF results only for the first four electronic states of quartet spin multiplicity.[16]

Finally, the potential energy curves (PECs) of the quartet and doublet states are shown in Fig. 3 and 4. The zero of both plots is set to the equilibrium energy of the ground state. The quartet PECs are smooth and well separated from each other. Only the last $^4\Delta$ state suffers from an avoided crossing at 2.1 Å. On the other hand, the doublet PECs are quite dense especially in the energy region of ~60 kcal mol^{-1}. The PEC of 2$^2\Delta$ becomes
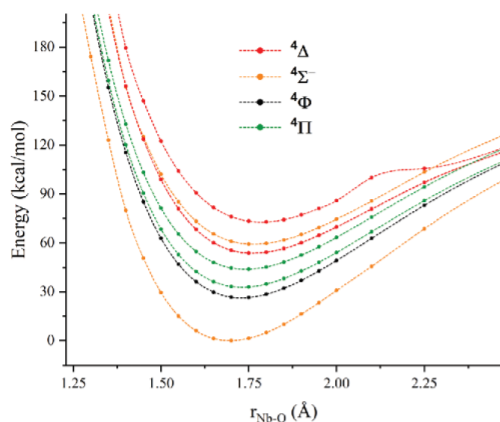
125

Fig. 3 MRCI PECs of the quartet states of NbO with respect to Nb–O distance.
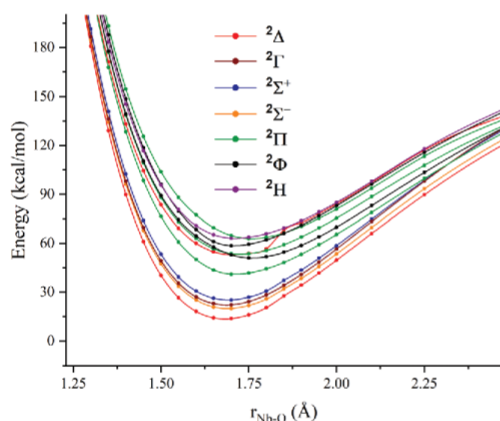

Fig. 4 MRCI PECs of the doublet states of NbO with respect to Nb–O distance.

discontinuous at 1.8 Å possibly because of some avoided crossing with a higher state, while the two $^2\Phi$ states undergo an avoided crossing at 1.6 Å.

Our spin–orbit calculations were able to capture the second order splitting of the ground $X^4\Sigma^-$ state. Our MRCI value of 57 cm^{-1} is in very good agreement with the experimental value of 62 cm^{-1}, which can explain the little relation of the gas phase emission spectrum with the low-temperature matrix absorption spectrum.[15] Our $^2\Delta_{3/2}$–$^2\Delta_{5/2}$ splitting of 947 cm^{-1} is also in very good agreement with the 940 cm^{-1} experimental value, in contrast with the $^2\Pi_{1/2}$–$^2\Pi_{3/2}$ splitting which is predicted to be considerably smaller compared to experiment (606 vs. 782 cm^{-1}).[19] The energy gap between successive $2^4\Pi_\Omega$ ($\Omega = -1/2, 1/2, 3/2, 5/2$) components is theoretically (experimentally; $\nu = 0$)[22] 234 (265), 181 (250), and 148 (36) cm^{-1}. The same values for $1^4\Pi$ are theoretically

80, 96, and 121 cm^{-1}, and the $1^2\Gamma_{7/2}$–$1^2\Gamma_{9/2}$ splitting is 48 cm^{-1}, but no experimental results are available for these two states. We are not aware of any other theoretical work on spin–orbit effects.

The binding energy of $X^4\Sigma^-$ increases with the level of theory and is 174.9, 176.4, 178.7, and 179.9 kcal mol^{-1} at the MRCI, MRCI+Q, CCSD(T), and C-CCSD(T) levels respectively. ZPE-corrected binding energies (D_0) were found to be 173.5, 175.0, 177.3, and 178.4 kcal mol^{-1} for the same methodologies. The highest level C-CCSD(T) value of 178.4 kcal mol^{-1} is about 2 kcal mol^{-1} higher than the upper bound of experiment (173.6 ± 2.5 kcal mol^{-1}).[21] After considering spin–orbit (SO) effects of both the Nb(^{6}D) + O(^{3}P) fragments and the $X^4\Sigma^-$ ground state the C-CCSD(T) SO-corrected binding energy becomes: $D_0^{\text{SO-corrected}} = D_0 + SO_{\text{corr}}(\text{NbO}; X^4\Sigma^-) - [SO_{\text{corr}}(\text{Nb}; {}^6\text{D}) + SO_{\text{corr}}(\text{O}; {}^3\text{P})] = D_0 + 62.1$ cm^{-1} − (634.4 + 78.0) cm^{-1} = 178.4 − 1.86 kcal mol^{-1} = 176.5 kcal mol^{-1}, which is just 0.4 kcal mol^{-1} greater than the experimental upper limit. The SO_{corr} values for the atoms are obtained as the energy difference between the experimental M_J average and the lower energy J-state of Nb(^{6}D) and O(^{3}P), and for NbO as the difference between the MRCI energies before and after spin–orbit effects.

Dipole moments calculated both as expectation values and as first derivatives with respect to an external electric field are listed in Table 2. Generally, the values range from about 2 to about 5 Debye except for the $1^4\Delta$ state, which has a practically zero dipole moment. As expected (see above), the dipole moment of the $1^2\Delta$ and $2^4\Pi$ states lies at the lower and the upper end of the 2–5 D range, respectively. The $1^4\Delta$ state is the only one with one electron in both 3σ and 4σ orbitals, which are both localized on the metal, and this may be the reason for its small dipole moment.

Finally, we identified the ground state of NbO$^+$ and NbO$^-$ as $^3\Sigma^-$ with the departing or added electron either leaving from or going to 3σ. The ESI† includes potential energy curves for the lowest seven states of NbO$^-$. The ionization energy of NbO is 7.01 and 7.17 eV at the CCSD(T) and C-CCSD(T) levels, respectively. The latter value is in perfect agreement with the experimental value of Loock et al. (7.154 ± 0.001 eV).[21] The same levels provide an electron affinity of 0.59 and 0.65 eV, which is in poor agreement with the experimental value of 1.29 eV.[38] After adding a series of diffuse functions on the metal center these values double to 1.24 and 1.21 eV, now in very good agreement with experiment.

IIIB. NbO + CH$_4$

In this section we investigate the reaction of NbO with methane focusing on the activation of a C–H bond to form CH$_3$NbOH and the subsequent release of methanol. The reaction of NbO$^{0,+,2+}$ and NbO$_2^{0,+,2+}$ with methane has been investigated experimentally and theoretically for the ground state only.[39–41] Here, we investigate the pathways related to both the ground and lowest excited electronic states going beyond the first intermediate CH$_3$NbOH structure. Initially, we located all intermediates and transition states for the lowest quartet and doublet states at the DFT/MN15 level. For the first reaction step, we constructed the potential energy profiles (PEPs) along the intrinsic reaction coordinate (IRC) to identify possible
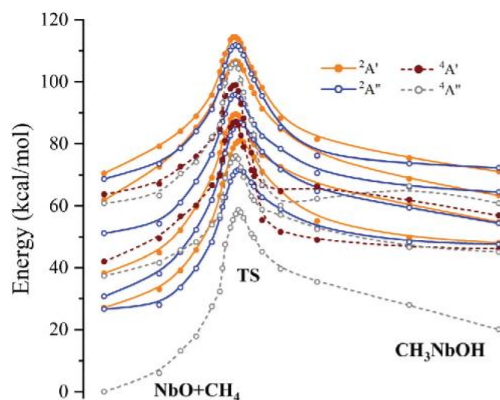
This journal is © the Owner Societies 2019

Phys. Chem. Chem. Phys., 2019, 21, 26324–26332 | 26329

126

Fig. 5 CASSCF PEPs for the lowest lying electronic states of the NbO + CH$_4$ reaction pathway.

crossings between them. All intermediate structures for the IRC calculation were optimized with MN15, and single point energy calculations were done for the lowest and some excited states at the CASSCF level for each spin multiplicity separately.

The PEPs for the first step are shown in Fig. 5. The ground state PEP (lowest energy $^4A''$ pertaining to $^4\Sigma^-$) is well separated from the rest of the states and the character of the singly occupied molecular orbitals centered on Nb does not change along the reaction. Specifically, the 3σ and 1δ orbitals of NbO convert to σ_{Nb} and δ_{Nb} orbitals of CH$_3$NbOH (compare Fig. 1 and 6). The σ_{Nb} orbital retains its 5s nature but it is further polarized away not only from the NbO bond but also from the NbC bond. The δ_{Nb} orbitals remain pure d_{xy} and $d_{x^2-y^2}$ atomic orbitals of Nb. The Nb–O bonding orbitals 2σ and 1π remain doubly occupied and polarized towards oxygen. The $1\pi_y$ adopts the a'' irreducible representation and stays largely unaffected by

the reaction with CH$_4$ (orbital $\pi_{y,NbO}$), but the $1\pi_x$ and 2σ orbitals both become a' orbitals and are mixed with each other (see orbitals $\sigma_{NbO} + \sigma_{OH}$ and $\pi_{x,NbO} + \sigma_{NbO}$ of Fig. 6). Overall, the electronic structure of the metal–oxygen moiety keeps its character before and after the formation of the O–H and Nb–C bonds. The hydrogen atom is attached as a proton to the oxygen terminal replacing the $2s^2$ electron pair present in the original NbO molecule with a σ_{OH}^2 pair, while the CH$_3$ unit attaches as CH$_3^-$ to the metal, forming the chemical bond represented by the orbital σ_{NbC} of Fig. 6. The Mulliken charges on carbon (-1.0) and on the hydrogen atom of OH ($+0.2$) agree with this picture. The situation for the excited states is identical. Finally, the 2π orbitals populated in the Π and Φ states split into a' and a'' orbitals under the C_s symmetry of CH$_3$NbOH. As in the 1π case, the $2\pi_y$ (a'') orbital is minimally affected, while $2\pi_x$ (a') blends with the $\sigma^*(NbC)$ molecular orbital (see orbitals $\pi_{y,NbO}^*$ and $\pi_{x,NbO}^* + \sigma_{NbC}^*$ of Fig. 6).

As shown in Fig. 5, the reaction of methane with the first excited state of NbO, $^2\Delta$, separates into two components ($3\sigma^2 1\delta_{xy}$ and $3\sigma^2 1\delta_{x^2-y^2}$) along the reaction coordinate (lowest energy $^2A'$ and $^2A''$ PEPs), which converge to the same energy at the end of the reaction with the same $3\sigma^2 1\delta^1$ character. The next excited state, $^2\Sigma^-$, also retains its $3\sigma^1 1\delta^2$ character along the reaction, and the same is true for the rest of the studied doublet states. On the other hand, the quartet states undergo some avoided crossings. Specifically, both the $^4A''$ and $^4A'$ components of $^4\Phi$ and $^4\Pi$ nearly cross in the region just after the transition state and exchange their $3\sigma^1 1\delta^1 2\pi^1$ electronic configurations.

Conclusively, the reaction of the lowest energy states of NbO with CH$_4$ proceeds *via* a [2+2] oxidative addition mechanism, where one C–H bond cleaves heterolytically. One proton attaches to oxygen and one methyl anion attaches to niobium. The alternative radical mechanism is not observed currently because of the strong Nb^{2+}O^{2-} character of the Nb–O bond as dictated by the $2\sigma^2 1\pi^4$ electronic configuration and the
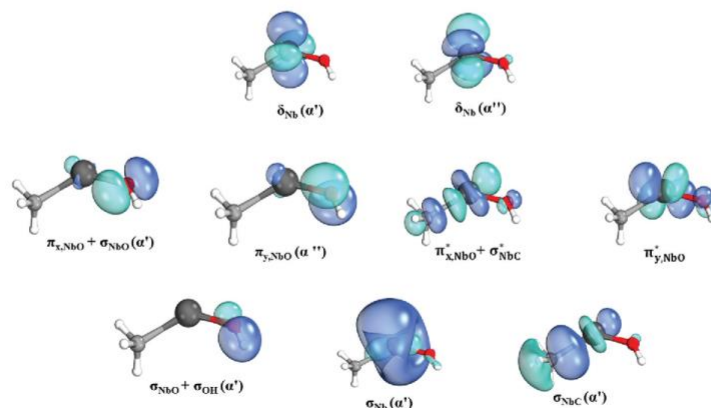
Fig. 6 Valence molecular orbitals for the CH$_3$NbOH complex at equilibrium.

26330 | *Phys. Chem. Chem. Phys.*, 2019, **21**, 26324–26332

This journal is © the Owner Societies 2019

127

Fig. 7 CCSD(T) complete energy diagram for the reaction of NbO with CH$_4$ (R) to produce Nb and CH$_3$OH (P) for the lowest energy doublet, quartet, and sextet states.

polarization of the 2σ and 1π orbitals towards oxygen. To investigate the possibility of a radical mechanism, we probed the reaction of CH$_4$ with the lowest energy sextet state. According to our calculations, the sextet state has a Nb^{3+}O$^{\bullet}$ character, which can initiate the radical mechanism.[28,42] Specifically, the lowest sextet state can be generated from the ground state by promoting one 1π$_x$ electron to a 2π$_x$ orbital, which represents an electron transfer from oxygen to niobium (see Fig. 1).
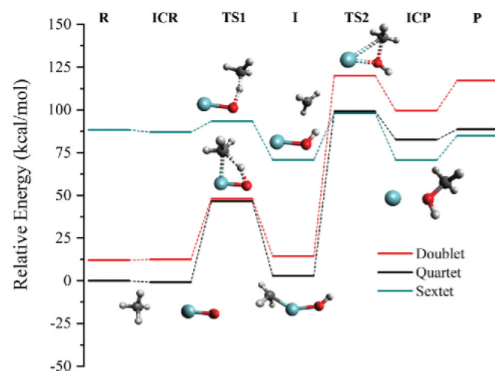
Our CCSD(T) complete energy diagram for the reaction of NbO with CH$_4$ to produce Nb and CH$_3$OH for the lowest energy doublet, quartet, and sextet states is given in Fig. 7. The MN15 and CCSD(T) diagrams are compared in the ESI.† The two diagrams are in very good agreement with the exception that MN15 overestimates the interaction energy of NbO + CH$_4$ (ICR) and Nb + CH$_3$OH (ICP) in comparison with CCSD(T). The TS2 structures have T1 diagnostics (see the ESI†) bigger than the 0.045 threshold proposed in the literature as the limit for single reference character of 4d-transition metal compounds.[43] However, we consider that our values are quite accurate based on our recent results, where CCSD(T) values provided accurate energetics with T1 diagnostics as large as 0.09.[35] The smallest coefficient of the CI vector (CASSCF level) for TS2 is 0.93 (see the ESI†). On the other hand, the lowest doublet state of Nb(^{2}G; 5s^{2}4d^3) is naturally multi-reference (the largest two CI coefficients are 0.59 and −0.56; see the ESI†), but the CCSD(T) calculation predicts a small T1 value of 0.024. Despite their small T1 values, our ICP and Nb + CH$_3$OH energies for the doublet state should not be considered as accurate. Specifically, the CCSD(T) Nb(^{6}D) ← Nb(^{2}G) excitation energy is predicted as 11 305 cm^{-1} vs. the experimental value of 8471 cm^{-1} (M_J-averaged).[37] Our results question the validity of the use of T1 as an indicator of multi-reference character.

The corresponding structures and frequencies are provided in the ESI.† For the doublet and quartet states, NbO reacts first with CH$_4$ to produce the intermediate CH$_3$NbOH structure, as discussed above. On the other hand, the sextet indeed follows a radical mechanism and the formed intermediate structure is a

methyl radical interacting with NbOH (see Fig. 7 and the ESI†). Overall, the energy landscape for the sextet state is slightly exothermic and characterized by small activation energy barriers. In contrast, the reactants of quartet and doublet spin multiplicity are lower in energy and have to overcome prohibitive activation energy barriers of about 100 kcal mol^{-1}. It should be noted that the lowest energy state of the Nb + CH$_3$OH products is a sextet. Therefore, one possible way to perform this reaction is by photochemically accessing the sextet state of NbO. The reaction is rather spontaneous on the sextet potential energy surface. Another way to efficiently perform this reaction would be to stabilize the sextet state of the NbO unit by attaching suitable ligands to niobium. We drew similar conclusions for the FeO^{2+} unit, where weak field ligands are necessary to improve its efficiency of C–H activation.[28]

IV. Summary and conclusions

High level electronic structure calculations were performed to study several low-lying electronic states of NbO. This is the first systematic high level electronic structure investigation of NbO. We report bond lengths, harmonic vibrational frequencies, anharmonicities, excitation energies, binding energies, bonding patterns, and dipole moments for all states. In addition, the ionization energy and electron affinity for the ground state are reported and they are both in very good agreement with experiment. The ground states were found to be $^4\Sigma^-$ for NbO and $^3\Sigma^-$ for both NbO$^-$ and NbO$^+$. Spin–orbit effects were also included for many low-lying states and our calculations predict a quite accurate second order spin–orbit splitting for the ground $^4\Sigma^-$ state. Coupled cluster calculations were completed for many states both with and without the core-correlation. Generally, the CCSD(T) results compare better with experiment than MRCI and MRCI+Q. The sub-valence electron correlation was found to be essential for reproducing the experimental bond lengths and spectroscopic constants. Our calculations provide a complete set of data for all low-lying electronic states of NbO and identified some states, such as 1$^2\Gamma$ and 1$^2\Sigma^+$, which are not yet experimentally detected. Finally, binding schemes are proposed based on the molecular orbitals and CI expansion of the wave functions.

Next, we studied the reaction of NbO with CH$_4$ for the lowest thirteen channels. All of them are characterized by Nb^{2+}O^{2-} nature which facilitates the [2+2] (oxidative addition) mechanism leading to the CH$_3$–Nb^{2+}OH intermediate. Finally, the methyl group recombines with hydroxyl to make methanol. The reaction is highly endothermic and large activation energy barriers have to be overcome. We also explored the lowest energy reaction path of sextet multiplicity, which leads to the ground state Nb + CH$_3$OH products. We found that the reaction is slightly exothermic in this case and only small activation energy barriers are present. The reason for the different energy landscape is ascribed to the radical mechanism followed along the sextet reaction path. Therefore, the reaction can be achieved by photochemically accessing the sextet pathway.

This journal is © the Owner Societies 2019

Phys. Chem. Chem. Phys., 2019, 21, 26324–26332 | 26331

128

Conflicts of interest

There are no conflicts to declare.

Acknowledgements

References

1 K. Kim, S.-G. Woo, Y. N. Jo, J. Lee and J.-H. Kim, *Electrochim. Acta*, 2017, **240**, 316.

2 C. Nico, T. Monteiro and M. P. F. Graça, *Prog. Mater. Sci.*, 2016, **80**, 1.

3 F. Nakagomi, S. E. Cerruti, M. R. de Freitas, E. S. Freitas Neto, F. V. de Andrade and G. O. Siqueira, *Chem. Phys. Lett.*, 2019, **729**, 37.

4 N. P. de Moraes, F. N. Silva, M. L. C. P. da Silva, T. M. B. Campos, G. P. Thim and L. A. Rodrigues, *Mater. Chem. Phys.*, 2018, **214**, 95.

5 N. Prado and L. C. A. Oliveira, *Appl. Catal., B*, 2016, **205**, 481.

6 K. Tanabe, *Catal. Today*, 1990, **8**, 1.

7 K. Tanabe and S. Okazaki, *Appl. Catal., A*, 1995, **133**, 191.

8 A. Sauval, *Astron. Astrophys.*, 1977, **62**, 295.

9 D. N. Davis and P. C. Keenan, *Publ. Astron. Soc. Pac.*, 1969, **81**, 230.

10 T. Tsuji, *Annu. Rev. Astron. Astrophys.*, 1986, **24**, 89.

11 N. M. White and R. F. Wing, *Astrophys. J.*, 1978, **222**, 209.

12 E. Miliordos and A. Mavridis, *J. Phys. Chem. A*, 2007, **111**, 1953.

13 J. M. Dyke, A. M. Ellis, M. Fehèr, A. Morris, A. J. Paul and J. C. H. Stevens, *J. Chem. Soc., Faraday Trans. 2*, 1987, **83**, 1555.

14 K. P. Huber and G. Herzberg, *Molecular Spectra and Molecular Structure*, 1979.

15 A. J. Merer, U. Sassenberg, J. L. Féménias and G. Cheval, *J. Chem. Phys.*, 1987, **86**, 1219.

16 S. R. Langhoff and C. W. Bauschlicher, *J. Chem. Phys.*, 1988, **89**, 2160.

17 P. E. M. Siegbahn, *Chem. Phys. Lett.*, 1993, **201**, 15.

18 M. Dolg, H. Stoll, H. Preuss and R. M. Pitzer, *J. Phys. Chem.*, 1993, **97**, 5852.

19 O. Launila, B. Schimmelpfennig, H. Fagerli, O. Gropen, A. G. Taklif and U. Wahlgren, *J. Mol. Spectrosc.*, 1997, **186**, 131.

20 M. Zhou and L. Andrews, *J. Phys. Chem. A*, 1998, **102**, 8251.

21 H.-P. Loock, B. Simard, S. Wallin and C. Linton, *J. Chem. Phys.*, 1998, **109**, 8980.

22 C. T. Kingston, C. K. D. Liao, A. J. Merer and S. J. Tang, *J. Mol. Spectrosc.*, 2001, **207**, 104.

23 B. Kharat, S. B. Deshmukh and A. Chaudhari, *Int. J. Quantum Chem.*, 2009, **109**, 1103.

24 N. M. S. Almeida, I. R. Ariyarathna and E. Miliordos, *Phys. Chem. Chem. Phys.*, 2018, **20**, 14578.

25 I. R. Ariyarathna and E. Miliordos, *Phys. Chem. Chem. Phys.*, 2018, **20**, 12278.

26 E. Miliordos and A. Mavridis, *J. Phys. Chem. A*, 2010, **114**, 8536.

27 C. N. Sakellaris, E. Miliordos and A. Mavridis, *J. Chem. Phys.*, 2011, **134**, 234308.

28 J. K. Kirkland, S. N. Khan, B. Casale, E. Miliordos and K. D. Vogiatzis, *Phys. Chem. Chem. Phys.*, 2018, **20**, 28786.

29 T. H. Dunning, *J. Chem. Phys.*, 1989, **90**, 1007–1023.

30 R. A. Kendall, T. H. Dunning and R. J. Harrison, *J. Chem. Phys.*, 1992, **96**, 6796.

31 D. E. Woon and T. H. Dunning, *J. Chem. Phys.*, 1993, **98**, 1358.

32 K. A. Peterson, D. Figgen, M. Dolg and H. Stoll, *J. Chem. Phys.*, 2007, **126**, 124101.

33 H.-J. Werner, P. J. Knowles, G. Knizia, F. R. Manby, M. Schütz, P. Celani, W. Györffy, D. Kats, T. Korona, R. Lindh, A. Mitrushenkov, G. Rauhut, K. R. Shamasundar, T. B. Adler, R. D. Amos, A. Bernhardsson, A. Berning, D. L. Cooper, M. J. O. Deegan, A. J. Dobbyn, F. Eckert, E. Goll, C. Hampel, A. Hesselmann and G. Hetzer, *MOLPRO, version 2015.1, a package of ab initio programs*, 2015 see http://www.molpro.net.

34 H. S. Yu, X. He, S. L. Li and D. G. Truhlar, *Chem. Sci.*, 2016, **7**, 5032.

35 S. N. Khan and E. Miliordos, *J. Phys. Chem. A*, 2019, **123**, 5590.

36 M. J. Frisch, G. W. Trucks, H. B. Schlegel, G. E. Scuseria, M. A. Robb, J. R. Cheeseman, G. Scalmani, V. Barone, G. A. Petersson, H. Nakatsuji, X. Li, M. Caricato, A. V. Marenich, J. Bloino, B. G. Janesko, R. Gomperts, B. Mennucci, H. P. Hratchian, J. V. Ortiz, A. F. Izmaylov, J. L. Sonnenberg, D. Williams-Young, F. Ding, F. Lipparini, F. Egidi, J. Goings, B. Peng, A. Petrone, T. Henderson, D. Ranasinghe, V. G. Zakrzewski, J. Gao, N. Rega, G. Zheng, W. Liang, M. Hada, M. Ehara, K. Toyota, R. Fukuda, J. Hasegawa, M. Ishida, T. Nakajima, Y. Honda, O. Kitao, H. Nakai, T. Vreven, K. Throssell, J. J. A. Montgomery, J. E. Peralta, F. Ogliaro, M. J. Bearpark, J. J. Heyd, E. N. Brothers, K. N. Kudin, V. N. Staroverov, T. A. Keith, R. Kobayashi, J. Normand, K. Raghavachari, A. P. Rendell, J. C. Burant, S. S. Iyengar, J. Tomasi, M. Cossi, J. M. Millam, M. Klene, C. Adamo, R. Cammi, J. W. Ochterski, R. L. Martin, K. Morokuma, O. Farkas, J. B. Foresman and D. J. Fox, *Gaussian 16, Revision B.01*, Gaussian, Inc., Wallingford CT, 2016.

37 A. Kramida, Y. Ralchenko and J. Reader, NIST ASD Team (2019). NIST Atomic Spectra Database (version 5.7.1), [Online], Available: https://physics.nist.gov/asd, Fri Nov 01 2019, National Institute of Standards and Technology, Gaithersburg, MD, DOI: 10.18434/T4W30F.

38 D. R. Lide, *CRC Handbook of Chemistry and Physics*, CRC Press, New York, 93rd edn, 2012.

39 G. Wang, S. Lai, M. Chen and M. Zhou, *J. Phys. Chem. A*, 2005, **109**, 9514.

40 K. J. de Almeida, T. C. Silva, J. L. Neto, M. V. J. Rocha, T. C. Ramalho, M. N. de Miranda and H. A. Duarte, *J. Organomet. Chem.*, 2016, **802**, 49.

41 Y. Cao, X. Zhao, B. Xin, S. Xiong and Z. Tang, *THEOCHEM*, 2004, **683**, 141.

42 M. Schlangen and H. Schwarz, *Dalton Trans.*, 2009, 10155.

43 J. Wang, S. Manivasagam and A. K. Wilson, *J. Chem. Theory Comput.*, 2015, **11**, 5865.

129

Appendix B: Supporting Material for Chapter 4

Appendix B contains a full copy of the following article

E. E. Claveau and **E. Miliordos**, *Physical Chemistry Chemical Physics* <u>23</u>, 21172 (2021)

ROYAL SOCIETY
OF CHEMISTRY

Check for updates

Electronic structure of the dicationic first row transition metal oxides†

Emily E. Claveau [ID] and Evangelos Miliordos [ID] *

Multi-reference electronic structure calculations combined with large basis sets are performed to investigate the electronic structure of the ground and low-lying electronic states of the MO^{2+} diatomic species with M = Ti–Cu. These systems have shown high efficiency in the activation of the C–H of saturated hydrocarbons. This study is the first systematic and accurate work for these systems and our results and discussion provides insights into the reactivity and stability of MO^{2+} units. We find that they can be divided in three groups. The early transition metals (Ti, V, Cr) have very stable and well separated oxo ($M^{4+}O^{2-}$) character ground states, the middle transition metals (Mn, Fe) have oxyl ($M^{3+}O^{\bullet-}$) ground states with low-lying oxo excited states, and the late transition metals (Co, Ni, Cu) have well separated oxyl states. The reported spectroscopic constants will aid future experimental investigations, which are sparse in the literature. Periodic trends for the bond lengths, energetics, excitation energies, and wavefunction composition are discussed in detail. Complete basis set limit results indicate the high accuracy of the quintuple-ζ basis sets.

I. Introduction

Transition metal complexes with a metal(IV)–oxo (MO^{2+}) unit have been shown to efficiently activate C–H bonds of saturated hydrocarbons.[1–9] The iron oxo unit is the most widely studied because of its presence in intermediate forms of enzymes.[10] Within the first-row transition metals, Ti through Cu oxo complexes have been recently synthesized and their reaction with organic molecules has been assessed.[1–8,11–16] The low cost and higher abundance of the first-row transition metals make them ideal candidates for industrial applications.

To understand the catalytic performance of these transition metal compounds, we first need to understand the electronic structure of MO^{2+}, which will enable a deeper comprehension of the role of the ligand effects[17–23] and the involvement of the excited states in the reaction mechanism.[4] Despite the importance of these units, surprisingly minimal knowledge exists in the literature on the electronic structure of their ground and low-lying electronic states for the bare and ligated MO^{2+} species.[24–29] On the contrary, the study of neutral (MO), cationic (MO^+) and anionic (MO^-) bare metal oxygen units has

been rather complete for several electronic states at high levels of theory.[30–37] To fill this gap in the literature, we recently elucidated the electronic structure of FeO^{2+} and monitored the effect of strong and weak field ligands,[18] and we currently investigate the MO^{2+} ions with M = Ti–Mn, Co–Cu with state-of-the-art quantum chemical methodologies. For reasons of completeness, we refer to our earlier FeO^{2+} results as well.

Compared to the $MO^{0,\pm}$ species, MO^{2+} units may adopt two forms, the usually more stable oxo form ($M^{4+}O^{2-}$) and the oxyl form ($M^{3+}O^{\bullet-}$) which "have nearly one unpaired electron or hole on the oxygen ligand and a metal center in a nearly one-electron-reduced oxidation state".[38] The relative contribution of each configuration to the wavefunction of the complex is sensitive to the nature of the metal and the ligands. Practically, the metals before group 8 (Fe) make oxo complexes and the remaining metals tend to form oxyl structures. The famous oxo-wall placed between Fe and Co is a verbal formulation of this trend.[38] Transition metal oxo complexes follow a proton-coupled electron transfer mechanism to activate a C–H bond, while oxyl complexes are more reactive (lower activation barriers) enabling the hydrogen radical abstraction mechanism.[38]

The interplay between the oxo and oxyl forms render the comprehension of the electronic structure of the MO^{2+} species imperative. Presently, we perform multi-reference calculations to predict their ground and low-lying electronic states, analyze their wavefunctions, present spectroscopic constants and examine their stability. In Section II, we describe the quantum chemical approaches employed in this study. In Section III, we

Department of Chemistry and Biochemistry, Auburn University, Auburn AL 36849-5312, USA. E-mail: emiliord@auburn.edu

discuss each metal separately followed by a summary and comparative review for all metals in Section IV.

II. Computational details

Multi-reference techniques were employed to solve the electronic Schrödinger equation as they are necessary to tackle the complexity of the wavefunction for the systems in question.[4,25] The first order wavefunctions were obtained at the Complete Active Space Self-Consistent Field (CASSCF) level. The active space for all metal oxide dications mentioned in this manuscript included nine orbitals representing the three 2p orbitals of oxygen, the 4s orbital of the metal, and the 3d orbitals of the metal. The 2s orbital and electrons of oxygen were not included in the active space, which is a common practice for cationic, neutral, and anionic metal oxides, because of the minimal contribution of $2s^1$ configurations in the CASSCF wavefunctions leading to swap of the 2s orbital of oxygen with 3p orbitals of the metal. In addition, for MO^{2+} the 4s orbital of the metal is minimally populated at CASSCF and it is exchanged with other orbitals (also minimally populated) of the same symmetry. This situation is expected since the metal is in a 2+, 3+, or 4+ oxidation (*in situ*) state, and none of them populates the 4s orbital. In any case, we decided to include this ninth "4s" orbital to avoid missing electronic states.

Multi-Reference Configuration Interaction (MRCI) was applied on top of the CASSCF wavefunction. Single and double promotions from the active to the virtual space are allowed within the internally contracted scheme.[39–41] The dynamic correlation from the 2s electron of oxygen is now included. A separate set of MRCI calculations (C-MRCI) include the electron correlation of the subvalence $3s^2 3p^6$ electrons of the metal. The Davidson correction (+Q) is also added to remedy the size non-extensivity of MRCI and C-MRCI.[42]

Two series of basis sets were used. Exploratory calculations and full potential energy curves were performed with triple-ζ quality basis sets: cc-pVTZ for the metals[43] and aug-cc-pVTZ for oxygen.[44–46] The diffuse functions on oxygen are necessary to accurately describe the polarized nature of the metal–oxygen bonds. The calculation of the spectroscopic constants and other numerical data are obtained by recalculating the potential energy curves (PECs) around equilibrium with the corresponding quintuple-ζ basis sets (cc-pV5Z and aug-cc-pV5Z). For the C-MRCI calculations the corresponding weighted-core basis set was used for the metal (cc-pwCV5Z).[43]

For the ground state of each species, we also calculated the complete basis set limit (CBS) for the spectroscopic constants. The process involved the extrapolation of the energy for every point of the potential energy curves to the CBS limit. An exponential convergence pattern was assumed:

$$E_n = E_\infty + Ae^{-bn}$$

where E_n is the energy with triple ($n = 3$), quadruple ($n = 4$), or quintuple ($n = 5$) basis sets [cc-pVnZ or cc-pwCVnZ for the metal and aug-ccpVnZ for oxygen]. E_∞ is the CBS limit of the energy

and A, b are constants to be determined. By fitting the E_3, E_4, E_5 values to this expression, the E_∞ value is given by

$$E_\infty = \frac{E_3 E_5 - E_4^2}{E_3 + E_5 - 2E_4}$$

This expression was used separately for the CASSCF reference energy and the electron correlation energy at MRCI or C-MRCI, since the two quantities converge at a different rate (CASSCF energies converge faster). The two CBS limits were finally added to get the overall energy CBS limit. The extrapolated PECs were then used to obtain spectroscopic data. Our values for each of the three basis sets and the CBS limit are listed in the ESI.†

The C_{2v} point-group was always exploited, and the ro-vibrational Schrödinger equation was solved numerically (in-house code) to obtain the rotational and vibrational levels of all states using the most abundant isotopes (see Table 1). The code is available at http://auburn.edu/cosam/faculty/chemistry/miliordos/my_lab/page7.htm. The MOLPRO 2015 suite of codes was invoked for all electronic structure calculations.[47]

III. Results and discussion

The ground and low-lying excited electronic states of the first-row transition metal monoxides, neutral (MO) and cationic (MO$^+$), have been studied meticulously in the literature.[30–37,48,49] In all cases, the oxygen terminal is electron rich and can be characterized as O$^-$ or O^{2-} depending on how someone assigns the polarized σ and π bonds. More importantly, theoretical studies provide evidence that no unpaired electrons exist on oxygen,[30–37,48,49] which is better described by the conventional MO = $M^{2+}O^{2-}$ or MO$^+$ = $M^{3+}O^{2-}$ picture. Going from MO to MO$^+$ the electron detaches from some metallic orbital due to the lower ionization energy of the metal (6.56–7.73 eV *vs.* 13.62 eV for oxygen),[50] and the oxygen remains electron rich. For Sc, Ti, V, Co, Ni, this metallic orbital is the 4s polarized away from oxygen, for Mn, Cu, Zn it is some 3d orbital, while for Cr and Fe the two possibilities are energetically nearly degenerate.[30–37,48,49]

The second electron detachment side from MO$^+$ is not clear. The already positively charged metal requires higher ionization energy, which may now be comparable to that of oxygen. As a result, the ground state electron configuration is expected to be of either $M^{4+}O^{2-}$ (oxo) or $M^{3+}O^{\bullet-}$ (oxyl) character. The latter notation implies an unpaired electron on oxygen. Indeed, our calculations demonstrate that early transition metal oxides prefer the oxo, whereas late transition metals prefer the oxyl form. This is known as the oxo-wall in the literature of inorganic chemistry,[38] and is consequence of the higher ionization energy of late transition metals. In some cases, there is even mixed $M^{4+}O^{2-}$ $\leftrightarrow$ $M^{3+}O^{\bullet-}$ multi-reference nature.

Below we discuss each metal oxide separately and in the summary section we provide a more comparative analysis. Table 1 lists all our numerical results including the CBS values at MRCI and C-MRCI level. The CBS values are in excellent agreement with our quintuple-ζ results (see Summary).

This journal is © the Owner Societies 2021

Phys. Chem. Chem. Phys., 2021, **23**, 21172–21182 | **21173**

Table 1 Equilibrium bond length r_e (Å), harmonic vibrational frequency ω_e (cm^{-1}), anharmonicity $\omega_e x_e$ (cm^{-1}), $\Delta G_{1/2}$ (cm^{-1}) and excitation energy T_e (cm^{-1}) for the lowest electronic states of MO^{2+}, M = Ti–Cu

Table 1 (continued)

State	Method[a]	r_e	ω_e	$\omega_e x_e$	$\Delta G_{1/2}$	T_e
		^{48}Ti^{16}O^{2+}				
$\tilde{X}^1\Sigma^+$	MRCI	1.554	1057	3.2	1055	0
	MRCI/CBS	1.553	1050	3.4	1049	0
	MRCI + Q	1.557	1052	3.3	1049	0
	C-MRCI	1.540	1084	4.9	1076	0
	C-MRCI/CBS	1.539	1078	4.8	1069	0
	C-MRCI + Q	1.545	1084	6.6	1068	0
$^1\Phi$	MRCI	1.804	683	11.6	658	19112
	MRCI + Q	1.803	698	11.3	674	19256
	C-MRCI	1.789	683	10.9	655	19615
	C-MRCI + Q	1.784	717	10.9	692	20057
$^3\Phi$	MRCI	1.790	736	16.4	696	20070
	MRCI + Q	1.791	741	14.6	705	20278
	C-MRCI	1.772	735	15.1	701	20455
	C-MRCI + Q	1.770	755	12.6	724	21005
$^1\Pi$	MRCI	1.804	694	12.2	668	20757
	MRCI + Q	1.803	708	11.3	683	20816
	C-MRCI	1.788	708	11.3	683	21257
	C-MRCI + Q	1.783	729	10.5	703	21522
		^{51}V^{16}O^{2+}				
$\tilde{X}^2\Delta$	MRCI	1.536	1026	5.4	1017	0
	MRCI/CBS	1.535	1027	5.3	1019	0
	MRCI + Q	1.539	1019	5.6	1010	0
	C-MRCI	1.527	1038	5.2	1030	0
	C-MRCI/CBS	1.526	1040	5.1	1032	0
	C-MRCI + Q	1.531	1025	4.5	1019	0
$^2\Pi$	MRCI	1.674	571	44.3	522	21289
	MRCI + Q	1.671	572	35.7	493	21135
	C-MRCI	1.676	599	41.9	536	21487
	C-MRCI + Q	1.670	554	22.6	489	21355
		^{52}Cr^{16}O^{2+}				
$\tilde{X}^3\Sigma^-$	MRCI	1.529	972	13.2	947	0
	MRCI/CBS	1.528	970	13.2	944	0
	MRCI + Q	1.529	972	12.3	948	0
	C-MRCI	1.527	971	13.3	946	0
	C-MRCI/CBS	1.528	975	13.3	950	0
	C-MRCI + Q	1.530	970	12.4	946	0
$^1\Gamma$	MRCI	1.507	1065	8.1	1048	11197
	MRCI + Q	1.508	1063	8.1	1046	11138
	C-MRCI	1.504	1071	7.8	1056	10261
	C-MRCI + Q	1.505	1070	7.6	1055	10216
$^5\Sigma^-$	MRCI	1.975	327	0.2	326	13100
	MRCI + Q	1.946	331	−0.1	332	13360
	C-MRCI	1.959	337	0.3	336	13381
	C-MRCI + Q	1.918	349	0.3	349	14119
$^1\Sigma^+$	MRCI	1.514	1019	8.4	1003	14278
	MRCI + Q	1.515	1019	8.3	1003	13968
	C-MRCI	1.509	1049	8.8	1031	13785
	C-MRCI + Q	1.511	1047	8.1	1031	13232
$^7\Sigma^-$	MRCI	2.202	370	3.1	364	15523
	MRCI + Q	2.200	372	3.1	366	15973
	C-MRCI	2.189	378	3.1	372	15809
	C-MRCI + Q	2.184	383	3.2	376	16875
$^3\Phi$	MRCI	1.601	760	10.7	736	16942
	MRCI + Q	1.596	745	12.4	745	16197
	C-MRCI	1.593	516	29.2	392	17256
	C-MRCI + Q	1.584	449	22.0	677	16323
$^3\Pi$	MRCI	1.622	770	11.7	746	18404
	MRCI + Q	1.614	755	2.4	765	17717
	C-MRCI	1.610	874	30.9	784	18699
	C-MRCI + Q	1.598	877	17.7	831	17782
		^{55}Mn^{16}O^{2+}				
$\tilde{X}^4\Sigma^-$	MRCI	2.191	316	2.3	312	0
	MRCI/CBS	2.187	315	1.9	312	0
	MRCI + Q	2.183	315	2.3	311	0
	C-MRCI	2.179	322	2.4	318	0
	C-MRCI/CBS	2.172	322	1.8	319	0
	C-MRCI + Q	2.163	323	2.4	319	0
$^6\Sigma^-$	MRCI	2.234	326	2.6	321	310
	MRCI + Q	2.229	326	2.5	321	355
	C-MRCI	2.222	332	2.6	327	337
	C-MRCI + Q	2.210	335	2.6	330	418
$^8\Sigma^-$	MRCI	2.280	333	2.8	327	613
	MRCI + Q	2.277	333	2.8	328	697
	C-MRCI	2.268	339	2.9	334	669
	C-MRCI + Q	2.261	342	3.0	337	848
$^6\Delta$	MRCI	2.227	330	2.8	324	17030
	MRCI + Q	2.221	330	2.8	324	16749
	C-MRCI	2.215	336	2.9	330	17359
	C-MRCI + Q	2.202	338	2.9	333	16951
$^2\Delta$	MRCI	1.508	961	12.2	934	18056
	MRCI + Q	1.509	952	9.6	934	16748
	C-MRCI	1.506	969	11.6	945	16592
	C-MRCI + Q	1.507	974	10.6	951	14113
$^2\Pi$	MRCI	1.640	603	19.1	568	23447
	MRCI + Q	1.633	649	18.6	612	22036
	C-MRCI	1.636	633	22.7	584	22366
	C-MRCI + Q	1.622	702	19.3	655	19769
		^{59}Co^{16}O^{2+}				
$\tilde{X}^6\Phi$	MRCI	2.105	382	2.7	376	0
	MRCI/CBS	2.110	382	2.6	377	0
	MRCI + Q	2.095	382	2.7	377	0
	C-MRCI	2.104	386	2.8	381	0
	C-MRCI/CBS	2.103	386	2.6	381	0
	C-MRCI + Q	2.091	389	2.8	384	0
$^4\Phi$	MRCI	2.081	368	2.8	362	113
	MRCI + Q	2.073	368	2.8	363	156
	C-MRCI	2.079	370	2.8	365	65
	C-MRCI + Q	2.066	370	2.8	365	104
$^2\Phi$	MRCI	2.083	369	2.6	363	184
	MRCI + Q	2.075	370	2.6	365	269
	C-MRCI	2.081	371	2.6	365	85
	C-MRCI + Q	2.068	375	2.6	370	163
$^6\Sigma^+$	MRCI	2.079	375	2.6	370	292
	MRCI + Q	2.068	370	2.6	365	268
	C-MRCI	2.080	372	2.7	367	319
	C-MRCI + Q	2.064	375	2.7	370	289
		^{58}Ni^{16}O^{2+}				
$\tilde{X}^5\Delta$	MRCI	2.025	398	2.9	392	0
	MRCI/CBS	2.023	399	2.8	393	0
	MRCI + Q	2.009	398	3.0	392	0
	C-MRCI	2.029	401	2.9	396	0
	C-MRCI/CBS	2.027	402	2.9	396	0
	C-MRCI + Q	2.011	404	3.0	398	0
$^3\Delta$	MRCI	2.050	399	2.7	394	1642
	MRCI + Q	2.041	402	2.6	397	1326
	C-MRCI	2.060	397	2.8	391	724
	C-MRCI + Q	2.049	401	2.9	395	817
$^1\Delta$	MRCI	2.067	390	2.0	387	2015
	MRCI + Q	2.060	392	1.6	390	1672
	C-MRCI	2.067	390	2.1	388	2000
	C-MRCI + Q	2.057	395	1.5	394	1486
		^{63}Cu^{16}O^{2+}				
$\tilde{X}^4\Sigma^-$	MRCI	1.945	415	2.4	410	0
	MRCI/CBS	1.943	416	2.4	411	0
	MRCI + Q	1.927	417	2.3	413	0
	C-MRCI	1.951	416	2.5	411	0
	C-MRCI/CBS	1.949	416	2.4	411	0
	C-MRCI + Q	1.932	420	2.4	415	0
$^2\Sigma^-$	MRCI	2.004	415	2.9	409	960
	MRCI + Q	1.999	417	2.9	412	1787
	C-MRCI	2.007	414	2.9	409	523
	C-MRCI + Q	1.998	419	2.9	413	1425

133

Table 1 (continued)

State	Method[a]	r_e	ω_e	$\omega_e x_e$	$\Delta G_{1/2}$	T_e
$^2\Pi$	MRCI	2.054	395	2.8	389	3951
	MRCI + Q	2.055	393	2.6	388	4233
	C-MRCI	2.053	396	2.9	391	3734
	C-MRCI + Q	2.046	400	2.7	394	4082

[a] The quintuple-zeta basis sets are employed, except for MRCI/CBS and C-MRCI/CBS, which correspond to the complete basis set limit (see Computational details).

TiO^{2+}

The ground state of TiO is a $^3\Delta$ state with one σ [$3d_{z^2}$(Ti)–$2p_z$(O); Ti placed at the origin and O at $z > 0$] and two π [$3d_{xz}$(Ti) + $2p_x$(O) or $3d_{yz}$(Ti) + $2p_y$(O)] bonds, all polarized towards oxygen, one δ [$3d_{xy}$(Ti) or $3d_{x^2-y^2}$(Ti)] electron, localized on titanium, and one electron in a hybrid σ_{Ti} [$4s$(Ti)–$3d_{z^2}$(Ti)] orbital localized on titanium but polarized away from oxygen.[31] The first electron detaches from the latter σ_{Ti} orbital generating the $^2\Delta$ ground state of TiO^+ ($\sigma^2\pi^4\delta^1$). The second electron leaves from the δ orbital producing the $^1\Sigma^+$ ground state of TiO^{2+} ($\sigma^2\pi^4$). The possibility of removing a π electron (instead of δ) leads to a ($\sigma^2\pi^3\delta^1$) configuration, which corresponds to the next four states $^{1,3}\Phi$ and $^{1,3}\Pi$. These states lie at about 20 000 cm^{-1} higher and bear considerably longer bonds, 1.56 vs. 1.80 Å, justified by the cleavage of one π bond. Table 1 lists all our numerical data for the first three states of singlet spin multiplicity, $^1\Sigma^+$, $^1\Phi$, $^1\Pi$, and the first triplet state $^3\Phi$. Fig. 1 shows the PECs for these five states plus the next two of $^{1,3}\Delta$ symmetry, which correspond to a $\sigma^1\pi^4\delta^1$ configuration. All $^{1,3}(\Pi, \Delta, \Phi)$ states have $M^{3+}O^\bullet$ oxyl character.

Typical orbitals for all MO^{2+} systems are shown in Fig. 2 and correspond to TiO^{2+} (early transition metal) and NiO^{2+} (late transition metal). The dominant configuration of the ground state is indeed $\sigma^2\pi^4$ with a configuration interaction (CI) vector coefficient of 0.79 (62%). The next six most important configurations correspond to σ → σ* and π → π*, which signify oxygen to metal electron transfer (oxyl character): σ and π are polarized towards oxygen, while σ* and π* towards titanium. The opposite polarization is observed for late transition metals. The overall contribution of these six components is 24%. The remaining 14% corresponds to numerous other configurations demonstrating the high multi-reference character of these systems. The $\sigma^2\pi^3\delta^1$ character constitutes the 85% (four components) for $^1(\Pi, \Phi)$ and 87% (two components) for $^3(\Pi, \Phi)$, while the $\sigma^1\pi^4\delta^1$ character for $^1\Delta$ and $^3\Delta$ is 84% (two components) and 86% (single component).

The MRCI results of Table 1 indicate that the +Q correction affects the equilibrium bond length r_e by a few mili-Å but generally increase the vibrational frequencies by 20–30 cm^{-1}. This is observed mainly for the excited states, regardless of the inclusion of the sub-valence electron correlation (MRCI vs. C-MRCI). The excitation energies increase in the MRCI → MRCI + Q → C-MRCI → C-MRCI + Q order overall by 765 cm^{-1} and 945 cm^{-1} (MRCI to C-MRCI + Q) for the $^1\Pi$ and $^1\Phi$ states. As expected from the morphology of the PECs (see Fig. 1), the

vibrational frequencies ω_e are considerably smaller (about 300 cm^{-1}) for the excited states. The sub-valence electron correlation affects both r_e and ω_e. The former drops by 0.01–0.02 Å, as noticed earlier for TiO^+ and TiO,[31] and the latter decreases for the ground state but increases for the excited states (see Table 1).

A final comment pertains to the dissociation limit of the PECs. The first two ionization energies of Ti are 6.83 and 13.58 eV.[50] The latter is slightly smaller than the first ionization of oxygen (13.62 eV)[50] stabilizing the Ti^{2+} + O over Ti^+ + O^+ fragments by 0.04 eV. Indeed, our PECs dissociate smoothly to Ti^{2+} + O. For every other metal, the second ionization energy is higher than 13.62 eV by at least 1.0 eV and the lowest energy fragments are M^+ + O^+. However, our PECs still dissociate to M^{2+} + O. We have seen this for other first- and second-row transition metal dicationic oxides (FeO^{2+}, RhO^{2+}, RuO^{2+}).[17,18,51] For FeO^{2+} and RuO^{2+},[18,51] we were able to get the right dissociation channel by introducing a larger active space including a second set of d-orbitals. This practice was unsuccessful for the present oxides and RhO^{2+}.[17] The stability of all MO^{2+} species with respect to the M^+ + O^+ dissociation products is examined in more detail in the Summary section.

VO^{2+}

The vanadium oxide dication is quite similar to TiO^{2+} with a well separated ground state of primarily oxo character (71%). The additional electron populates one of the δ orbitals producing the $\tilde{X}^2\Delta$ state. The next six (oxyl) components (σ → σ* and π → π*; see TiO^{2+}) account for the 15% of the remaining wavefunction. Therefore, compared to TiO^{2+}, the oxo nature has increased by 10%. The next group of states, $^2\Pi$, $^4\Delta$, $^4\Pi$, and $^6\Sigma$ lie at 21 000 cm^{-1} and higher and have flat or repulsive PECs (see Fig. 1). The quartet and doublet states are result of O → M electron transfer (π → δ, π → π*), while $^6\Sigma$ is a repulsive curve from the ferromagnetic coupling of the $M^{2+}(3d^3)$ + $O(2p^4)$ unpaired electrons. It should be added that the $V^{4+}(^2D)$ + O^{2-} (^1S) combination creates three oxo states, $^2\Delta$, $^2\Pi$, and $^2\Sigma^+$, with an electron in the δ, π*, σ* orbitals. The first one is the ground state, while the second one participates in the wavefunction of the $^2\Pi$ at equilibrium (~1.7 Å) and shorter distances. Specifically, the first two larger CI vector components of $^2\Pi$ at 1.7 Å are $\sigma^2\pi^3\delta^2$ (31%) and $\sigma^2\pi^4\pi^{*1}$ (26%). The $^2\Sigma^+$ state is expected to be higher than the present energy scale, due to the antibonding nature of σ*.

The bond of the ground state is shorter than TiO^{2+} (1.53 vs. 1.54 Å at C-MRCI; see Table 1) and gets shorter at C-MRCI by ~0.01 Å. The same trends can be seen for neutral and cationic counterparts.[30,31] Going from TiO^{2+} to VO^{2+}, the additional electron resides at a δ orbital, which has no amplitude along the interatomic axis, and the increased nuclear charge of the metal is not screened. Therefore, the σ^2 electrons [~$2p_z(O)^2$] experience larger attraction ($V^{4+} \leftarrow :O^{2-}$) and bring the two atoms closer. This stabilization can explain also the higher oxo character of VO^{2+}. The minimum of the flat PEC of the first excited state ($^2\Pi$) is at 1.67 Å, 0.1 Å longer than $\tilde{X}^2\Delta$. The ω_e
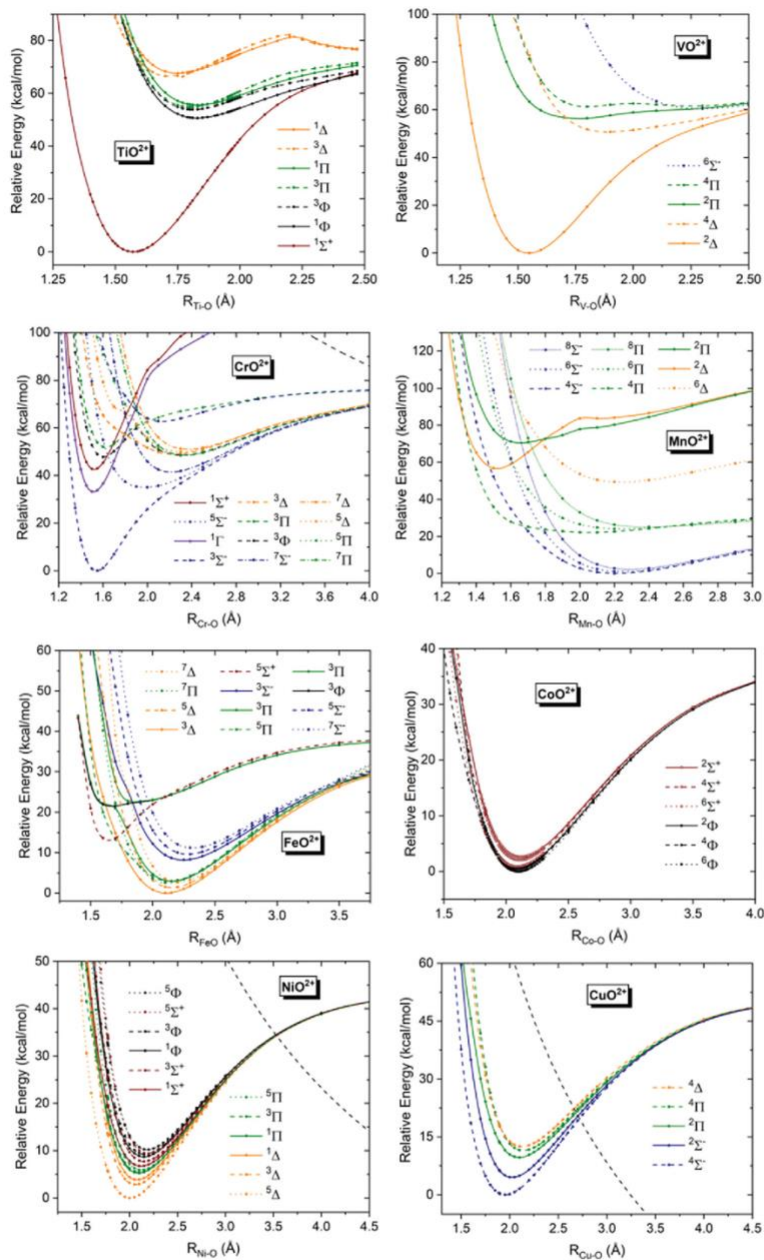
This journal is © the Owner Societies 2021

Phys. Chem. Chem. Phys., 2021, **23**, 21172–21182 | **21175**

134

Fig. 1 MRCI/cc-pVTZ(M) aug-cc-pVTZ(O) PECs for first row MO^{2+} species, M = Ti–Cu. The dashed black curves shown in CrO^{2+}, NiO^{2+}, and CuO^{2+} correspond to the M^{+} + O^{+} Coulombically repulsive curves.

values for VO^{2+} (~1030 cm^{-1} for $\tilde{X}^2\Delta$ and less than 600 cm^{-1} for $^2\Pi$) are about 50 cm^{-1} smaller than TiO^{2+}.

Our best bond length of 1.531 Å is in excellent agreement of the MR-ACPF value (1.54 Å) but considerably longer than the

21176 | Phys. Chem. Chem. Phys., 2021, 23, 21172–21182

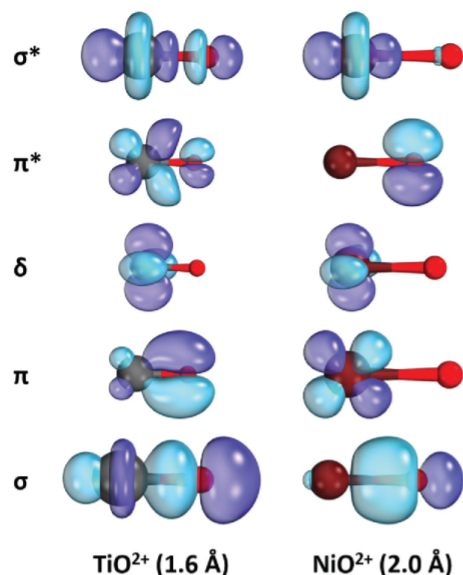This journal is © the Owner Societies 2021

135

Fig. 2 Typical molecular orbitals for the early and late MO^{2+} species at equilibrium. The TiO^{2+} and NiO^{2+} orbitals are specifically shown at 1.6 and 2.0 Å, respectively.

B3LYP value (1.49 Å) of Schröder *et al.*[26] The latter authors examined also the $^4\Delta$ state, which was found at ~ 2.5 eV (or $\sim 20\,000$ kcal mol^{-1}) with an equilibrium bond length of 1.70 Å. Our values for this state are ~ 1.9 Å and $\sim 18\,000$ cm^{-1}.

Finally, we calculated the spin–orbit splitting for the ground state $^2\Delta$ by diagonalizing the spin–orbit Breit–Pauli Hamiltonian using the four (M_L, M_S) MRCI wavefunctions of $^2\Delta$ as "basis set". The splitting is found to be 369 cm^{-1}, which is about half of the *in situ* $V^{4+}(^2D)$ center (624.87 cm^{-1}).[52]

CrO^{2+}

The addition of a second electron to TiO^{2+} populates a δ orbital. The $\sigma^2\pi^4\delta^2$ configuration of CrO^{2+} generates three states: the ground high-spin state $\tilde{X}^3\Sigma^-$ $(\sigma^2\pi^4\delta_+^1\delta_-^1)$, and the sister low-spin states $^1\Gamma$ and $^1\Sigma^+$ $(\sigma^2\pi^4\delta_+^2 \pm \sigma^2\pi^4\delta_-^2)$; $\delta_\pm$ are the two δ orbitals. The components in the parentheses account for the 66% (coefficient = 0.81), 77% (coefficients = 0.62/−0.62) and 72% (coefficients = 0.60/0.60) of the wavefunction for $\tilde{X}^3\Sigma^-$, $^1\Gamma$ and $^1\Sigma^+$, respectively. These three states have the shortest bond lengths among the low-lying electronic states of CrO^{2+}: 1.530, 1.505 and 1.511 Å (C-MRCI + Q; see Table 1). Sub-valence electron correlation plays a smaller role for CrO^{2+} compared to the previous two oxides. The bond length drops only by less than 0.005 Å. However, it reduces the excitation energies by approximately 1000 cm^{-1}. The $^1\Gamma$ state is the first excited state at $\sim 11\,000$ cm^{-1} at MRCI or MRCI + Q and ~ 10.000 cm^{-1} at C-MRCI or C-MRCI + Q, while $^1\Sigma^+$ is the third excited state at $\sim 13\,500$ cm^{-1} (see Table 1). Finally, the harmonic vibrational frequencies are larger by ~ 100 cm^{-1} for the singlets.

Starting from the $\sigma^2\pi^4\delta^1$ ground state of VO^{2+}, the possibility of the additional electron to populate a $\pi^\star$ orbital generates the $^3\Phi$ and $^3\Pi$ excited states. The contribution of the $\sigma^2\pi^4\delta^1\pi^{\star 1}$ $(\sigma^2\pi^4\delta_+^1\pi_x^{\star 1} \pm \sigma^2\pi^4\delta_-^1\pi_y^{\star 1}$ or $\sigma^2\pi^4\delta_+^1\pi_y^{\star 1} \pm \sigma^2\pi^4\delta_-^1\pi_x^{\star 1})$ configuration is 67% and 63% in the two states. The bond distance elongates considerably and it is almost 0.1 Å longer than the singlet states (see Table 1). These are the highest energy states studied presently lying in the 16 000–18 000 cm^{-1} energy region.

The PECs of CrO^{2+}, shown in Fig. 1, revealed the presence of two more states in between the previously mentioned states with even longer bond distances. The $^5\Sigma^-$ lies at 14 119 cm^{-1} with $r_e = 1.92$ Å and $\omega_e = 349$ cm^{-1} (C-MRCI + Q). The small value of the latter is due to the wider PEC of this state. The other state is a $^7\Sigma^-$ with even longer bond distance (~ 2.2 Å) and similar ω_e (~ 380 cm^{-1}). Starting from the ground state, the quintet/septet states involve the promotion of one/two π electron(s) to one/two $\pi^\star$ orbital(s). The quintet can be characterized as an oxyl $Cr^{3+}O^\bullet$ state but the septet is better described as the interaction of $Cr^{2+}(^5D;\ 3d^4) + O(^3P;\ 2p^4)$. Overall, CrO^{2+} shows a higher diversity and density of states compared to the early TiO^{2+} and VO^{2+} species.

In this case, there is a very recent *ab initio* work of similar high-level by Ornellas and co-workers, who constructed potential energy curves for more states at the MRCI level.[28] However, they did not identify the first two excited states $^1\Gamma$ and $^1\Sigma^+$. Equilibrium bond lengths and excitation energies are in common only for the ground state $\tilde{X}^3\Sigma^-$ and the excited state $^3\Pi$. Our numbers are in excellent agreement with them. The bond lengths agree within 0.004 Å and the excitation energies by less than 400 cm^{-1}.

MnO^{2+}

The PECs of Fig. 1 indicate a clear distinction between MnO^{2+} and the previous oxides: the lowest energy curves are those with the longer bond lengths and correspond to shallow minima due to the interaction of the $Mn^{2+} + O$ fragments. The ground state of Mn^{2+} is $^6S(3d^5)$ and its combination with $O(^3P;\ 2s^22p^4)$ yields the $^{4,6,8}\Sigma^-$ and $^{4,6,8}\Pi$ states. The former states are lower in energy, and their PECs are nearly parallel for distances longer than 2.2 Å. For shorter distances (repulsive region), the $^8\Sigma^-$ shows the steepest increase followed by the $^6\Sigma^-$ and finally the $\tilde{X}^4\Sigma^-$. The order of the equilibrium bond lengths, $r_e(X^4\Sigma^-) < r_e(^6\Sigma^-) < r_e(^8\Sigma^-)$, is a reflection of this observation (see Table 1). The reason why lower spin pertains to smaller repulsion is that lower-spin states include electron configurations with spin coupling between electrons of Mn^{2+} and O. Specifically, the wavefunction of the high spin $^8\Sigma^-$ is nearly single determinantal (coefficient = 0.99, 98%) with all five electrons of Mn^{2+} and two electrons of O centers having the spin. The wavefunctions of the $^6\Sigma^-$ and $\tilde{X}^4\Sigma^-$ are clearly multireference. Their largest coefficients correspond to the same electron configuration with one or two spin flipped electrons (50% for $^6\Sigma^-$ and 37% for $\tilde{X}^4\Sigma^-$), but there are numerous configurations where two electrons couple into the same orbital with coefficients between 0.15 and 0.30.

This journal is © the Owner Societies 2021

Phys. Chem. Chem. Phys., 2021, **23**, 21172–21182 | **21177**

136

The PECs of the $^{4,6,8}\Pi$ states are purely repulsive, except for the $^4\Pi$ state which shows a very shallow minimum at around 1.9 Å. Looking at the CI vector of $^4\Pi$ at 1.9 Å, we clearly see that this is due to a mixing with an oxo $Mn^{4+}O^{2-}$ state $\sigma^2\pi^4\delta^2\pi^{*1}$, which is dominant at this distance (66%). Due to the lack of a deep potential well, no numerical data are reported for these states in Table 1.

The next electronic state comes from the next Mn^{2+} + O channel, which pertains to the excitation of oxygen to ^1D. The $M_L = \pm 2$ components of ^1D have the strongest attraction with $Mn^{2+}(^6S)$ producing the $^6\Delta$ state with a $0.60[(\delta_+^1\delta_-^1\sigma^{*1}\pi_x^{*1}\pi_y^{*1})\sigma^2(\pi_x^2-\pi_y^2)]$ main configuration state function (CSF). The orbitals in the first parenthesis are localized on the metal and the σ, π orbitals of the second parenthesis on the oxygen. The bond length is 2.20 Å (C-MRCI + Q), practically (± 0.01 Å) equal to that of $^6\Sigma$ at every level of theory.

The next two PECs are well bound and are the lowest energy oxo $Mn^{4+}O^{2-}$ states with short bond distances (1.51 and 1.62 Å; C-MRCI + Q; see Table 1). The first one is a $^2\Delta$ state with a $\sigma^2\pi^4\delta^3$ configuration and the second one is a $^2\Pi$ state with the same $\sigma^2\pi^4\delta^2\pi^{*1}$ configuration found for the $^4\Pi$ at 1.9 Å and below (see above). These two states can be created by adding a δ or π^* electron to the ground state of CrO^{2+}. MnO^{2+} is the first system with a non-oxo ground state. The $^2\Delta$ and $^4\Pi$ states are at 14 113 and 19 769 cm^{-1} respectively. It is noteworthy that the excitation energy T_e drops significantly with the level of theory. Both the Davidson correction and the $3s^23p^6$ electron correlation decrease T_e values by more than 1000 cm^{-1}. In fact, the Davidson correction is more effective when the sub-valence electron correlation is included in the calculation ($\sim$1400 cm^{-1} vs. 2500 cm^{-1}).

FeO^{2+}

Although FeO^{2+} is not studied presently, for the sake of coherence we summarize the main findings of our earlier study.[18] The PECs of FeO^{2+} reveal many similarities with MnO^{2+}. The lowest energy structures belong to the $Fe^{2+}(^5D; 3d^6)$ + O(^3P) channel, but due to the high degeneracy of $Fe^{2+}(^5D)$ there are numerous minima of triplets, quintets, and septets (see Fig. 1 of this article and Fig. 3, 4, and 5 of ref. 18) in the 2.1–2.3 Å range of Fe–O distances. The ground state is $\tilde{X}^3\Delta$ followed by a $^5\Delta$ and $^7\Delta$ within 641 cm^{-1} (MRCI + Q). As in MnO^{2+}, the high-spin $^7\Delta$ state is single reference with a $\sigma^2\pi^2\delta^3\pi^{*2}\sigma^{*1}$ configuration, which has an extra δ electron compared to $^8\Sigma$ of MnO^{2+}. The $\tilde{X}^3\Delta$ and $^5\Delta$ states have rich multireference character with $Fe^{2+}O^{\bullet\bullet}$ and $Fe^{3+}O^{\bullet}$ components.

Four low-lying oxo states were identified at 4049 cm^{-1} ($^5\Sigma^+$), a $^5\Pi$ at the same region but it appears as a shoulder of the first $^5\Pi$ PEC, a $^3\Phi$ at 8491 cm^{-1}, and a $^3\Pi$ at the same region appearing as a shoulder too. The presence of a water or ammonia ligand stabilized these oxo states including the shoulders further (see Fig. 6 of ref. 18), and in the case of $(NH_3)FeO^{2+}$ $^5\Sigma^+$ became the ground state. The dominant configurations of $^5\Sigma^+$, $^5\Pi$, and $^3(\Phi, \Pi)$ are $\sigma^2\pi^4\delta^2\pi^{*2}$, $\sigma^2\pi^4\delta^2\pi^{*1}\sigma^{*1}$, and $\sigma^2\pi^4\delta^3\pi^{*1}$, respectively. An interesting observation is that compared to the lowest energy oxo state of MnO^{2+} ($^2\Delta$; $\sigma^2\pi^4\delta^3$), the additional electron does not populate the last δ available
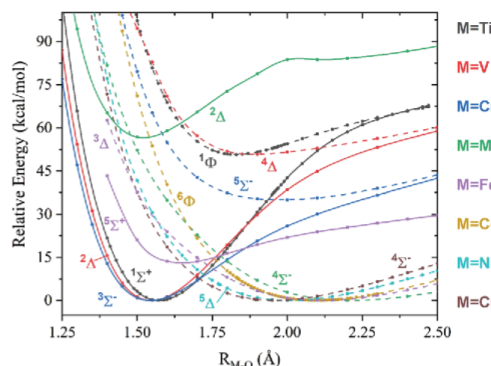

Fig. 3 MRCI PECs for the lowest oxo (solid lines) and oxyl (dashed lines) states of the first row MO^{2+} species, M = Ti–Cu.
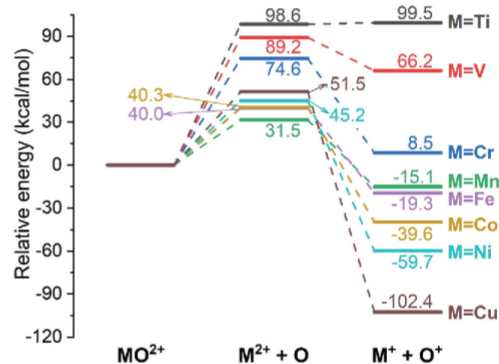

Fig. 4 Relative energy of the M^{2+} + O and M^+ + O$^+$ channels with respect to the MO^{2+} equilibrium energy for M = Ti–Cu. See text for details.

spot in the FeO^{2+} oxo states. Instead, these are better seen as coming from the higher energy MnO^{2+} ($^2\Pi$; $\sigma^2\pi^4\delta^2\pi^{*1}$) state with an addition of an electron to either π^* or σ^*, but again not to the δ orbital. This is opposite to what happens for the second-row counterpart of FeO^{2+}, RuO^{2+}, which has a $^1\Sigma^+$ ($\sigma^2\pi^4\delta^4$) ground state.[18,51]

CoO^{2+}

Cobalt marks the beginning of a different kind of dicationic oxides. Our calculations indicate no oxo states among the lowest-lying electronic states. Our CASSCF PECs for many more states, which are shown in the ESI† (Fig. S2), revealed states with potential well minima only in the 2.0–2.2 Å region. Our MRCI PECs for the lowest six states confirmed this observation (see Fig. 1). The molecular orbitals now resemble the NiO^{2+} orbitals (see Fig. 2). The π bonding orbital is clearly localized on the metal ($\sim 3d_{xz}$ or $3d_{yz}$), π^* is practically the 2p orbital of oxygen, σ remains the $2p_z(O)$ but more polarized towards

137

oxygen, and σ^* becomes nearly identical to the $3d_{z^2}$ orbital of the metal.

The PECs of Fig. 1 indicate the $Co^{2+} + O$ fragments as the origin of the curves. The ground state of Co^{2+} is $^4F(3d^7)$ and its "marriage" with $O(^3P)$ gives 21 molecular states: $^{2,4,6}[\Sigma^+(2),$ $\Sigma^-(1), \Pi(3), \Delta(3), \Phi(2), \Gamma(1)]$. According to our MRCI calculations the lowest three states are $^{2,4,6}\Phi$ followed by the $^{2,4,6}\Sigma^+$ states. The first four states ($^{2,4,6}\Phi$ and $^6\Sigma^+$) lie within 300 cm^{-1} with $\tilde{X}^6\Phi$ being the ground state. The two sextet states consist of two primary electron configurations: $^6\Sigma^+ \sim 0.88\ \sigma^2\pi^4\delta^2\pi^{*2}\sigma^{*1} - 0.46$ $\sigma^2\pi^2\delta^4\pi^{*2}\sigma^{*1}$ and $\tilde{X}^6\Phi \sim 0.70\ \sigma^2\pi_x^1\pi_y^2\delta_-^2\delta^1\pi^{*2}\sigma^{*1} - 0.70$ $\sigma^2\pi_{x^2}\pi_{y^1}\delta_+^1\delta^2\pi^{*2}\sigma^{*1}$. Both expressions imply two unpaired electrons on oxygen ($\sigma^2\pi^{*2} \approx 2p_z^22p_x^12p_y^1$) suggesting the involvement of O (^3P; $M_L = 0$), and consequently of Co^{2+} (^4F; $M_L = 0$), Co^{2+} (^4F; $M_L = \pm 3$) for $^6\Sigma^+$, $^6\Phi$, respectively. Indeed, the Co^{2+} (^4F; $M_L = 0$) wavefunction is given by $\sqrt{4/5}\ (3d_{z^2})^1(3d_{xz})^2(3d_{yz})^2$ $(3d_{x^2-y^2})^1(3d_{xy})^1 - \sqrt{1/5}\ (3d_{z^2})^1(3d_{xz})^1(3d_{yz})^1(3d_{x^2-y^2})^2(3d_{xy})^2$, which coincides with the $^6\Sigma^+$ wavefunction considering that $\pi \sim 3d_{xz}$ or $3d_{yz}$, $\delta \sim 3d_{x^2-y^2}$ or $3d_{xy}$, and $\sigma^* \sim 3d_{z^2}$ (see Fig. 2). A similar observation can be seen for the $\tilde{X}^6\Phi$ state. The sister quartet and doublet states bear the same dominant configurations, but they are highly multi-reference states due to the numerous possible spin couplings. The quartet states have 10 electronic configurations of this type with coefficients between 0.15 and 0.50, and the doublets have 20 such configurations with coefficients between 0.10 and 0.60. Overall, these account for the 96–98% of their wavefunctions.

As can be seen from Fig. 1, all six PECs are nearly parallel to each other, and they are expected to have similar equilibrium bond lengths and vibrational frequencies. Indeed, the MRCI numerical data of Table 1 predict $r_e = 2.08$–2.10 Å, $\omega_e = 374 \pm 10$ cm^{-1}, and $\omega_e x_e = 2.7 \pm 0.1$ cm^{-1} for the first four states. The core +Q effects have minimal effects on these data reducing r_e by ~ 0.005 Å and increasing ω_e by ~ 5 cm^{-1}.

A final comment has to do with the PEC of $^4\Phi$, which exhibits a shoulder at the repulsive region around 1.6 Å. This is due to the presence of oxo components (46%) in the wavefunction at this distance. This shoulder is expected to evolve to a minimum upon the addition of ammonia or other strong field ligands.[18] Indeed, Wang et al. recently made a Co(IV)–oxo complex using substituted ammonia ligands.[1]

NiO^{2+}

Nickel oxide dication is very similar to CoO^{2+}. The lowest PECs come from $Ni^{2+} + O$, they have minima in the 2.0–2.2 Å range and are nearly parallel. The ground state of Ni^{2+} is $^3F(3d^8)$ and combined with $O(^3P)$ gives 21 states with the exact same spatial symmetry as $Co^{2+} + O$ but different spin multiplicities: $^{1,3,5}[\Sigma^+(2), \Sigma^-(1), \Pi(3), \Delta(3), \Phi(2), \Gamma(1)]$. The ground state $\tilde{X}^5\Delta$ results from the $Ni^{2+}(^3F; M_L = \pm 2) + O(^3P; M_L = 0)$ combination and has a single dominant configuration ($\sigma^2\pi^4\delta^3\pi^{*2}\sigma^{*1}$, 98%). The corresponding $^3\Delta$ and $^1\Delta$ states have the same electronic structure but four and six Slater determinants are used to describe the spin coupling with coefficients 0.57 and smaller. Their total contribution is 99% in both cases. The $^{1,3}\Delta$ states are the first and second excited states of NiO^{2+}.

Fig. 1 shows MRCI PECs for totally 12 states, but we report data only for the first three of them in Table 1. There are CASSCF PECs for even more states connected to higher energy fragments in the ESI† (Fig. S3) confirming the absence of low-lying oxo states. The ground state $^5\Delta$ has the shortest bond length, which starts at 2.025 Å and drops to 2.011 Å after including the +Q and sub-valence electron correlation effects. The first excited $^{1,3}\Delta$ states lie close to each other at around 1500 cm^{-1} at MRCI + Q with slightly (~ 0.02–0.03 Å) longer bonds, but $^3\Delta$ is stabilized to ~ 800 cm^{-1} at C-MRCI + Q. The vibrational frequencies for all states are about 400 cm^{-1} at all levels of theory.

CuO^{2+}

CuO^{2+} is a member of the same group of dicationic transition metal oxides as CoO^{2+} and NiO^{2+}. The ground state of NiO^{2+} ($^5\Delta$) can be generated from that of CoO^{2+} ($^6\Sigma^+$) by adding a δ electron and the same happens from NiO^{2+} to CuO^{2+}. The produced configuration $\sigma^2\pi^4\delta^4\pi^{*2}\sigma^{*1}$ is of $^4\Sigma^-$ symmetry, accounts for 98% of the ground state, and hails from the interaction of $Cu^{2+}(^2D; 3d^9; M_L = 0)$ and $O(^3P; M_L = 0)$. The corresponding $^2\Sigma^-$ state is the first excited state of the system, and its wavefunction consists of the three configurations due to the three possible spin-flips of the $\tilde{X}^4\Sigma^-$ configuration. The three coefficients 0.80 (σ^* spin–flip) and -0.41×2 (π^* spin–flip) make up the 98% of the wavefunction. The next two states, $^{2,4}\Pi$, result from the $Cu^{2+}(^2D; 3d^9; M_L = \pm 1) + O(^3P; M_L = 0)$ combination, where one π ($\sim 3d_{xz}$ or $3d_{yz}$) electron moves to the σ^* ($\sim 3d_{z^2}$). The $\sigma^2\pi^3\delta^4\pi^{*2}\sigma^{*2}$ CSF gives 99% and 96% of the CI vector for the $^4\Pi$ and $^2\Pi$ states. The $^2\Pi$ state appears to be lower than the higher spin $^4\Pi$ against conventional chemistry intuition. Fig. 1 shows the PECs for these four states and Table 1 lists their spectroscopic parameters. As in the previous two oxides, the sub-valence electron correlation of the metal affects marginally the results. In the ESI† we report a larger number of PECs (Fig. S4, ESI†) at the CASSCF level of theory including all states coming from the $Cu^{2+}(^2D) + O(^3P)$ fragments: $^{2,4}[\Sigma^+(1), \Sigma^-(2), \Pi(3), \Delta(2), \Phi(1)]$.

IV. Summary and conclusions

Based on our previous reports, dicationic transition metal oxides can be categorized in three groups, early, middle, and late. The main distinction is the character of the ground and low-lying excited states. TiO^{2+}, VO^{2+}, and CrO^{2+} have well separated ground states of predominant $M^{4+}O^{2-}$ (oxo) nature. MnO^{2+} and FeO^{2+} have ground states of oxyl nature with long metal–oxygen bonds ($M^{2+}O^{\bullet\bullet} \leftrightarrow M^{3+}O^{\bullet-}$), but they also bear low-lying oxo states. CoO^{2+}, NiO^{2+}, and CuO^{2+} have ground states with strong $M^{2+}O^{\bullet\bullet}$ character and bear no low-lying oxo states. The oxo wall for naked metal oxide dications can be placed between Cr and Mn, but if we consider the low-lying oxo states of Mn and Fe and the fact that they can be stabilized with strong field ligands, then the oxo wall may be shifted between Fe and Co.

This journal is © the Owner Societies 2021

Phys. Chem. Chem. Phys., 2021, **23**, 21172–21182 | **21179**

138

TiO^{2+} starts as a closed shell $Ti^{4+}O^{2-}$ system followed by the $V^{4+}O^{2-}$ and $Cr^{4+}O^{2-}$ species with one and two ferromagnetically coupled δ electrons. The latter oxide has a richer electronic spectrum with five oxo states within 55 kcal mol^{-1} *vs.* none for the former oxides. The oxo states of CrO^{2+} involve $Cr^{4+}(\delta^2)$ [$\tilde{X}^3\Sigma^-$, $^1\Gamma$, $^1\Sigma^+$] and $Cr^{4+}(\delta^1\pi^{*1})$ [$^3\Pi$, $^3\Phi$] configurations. The first three states have the shortest bond lengths: 1.530, 1.505 and 1.511 Å (C-MRCI + Q; see Table 1). The average bond length for these $\sigma^2\pi^4\delta^2$ states of CrO^{2+} (1.516 Å) is shorter than the 1.545 (TiO^{2+}; $\sigma^2\pi^4\delta^1$) and 1.531 (VO^{2+}; $\sigma^2\pi^4$) Å. The reason is the larger effective metallic charge due to its minimal screening from the δ electrons. The bond length becomes even smaller for the $^2\Delta$ ($\sigma^2\pi^4\delta^3$) excited state of MnO^{2+} (1.507 Å).

The MnO^{2+} and FeO^{2+} species bear ground states with reduced metal centers and longer bond lengths (2.0 Å or longer). The lowest energy oxo state is the $^2\Delta$ ($\sigma^2\pi^4\delta^3$) for MnO^{2+} followed by a $^2\Pi$ ($\sigma^2\pi^4\delta^2\pi^{*1}$) state. The lowest oxo state of FeO^{2+} does not populate exclusively δ orbitals and it is a $^5\Sigma^+$ ($\sigma^2\pi^4\delta^2\pi^{*2}$). As expected, due to the population of π^*, the $^2\Pi$ and $^2\Sigma^+$ states of MnO^{2+} and FeO^{2+} have the longest bond lengths 1.62–1.63 Å among the oxo states. No low-lying oxo states are observed for CoO^{2+}, NiO^{2+} and CuO^{2+}, and they "reside" at the repulsive wall of their PECs.

On the other hand, the oxyl states ($M^{2+}O^{\bullet\bullet}$ or $M^{3+}O^{\bullet-}$) lie at around 20 000 cm^{-1} for TiO^{2+} and VO^{2+}, at around 14 000 cm^{-1} for CrO^{2+}, and become the lowest states for the remaining metals. The bond lengths are always longer than 1.8 Å, with the longest one belonging to MnO^{2+} ($\sim$2.2 Å), while r_e values the late transition metal oxides are all 2.0 ± 0.1 Å. Fig. 3 summarizes these observations in terms of PECs for the lowest energy oxo and oxyl states of all species. Notice that the curvature of the PECs around equilibrium changes lowering the vibrational frequencies as we move to the heavier atoms.

To comprehend this trend, we calculated the total energy needed for the formation of M^{4+} by adding the first four ionization energies of each metal.[50] The values start from Ti to Cu: 91.2 (Ti), 97.4 (V), 103.4 (Cr), 107.9 (Mn), 109.5 (Fe), 109.8 (Co), 115.9 (Ni), and 122.2 (Cu) eV. The monotonic increase rationalizes the de-stabilization of the $M^{4+}O^{2-}$ states. In addition, the population of anti-bonding orbitals (π^*, σ^*) as we go to the right of the periodic table weaken the binding interaction energy of the two *in situ* M^{4+} and O^{2-} ions. Electron donating groups (strong field ligands) are expected to stabilize the oxo states, while electron withdrawing ligands (weak field ligands) will stabilize the oxyl character.[18,19]

Fig. 4 graphically presents the stability of the equilibrium MO^{2+} structures (M = Ti–Cu) with respect to the $M^{2+} + O$ and $M^+ + O^+$ fragments. The energy of $M^{2+} + O$ channel, $E(M^{2+} + O)$, is obtained at the MRCI level of theory setting the two atoms at a distance of 100 Å. The energy has converged within 0.01 kcal mol^{-1} at this distance for all species. The energy $E(M^+ + O^+)$ of the $M^+ + O^+$ fragments was obtained using the experimental[50] second ionization energy of M (IE_{2M}) and the first ionization energy of O (E_{1O}) as: $E(M^+ + O^+) = E(M^{2+} + O) + E_{1O} - E_{2M}$. The $E(M^{2+} + O)$ energy for M = Ti is found to be 98.6 kcal mol^{-1}. Fig. 1 suggests a $E(Ti^{2+} + O)$ energy of around 70 kcal mol^{-1}, but

the full PEC given in the ESI† (Fig. S1) shows that the plateau formed in the 2.25–2.50 Å region is because of some avoided crossings. This energy drops going from Ti to Mn to 31.5 kcal mol^{-1} and then increases to 51.5 kcal mol^{-1} to Cu. Our MRCI value for VO^{2+} (89.2 kcal mol^{-1}) is within the wide experimental range of 92.2 ± 6.9 kcal mol^{-1}.[26]

On the contrary, the $E(M^+ + O^+)$ energy drops continuously from Ti to Cu. The $Ti^+ + O^+$ channel is actually higher than $Ti^{2+} + O$ by 1.0 kcal mol^{-1}, but the $M^+ + O^+$ channel drops rapidly for M = V–Cu to -102.4 kcal mol^{-1}. Overall, the early oxides TiO^{2+}, VO^{2+}, and CrO^{2+} are stable with respect to any dissociation channel, but the rest of them are metastable with respect to $M^+ + O^+$. We were unable to make theoretically the $M^+ + O^+$ curves and thus we considered the expected $1/r$ curve in the PECs of Fig. 1. It turns out that only for Cr, Ni and Cu fall within the energy and distance range of Fig. 1 (see black dashed lines in the Cr, Ni, and Cu plots). The predicted barrier for dissociation of NiO^{2+} and CuO^{2+} is thus 30–35 and 15–20 kcal mol^{-1}, respectively. MnO^{2+} has an expected barrier of around 30 kcal mol^{-1}, but for the rest of the oxides the barrier is higher than these values rendering them very stable systems. To our knowledge VO^{2+}, CrO^{2+}, and FeO^{2+} have been observed experimentally.[26,53–56] Ligands, such as ammonia, will stabilize the $M^{4+}O^{2-}$ form with respect to both channels since they will stabilize the M^{4+} center more than M^+ or M^{2+}.[18]

The authors of ref. 28 were able to extend the PECs to longer distances than ours, and they captured the $Cr^+ + O^+/Cr^{2+} + O$ crossing region correctly. Therefore, they were able to calculate the $E(M^+ + O^+)$ and $E(M^{2+} + O)$ of Fig. 4 directly from the energies of the asymptotic limits. We estimated their $E(M^{2+} + O)$ value based on their Fig. 2 as $\leq$28 000 cm^{-1} or $\leq$80.0 kcal mol^{-1}, which compares well to our 74.6 kcal mol^{-1} value. Their $E(M^+ + O^+)$ value is reported as 23.84 kcal mol^{-1}, which is considerably larger than our 8.5 kcal mol^{-1}. Recall that our value is estimated based on the experimental ionization energies of Cr^+ and O, and we believe that our value is more accurate. In any case, according to the inset of their Fig. 2, the $CrO^{2+} \rightarrow Cr^+ + O^+$ dissociation has to go through a barrier of almost equal to the $E(M^{2+} + O)$ energy of $\sim$75 kcal mol^{-1}. Therefore, the CrO^{2+} system should be considered thermodynamically and kinetically very stable, and it has been observed experimentally.[53–56]

From the technical point of view, the electron correlation of the $3s^2 3p^6$ sub-valence electrons of the metal is important for the correct prediction of the metal–oxygen bond lengths and vibrational frequencies, especially for the early transition metals. On the contrary, the Davidson correction contributes mostly to the excitation energies. Finally, our CBS values show that the bond distances have converged within 0.005 Å in all cases (within 0.002 Å for most of them) at the quintuple-ζ basis set, and the vibrational frequencies within 2–3 cm^{-1} (except for TiO^{2+} which converged within 6–7 cm^{-1}).

The various bonding schemes and chemical activity makes dicationic transition metal oxides excellent catalysts but mastering them needs a more systematic bottom-up approach. In the future we will monitor the effect of ligands and continue

21180 | *Phys. Chem. Chem. Phys.*, 2021, **23**, 21172–21182

This journal is © the Owner Societies 2021

the investigation of the second and third row transition metals (we already studied RuO^{2+} and RhO^{2+}),[17,51] where the relativistic effects play an important role and are expected to dramatically change the overall picture.

Conflicts of interest

There are no conflicts to declare.

Acknowledgements

References

1 B. Wang, Y.-M. Lee, W.-Y. Tcho, S. Tussupbayev, S.-T. Kim, Y. Kim, M. S. Seo, K.-B. Cho, Y. Dede, B. C. Keegan, T. Ogura, S. H. Kim, T. Ohta, M.-H. Baik, K. Ray, J. Shearer and W. Nam, *Nat. Commun.*, 2017, **8**, 14839.

2 K. Qin, C. D. Incarvito, A. L. Rheingold and K. H. Theopold, *J. Am. Chem. Soc.*, 2002, **124**, 14008–14009.

3 W. Rasheed, A. Draksharapu, S. Banerjee, V. G. Young Jr, R. Fan, Y. Guo, M. Ozerov, J. Nehrkorn, J. Krzystek, J. Telser and L. Que Jr, *Angew. Chem., Int. Ed.*, 2018, **57**, 9387–9391.

4 D. F. Leto, A. A. Massie, D. B. Rice and T. A. Jackson, *J. Am. Chem. Soc.*, 2016, **138**, 15413–15424.

5 K. H. Bok, M. M. Lee, G. R. You, H. M. Ahn, K. Y. Ryu, S.-J. Kim, Y. Kim and C. Kim, *Chem. – Eur. J.*, 2017, **23**, 3117–3125.

6 C. D. Nunes, P. D. Vaz, V. Félix, L. F. Veiros, T. Moniz, M. Rangel, S. Realista, A. C. Mourato and M. J. Calhorda, *Dalton Trans.*, 2015, **44**, 5125–5138.

7 H. Kotani, S. Kaida, T. Ishizuka, K. Mieda, M. Sakaguchi, T. Ogura, Y. Shiota, K. Yoshizawa and T. Kojima, *Inorg. Chem.*, 2018, **57**, 13929–13936.

8 H. Kotani, S. Kaida, T. Ishizuka, M. Sakaguchi, T. Ogura, Y. Shiota, K. Yoshizawa and T. Kojima, *Chem. Sci.*, 2015, **6**, 945–955.

9 J. Cho, J. Woo, J. Eun Han, M. Kubo, T. Ogura and W. Nam, *Chem. Sci.*, 2011, **2**, 2057–2062.

10 V. C. C. Wang, S. Maji, P. P. Y. Chen, H. K. Lee, S. S. F. Yu and S. I. Chan, *Chem. Rev.*, 2017, **117**, 8574–8621.

11 R. L. Halbach, D. Gygi, E. D. Bloch, B. L. Anderson and D. G. Nocera, *Chem. Sci.*, 2018, **9**, 4524–4528.

12 R. J. Martinie, C. J. Pollock, M. L. Matthews, J. M. Bollinger, C. Krebs and A. Silakov, *Inorg. Chem.*, 2017, **56**, 13382–13389.

13 A. Bodner, P. Jeske, T. Weyhermueller, K. Wieghardt, E. Dubler, H. Schmalle and B. Nuber, *Inorg. Chem.*, 1992, **31**, 3737–3748.

14 B. S. Mandimutsira, B. Ramdhanie, R. C. Todd, H. Wang, A. A. Zareba, R. S. Czernuszewicz and D. P. Goldberg, *J. Am. Chem. Soc.*, 2002, **124**, 15170–15171.

15 P. Comba and A. Merbach, *Inorg. Chem.*, 1987, **26**, 1315–1323.

16 J. M. Stauber and C. C. Cummins, *Inorg. Chem.*, 2017, **56**, 3022–3029.

17 S. N. Khan and E. Miliordos, *Inorg. Chem.*, 2021, accepted.

18 J. K. Kirkland, S. N. Khan, B. Casale, E. Miliordos and K. D. Vogiatzis, *Phys. Chem. Chem. Phys.*, 2018, **20**, 28786–28795.

19 B. A. Jackson and E. Miliordos, *Phys. Chem. Chem. Phys.*, 2020, **22**, 6606–6618.

20 I. R. Ariyarathna and E. Miliordos, *Phys. Chem. Chem. Phys.*, 2021, **23**, 1437–1442.

21 C. J. Ballhausen and H. B. Gray, *Inorg. Chem.*, 1962, **1**, 111–122.

22 T. Z. H. Gani and H. J. Kulik, *ACS Catal.*, 2018, **8**, 975–986.

23 A. Nandy, J. Zhu, J. P. Janet, C. Duan, R. B. Getman and H. J. Kulik, *ACS Catal.*, 2019, **9**, 8243–8255.

24 J. Fišer, K. Franzreb, J. Lörinčík and P. Williams, *Eur. J. Mass Spectrom.*, 2009, **15**, 315–324.

25 H. Johansen and K. Tanaka, *Chem. Phys. Lett.*, 1985, **116**, 155–159.

26 D. Schröder, M. Engeser, H. Schwarz and J. N. Harvey, *ChemPhysChem*, 2002, **3**, 584–591.

27 S. Almenia, M. Mogren Al Mogren, D. Ben Abdallah, R. Linguerri and M. Hochlaf, *Chem. Phys. Lett.*, 2016, **646**, 142–147.

28 L. Gonçalves dos Santos, K. Franzreb and F. R. Ornellas, *Chem. Phys. Lett.*, 2021, **771**, 138525.

29 Z. Parsons, C. Leavitt, T. Duong, G. S. Groenewold, G. L. Gresham and M. J. Van Stipdonk, *J. Phys. Chem. A*, 2006, **110**, 11627–11635.

30 E. Miliordos and A. Mavridis, *J. Phys. Chem. A*, 2007, **111**, 1953–1965.

31 E. Miliordos and A. Mavridis, *J. Phys. Chem. A*, 2010, **114**, 8536–8572.

32 C. N. Sakellaris, E. Miliordos and A. Mavridis, *J. Chem. Phys.*, 2011, **134**, 234308.

33 C. N. Sakellaris and A. Mavridis, *J. Phys. Chem. A*, 2012, **116**, 6935–6949.

34 C. N. Sakellaris and A. Mavridis, *J. Chem. Phys.*, 2013, **138**, 054308.

35 S. Midda, N. C. Bera, I. Bhattacharyya and A. K. Das, *THEOCHEM*, 2006, **761**, 17–20.

36 M. L. Polak, M. K. Gilles, J. Ho and W. C. Lineberger, *J. Phys. Chem.*, 1991, **95**, 3460–3463.

37 H. Xian, Z. X. Cao, X. Xu, X. Lu and Q. E. Zhang, *Chem. Phys. Lett.*, 2000, **326**, 485–493.

38 Y. Shimoyama and T. Kojima, *Inorg. Chem.*, 2019, **58**, 9517–9542.

39 P. J. Knowles and H.-J. Werner, *Chem. Phys. Lett.*, 1988, **145**, 514–522.

40 K. R. Shamasundar, G. Knizia and H.-J. Werner, *J. Chem. Phys.*, 2011, **135**, 054101.

41 H. J. Werner and P. J. Knowles, *J. Chem. Phys.*, 1988, **89**, 5803–5814.

42 S. R. Langhoff and E. R. Davidson, *Intl. J. Quantum Chem.*, 1974, **8**, 61–72.

43 N. B. Balabanov and K. A. Peterson, *J. Chem. Phys.*, 2005, **123**, 064107.

44 T. H. Dunning, *J. Chem. Phys.*, 1989, **90**, 1007–1023.

45 R. A. Kendall, T. H. Dunning and R. J. Harrison, *J. Chem. Phys.*, 1992, **96**, 6796–6806.

46 D. E. Woon and T. H. Dunning, *J. Chem. Phys.*, 1994, **100**, 2975–2988.

47 H.-J. Werner, P. J. Knowles, G. Knizia, F. R. Manby, M. Schütz, P. Celani, W. Györffy, D. Kats, T. Korona, R. Lindh, *et al.*, *MOLPRO, version 2015.1, a package of ab initio programs*, 2015.

48 Y. Nakao, K. Hirao and T. Taketsugu, *J. Chem. Phys.*, 2001, **114**, 7935–7940.

49 C. N. Sakellaris, A. Papakondylis and A. Mavridis, *J. Phys. Chem. A*, 2010, **114**, 9333–9341.

50 W. M. Haynes, *CRC Handbook of Chemistry and Physics*, 93rd edn, Taylor & Francis, 2012.

51 N. M. S. Almeida, I. R. Ariyarathna and E. Miliordos, *J. Phys. Chem. A*, 2019, **123**, 9336–9344.

52 A. Kramida, Y. Ralchenko, J. Reader and NIST ASD Team, *NIST Atomic Spectra Database (ver. 5.7.1)*, [Online], 2019, available: https://physics.nist.gov/asd [2020, October 11]. National Institute of Standards and Technology, Gaithersburg, MD. , DOI: 10.18434/T4W30F.

53 S. Ohkido, Y. Ishikawa and T. Yoshimura, *Appl. Surf. Sci.*, 1994, **76–77**, 261–265.

54 A. Fiedler, I. Kretzschmar, D. Schröder and H. Schwarz, *J. Am. Chem. Soc.*, 1996, **118**, 9941–9952.

55 G. D. Flesch, R. M. White and H. J. Svec, *Int. J. Mass Spectrom. Ion Phys.*, 1969, **3**, 339–363.

56 G. L. Kellogg, *J. Appl. Phys.*, 1982, **53**, 6383–6386.

141